

AMERICAN UNIVERSITY OF BEIRUT

VALIDATION AND EXTENSION OF SYNTHETIC
GROUND MOTION SIMULATION
PROCEDURES

by
YARA NAWAF DAOUD

A thesis
submitted in partial fulfillment of the requirements
for the degree of Master of Engineering
to the Department of Civil and Environmental Engineering
of the Maroun Semaan Faculty of Engineering and Architecture
at the American University of Beirut

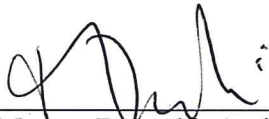
Beirut, Lebanon
August 2019

AMERICAN UNIVERSITY OF BEIRUT

VALIDATION AND EXTENSION OF SYNTHETIC
GROUND MOTION SIMULATION
PROCEDURES

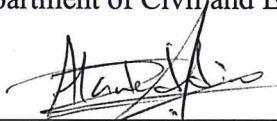
by
YARA NAWAF DAOUD

Approved by:



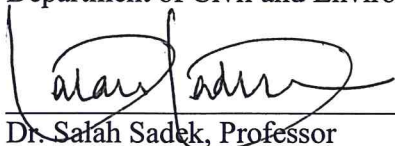
Dr. Mayssa Dabaghi, Assistant Professor
Department of Civil and Environmental Engineering

Advisor



Dr. Ibrahim Alameddine, Assistant Professor
Department of Civil and Environmental Engineering

Member of Committee



Dr. Salah Sadek, Professor
Department of Civil and Environmental Engineering

Member of Committee



Dr. Hikmat Zefbe, Associate Professor
Department of Civil and Environmental Engineering, University of Balamand

Member of Committee

Date of thesis defense: August 8, 2019

AMERICAN UNIVERSITY OF BEIRUT

THESIS, DISSERTATION, PROJECT RELEASE FORM

Student Name:

DAOUD

Last

YARA

First

NAWAF

Middle

Master's Thesis
Dissertation

Master's Project

Doctoral

I authorize the American University of Beirut to: (a) reproduce hard or electronic copies of my thesis, dissertation, or project; (b) include such copies in the archives and digital repositories of the University; and (c) make freely available such copies to third parties for research or educational purposes.

I authorize the American University of Beirut, to: (a) reproduce hard or electronic copies of it; (b) include such copies in the archives and digital repositories of the University; and (c) make freely available such copies to third parties for research or educational purposes

after : **One** ---- year from the date of submission of my thesis, dissertation, or project.

Two years from the date of submission of my thesis, dissertation, or project.

Three ---- years from the date of submission of my thesis, dissertation, or project.

ara

Signature

wed, August 21st, 2019.

Date

ACKNOWLEDGMENTS

To mom and dad, this thesis is for you. I can never thank you enough for your continuous care, support and truly unconditional love. I am so grateful to have such amazing parents/friends like you, this is more your achievement than it is mine.

I would like to thank every single person who I came across during my path at AUB and who has contributed in one way or another to making this experience unforgettable.

This work is a joint effort with my thesis advisor, Dr. Mayssa Dabaghi. It is the culmination of countless hours spent in her office and thousands of emails and phone calls between us. As my thesis advisor, she has given me invaluable help in enhancing my research and writing skills. She made me realize the importance of perseverance, hard work, attention to detail and most importantly: coding skills!

My gratitude extends to the committee members for their time and help. I would like to thank Dr. Ibrahim Alameddine, in particular, for his insightful feedback and suggestions throughout the course of this study. His door was always open for my numerous and very detailed questions. Dr. Sadek and Dr. Zerbe were the ones who introduced me to Earthquake Engineering, and it was because of them that I decided to pursue a Master's degree in that field.

Heartfelt thanks go to Prof. Mounir Mabsout who has had the utmost impact on my journey at AUB from day one. He has helped and guided me through all the good and the bad. I would like to thank him for believing in me and I hope I lived up to his expectations.

Dozens of people have helped me throughout this emotional rollercoaster. First and foremost, I want to thank my siblings Lili, Farah and Salim for their love, support and overall existence in this world. Thank you for putting up with my nagging, for numerous presentation practices and for providing constant after-midnight rides to and from AUB. The love we have in this household is truly incredible and it has given me the strength to do whatever I set my mind to, including this thesis.

From the bottom of my heart, I would like to extend my thanks and appreciation to my companions in this journey, mainly: Marc, Ruba, Hasnaa, Christelle, Bahaa, Abdallah, and Ghali. The countless days (and all-nighters) spent in the Hydraulics laboratory, our endless pizza and fried chicken meals, the Barbican-sponsored life chats, the continuous rants, and other crazy things I cannot list here (e.g. the infamous Christmas dinner) are forever instilled in my memory. You have all contributed in so many ways to this and I feel our paths will always be intertwined. You have been my backbone through all of this and I will forever be your backbone through everything. This was all possible thanks to Ms. Dima who provided us with a home inside AUB.

A special thank you goes to Mazen who has always been a ray of sunshine in my life. Thank you for always pushing me to be my best and for encouraging me not to give up even when I really wanted to.

As a final note, this study was sponsored by the Pacific Earthquake Engineering Research Center (PEER) and funded by the California Department of Transportation (Caltrans) and the PEER Transportation Systems Research Program. Any opinions, findings and conclusions or recommendations expressed in this material are those of the authors and do not necessarily reflect those of the above-mentioned agencies. We also thank Brian Chiou for providing his racetrack generation codes and Prof. Armen Der Kiureghian for his feedback. These supports are gratefully acknowledged.

AN ABSTRACT OF THE THESIS OF

Yara Nawaf Daoud for Master of Engineering
Major: Civil and Environmental Engineering

Title: Validation and Extension of Synthetic Ground Motion Simulation Procedures

For several years now, synthetic ground motions have been increasingly gaining attention in the field of earthquake engineering. Synthetic ground motion time series can be utilized in a variety of engineering applications including dynamic analysis and probabilistic seismic hazard analysis. However, these synthetic ground motions must capture the important characteristics and natural variability of recorded motions. Several ground motion simulation models and methods have been proposed, ranging from source-based deterministic to site-based stochastic and hybrid models. This study focuses on site-based stochastic models, which are more appealing to practicing engineers, and is comprised of two distinct studies related to synthetic ground motion simulation procedures.

The first study is a validation of different site-based models for simulation of far-field ground motions. Correlations between spectral acceleration values at different periods should be properly represented when computing structural response. Synthetic far-field ground motions using the site-based model proposed by Rezaeian and Der Kiureghian are found to exhibit correlations between spectral periods that are higher than those of the recorded motions and higher than the empirical model of Baker and Jayaram. Variations of this model to reduce the correlations between the spectral periods are also explored. In this study, the effect of these higher correlations on structural response is examined by developing a structural model exhibiting higher mode effects and subjecting it to three different sets of ground motions: one recorded and two synthetic. For this model, results show that higher correlations tend to produce lower variability of structural response which in turn results in non-conservative estimates of seismic risk. Properly accounting for these correlations is expected to improve structural variability estimates.

The second study presents methods to simulate near-fault ground motions for randomized source and site characteristics. It extends the Dabaghi and Der Kiureghian method, which requires information about the source, site, and source-to-site geometry, including directivity parameters. First, an extension is proposed when only the contributing fault, earthquake magnitude, and site location and properties are known. Using Monte Carlo simulation, the possible rupture directivity conditions are accounted for by randomizing rupture geometry and hypocenter location according to their probability distributions. To achieve this, new predictive models that account for variability and correlations are developed for rupture geometry parameters. Then, a second extension which takes as input type-of-faulting, magnitude, source-to-site distance, and site properties is proposed. Here, rupture geometry and both hypocenter and site locations are randomized, allowing comparison of synthetic motions with NGA-West2 models. Results show general agreement between the two.

CONTENTS

ACKNOWLEDGMENTS	V
ABSTRACT.....	VII
LIST OF ILLUSTRATIONS	X
LIST OF TABLES.....	XV
CHAPTER	
I. INTRODUCTION.....	1
A. Motivation, Objective and Scope.....	1
B. Organization of the Thesis	5
II. TOPIC 1: VALIDATION OF DIFFERENT SITE-BASED MODELS FOR SIMULATION OF FAR-FIELD GROUND MOTION	7
A. Introduction, Objectives and Chapter Organization.....	7
B. Ground Motion Catalogs	10
1. Elastic response spectra.....	11
2. Correlations between spectral accelerations.....	12
C. Structural Response	14
1. Structural model	15
2. Initial data bias and correlations.....	16
D. Results and Discussion	19
E. Research Significance and Conclusions	21
III. TOPIC 2: EXTENSION OF NEAR-FAULT GROUND MOTION SIMULATION PROCEDURE	24
A. Introduction, Objectives and Chapter Organization.....	24
B. Stochastic Near-Fault Ground Motion Model and Simulation Method	29
C. Rupture Geometry	30
1. Database of Earthquakes	32
2. Depth to Top of Rupture, <i>ZTOR</i>	33

3. Rupture Dimensions <i>LR</i> and <i>WR</i>	37
4. Location of Rupture Plane within Fault Plane	43
D. Hypocenter Location within Rupture Plane	43
E. Simulation Procedure for Specified Site and Random Hypocenter Location – P1	44
1. Example Application	46
F. Simulation Procedure for Random Site and Random Hypocenter Location – P2 ..	50
1. Example Application	51
G. Conclusions	59
IV. SUMMARY, CONCLUSIONS AND FUTURE WORK .	62
A. Summary of the Study.....	62
B. Major Contributions and Conclusions	63
C. Limitations and Recommendations for Future Studies.....	65
REFERENCES	67
APPENDIX	
A. ILLUSTRATION OF SIMULATION PROCEDURES	73
B. RUPTURE GEOMETRY MODELS – DIAGNOSTIC PLOTS	75
C. P2 SIMULATIONS VS GMPES.....	80

ILLUSTRATIONS

Figure	Page
1. Statistics of recorded and simulated 5% damped elastic response spectra	12
2. Correlations between spectral accelerations at different periods for T_1^* between 0.1 and 5s and $T_2^* = [0.1, 0.2, 0.5, 1, 1.5]$ s.	14
3. Selected structural model.	15
4. Correlations between spectral accelerations at the modal periods of the considered structure.	18
5. Scatter plots of V_b , max response (in kips) with mean and standard deviation of the error term $\epsilon = \ln V_b, \text{maxsimulated} - \ln V_b, \text{maxrecorded}$.	20
6. Scatter plots of V_5 , max response (in kips) with mean and standard deviation of the error term $\epsilon = \ln V_b, \text{maxsimulated} - \ln V_b, \text{maxrecorded}$.	21
7. Directivity parameters (after Somerville et al., 1997).	26
8. Distribution of earthquakes in the considered database with respect to moment magnitude and type of faulting.	32
9. Earthquake magnitude versus depth to top of rupture in the considered database.	33
10. Logistic regression models for $\text{Prob}(Z_{\text{TOR}} > 0)$ against used data.	34
11. Predictive models for $Z_{\text{TOR}} > 0$, with upper limits, against used data.	36
12. Comparison of developed models for LR with WC94 and employed data.	38
13. Comparison of developed models for WR with WC94 and employed data.	39
14. Comparison of resulting $\ln AR - M_w$ scaling relationships with the corresponding data from buried and surface ruptures. The solid lines represent the relationships for buried and surface ruptures below and above their intersections, respectively. The	

- dashed lines represent the relationships for buried and surface ruptures above and below their intersections, respectively. 41
15. Randomization of ZTOR and the rupture dimensions and location (gray rectangular surface) for an $M_w = 6.55$ earthquake on the Upper Elysian Park fault (dashed black rectangle). 48
 16. Randomization of the hypocenter location (black star) along strike (HypX) and down-dip (HypZ) within a fault rupture plane (gray rectangular surface) with fixed rupture geometry of $ZTOR = 3.1$ km, $LR = 16.7$ km and $WR = 18.6$ km. 48
 17. 5% damped RotD50 pseudo-acceleration response spectra of 100 simulated motions (38 pulse-like and 62 non-pulse-like) at the LADT site ($V_{s30} = 390$ m/s) due to an earthquake with $M_w = 6.55$ occurring on the Upper Elysian Park fault, median and median plus and minus one logarithmic standard deviations of the simulations, and examples of one pulse-like motion (from a scenario with $d = 11.2$ km and with $T_p = 2.12$ s) and one non-pulse-like motion (from a scenario with $d = 3.8$ km). 49
 18. Median and median plus and minus one logarithmic standard deviation of 5% damped pseudo-acceleration response spectra of RotD50 component for 600 synthetic motions, median spectra for pulse-like and non-pulse-like synthetic motions, median and median plus and minus one logarithmic standard deviation spectra predicted by a combination of the five NGA-West2 GMPEs, and median spectra predicted by each of the five NGA-West2 GMPEs for two different earthquake scenarios. 54
 19. Median and median plus and minus one logarithmic standard deviation of 5% damped pseudo-acceleration response spectra of RotD50 component for 300 synthetic motions, median spectra for pulse-like and non-pulse-like synthetic

<p>motions, median and median plus and minus one logarithmic standard deviation spectra predicted by a combination of the five NGA-West2 GMPEs, and median spectra predicted by each of the five NGA-West2 GMPEs for a similar earthquake scenario at HW sites (left) and FW sites (middle). The two scenarios are compared in the right panel.</p>	56
<p>20. Median of 5% damped pseudo-acceleration response spectra of the RotD50 component for 600 synthetic motions versus median spectra predicted by the NGA-West2 model for scenarios having same F, $RRUP$, $Vs30$ and $ZTOR$ values but different Mw values.</p>	58
<p>21. Median of 5% damped pseudo-acceleration response spectra of the RotD50 component for 600 synthetic motions versus median spectra predicted by the NGA-West2 model for scenarios having same F, Mw, $Vs30$ and $ZTOR$ values but different $RRUP$ values.</p>	58
<p>22. Median of 5% damped pseudo-acceleration response spectra of the RotD50 component for 600 synthetic motions versus median spectra predicted by the NGA-West2 model for scenarios having same F, Mw, $RRUP$ and $ZTOR$ values but different $VS30$ values.</p>	59
<p>A1. Simulation procedure P1.</p>	A-1
<p>A2. Simulation procedure P2.</p>	A-2
<p>B1. Diagnostic plots of the model for $ZTOR$.</p>	B-1
<p>B2. Plot of the fitted versus observed values of $ZTOR$.</p>	B-1
<p>B3. Diagnostic plots of the model for LR.</p>	B-2
<p>B4. Plot of the fitted versus observed values of LR.</p>	B-2
<p>B5. Diagnostic plots of the model for $WR Ztor = 0$.</p>	B-3

- B6. Plot of the fitted versus observed values of $WR | Z_{tor} = 0$. B-3
- B7. Diagnostic plots of the model for $WR | Z_{tor} > 0$. B-4
- B8. Plot of the fitted versus observed values of $WR | Z_{tor} > 0$. B-4
- C1. Scenario $M_w = 6.5, RRUP = 5 \text{ km}, VS30 = 525 \text{ ms}$ and $ZTOR = 0 \text{ km}$ for $F = 0$ (left) and $F = 1$ (right). C-1
- C2. Scenario $M_w = 6.5, RRUP = 10 \text{ km}, VS30 = 525 \text{ ms}$ and $ZTOR = 0 \text{ km}$ for $F = 0$ (left) and $F = 1$ (right). C-2
- C3. Scenario $M_w = 6.5, RRUP = 20 \text{ km}, VS30 = 525 \text{ ms}$ and $ZTOR = 0 \text{ km}$ for $F = 0$ (left) and $F = 1$ (right). C-2
- C4. Scenario $M_w = 7, RRUP = 5 \text{ km}, VS30 = 525 \text{ ms}$ and $ZTOR = 0 \text{ km}$ for $F = 0$ (left) and $F = 1$ (right). C-3
- C5. Scenario $M_w = 7, RRUP = 10 \text{ km}, VS30 = 525 \text{ ms}$ and $ZTOR = 0 \text{ km}$ for $F = 0$ (left) and $F = 1$ (right). C-3
- C6. Scenario $M_w = 7, RRUP = 20 \text{ km}, VS30 = 525 \text{ ms}$ and $ZTOR = 0 \text{ km}$ for $F = 0$ (left) and $F = 1$ (right). C-4
- C7. Scenario $M_w = 7.5, RRUP = 5 \text{ km}, VS30 = 525 \text{ ms}$ and $ZTOR = 0 \text{ km}$ for $F = 0$ (left) and $F = 1$ (right). C-4
- C8. Scenario $M_w = 7.5, RRUP = 10 \text{ km}, VS30 = 525 \text{ ms}$ and $ZTOR = 0 \text{ km}$ for $F = 0$ (left) and $F = 1$ (right). C-5
- C9. Scenario $M_w = 6.5, RRUP = 10 \text{ km}, VS30 = 525 \text{ ms}$ and $ZTOR = 3 \text{ km}$ for $F = 0$ (left) and $F = 1$ (right). C-5
- C10. Scenario $M_w = 7, RRUP = 10 \text{ km}, VS30 = 525 \text{ ms}$ and $ZTOR = 3 \text{ km}$ for $F = 0$ (left) and $F = 1$ (right). C-6

C11.Scenario $M_w = 6, RRUP = 10 \text{ km}, VS30 = 360 \text{ ms}$ and $ZTOR = 0 \text{ km}$ for $F = 0$ (left) and $F = 1$ (right). C-6

C12.Scenario $M_w = 6.5, RRUP = 10 \text{ km}, VS30 = 760 \text{ ms}$ and $ZTOR = 0 \text{ km}$ for $F = 0$ (left) and $F = 1$ (right). C-7

C13.Scenario $M_w = 7, RRUP = 10 \text{ km}, VS30 = 360 \text{ ms}$ and $ZTOR = 0 \text{ km}$ for $F = 0$ (left) and $F = 1$ (right). C-7

C14.Scenario $M_w = 7.5, RRUP = 10 \text{ km}, VS30 = 760 \text{ ms}$ and $ZTOR = 0 \text{ km}$ for $F = 0$ (left) and $F = 1$ (right). C-8

TABLES

Table	Page
1. Modal periods and static responses of the structure.	16
2. Median spectral accelerations at the modal periods. The differences with respect to the recorded set are listed between parentheses.	17
3. Standard deviation of natural logarithm of spectral accelerations at the modal periods of the considered structure.	17
4. Correlations between spectral accelerations at the modal periods of the considered structure.	18
5. Statistics of the V_b , max response.	20
6. Statistics of the V_5 , max response.	20
7. Estimated correlation matrix of regression residuals of the developed models and their 95% confidence intervals: a) for $ZTOR = 0$; and b) for $ZTOR > 0$. Only the correlation between $\ln LR$ and $\ln WR$ when $ZTOR > 0$ is found to be statistically significant (at the 8% significance level).	42
8. Correlation matrices of regression residuals used in the simulations: a) for $ZTOR = 0$; and b) for $ZTOR > 0$.	42
9. Shape and scale parameters of Weibull distributions for normalized down-dip hypocenter location fitted by Mai et al. (2005).	44
10. Ranges of simulated rupture geometry parameters and calculated distance and directivity parameters.	62

CHAPTER I

INTRODUCTION

A. Motivation, Objective and Scope

For several years now, synthetic ground motions have been increasingly gaining attention in the field of earthquake engineering. Synthetic ground motion time series can be utilized in a variety of engineering applications including linear and non-linear response-history analysis of structures as well as probabilistic seismic hazard analysis (PSHA). In conducting such studies, structural engineers must properly account for the range of earthquake scenarios possible at the site of interest, and for the corresponding ground motion characteristics and variability. While ground motion records might be available at some sites, they are usually scarce at most sites. To overcome this deficiency, engineers resort to selecting ground motions from regions other than that of interest and scaling them to match their target intensity or frequency content. However, this ground motion modification and scaling was shown to introduce a bias in expected structural response (Luco & Bazzurro, 2007) and has thus raised concerns as it can result in unrealistic representations of real ground shaking. An alternative approach to avoid the disadvantages associated with modification and scaling of ground motions is using synthetic ground motions in addition to or instead of recorded ones. Nevertheless, these synthetic ground motions must be able to capture the important characteristics and properly represent the natural variability of recorded motions for the given earthquake source and site characteristics.

Douglas and Aochi (2008) provide an extensive review of the various types of ground motion simulation models that exist. These models can be particularly useful at near-fault sites, where recorded ground motions are often scarce. Ground motion models

can be source- or site-based, deterministic, stochastic or hybrid. Deterministic source-based models, often referred to as physics-based, model the earthquake rupture mechanism and the propagation of seismic waves to the site of interest based on seismological principles (e.g., Dreger, Hurtado, Chopra, & Larsen, 2011; Olsen, Madariaga, & Archuleta, 1997). These models are computationally demanding and necessitate comprehensive knowledge of the source, path, and site characteristics, information that is seldom available to the practicing engineers. Moreover, they can only generate realistic time series at low frequencies (<1 Hz) (Douglas & Aochi, 2008). Stochastic source-based models represent the theoretical shape and scaling of the Fourier amplitude spectrum of the ground motion at a particular site using simple functional forms that represent the source, the path, and the site characteristics (e.g., Boore, 1983). However, these models fail to represent the low-frequency content of recorded ground motions. As for site-based models, they usually are parameterized stochastic models empirically fitted to ground motions recorded at various sites (e.g., Dabaghi & Der Kiureghian, 2018; Rezaeian & Kiureghian, 2010; Vlachos, Papakonstantinou, & Deodatis, 2017). These models are more appealing to design engineers because they are more time-efficient and only require information about source and site characteristics that is typically available (for example, earthquake magnitude, source-to-site distance, and shear-wave velocity of the site). However, these models do not rigorously represent the physics of the earthquake source and wave propagation, and require a large number of recorded motions to obtain statistically significant predictive equations (Douglas & Aochi, 2008). Hybrid approaches try to mitigate the limitations of the above-mentioned models by, for example, combining the low-frequency content simulated using a deterministic source-based model with the high-frequency content simulated using a

stochastic model, which may be source-based or site-based. Examples of hybrid models include the model of Graves and Pitarka (2010). For a more detailed review of existing ground motion models, see Douglas and Aochi (2008) and Dabaghi and Der Kiureghian (2017).

This study focuses on the site-based stochastic models of far-field and near-fault ground motion developed by Rezaeian and Der Kiureghian (2008, 2010a, 2010b, 2012) and by Dabaghi and Der Kiureghian (2014, 2017, 2018), respectively. Rezaeian and Der Kiureghian (2008, 2010a, 2010b, 2012) proposed a parameterized stochastic model of far-field ground motion based on a time and frequency modulated filtered white-noise process. The model can be used to generate horizontal orthogonal pairs of synthetic ground motion time series for given earthquake source and site characteristics. The input information necessary for this simulation procedure consists of the type of faulting (F), moment magnitude (M_w), distance (R_{RUP}), and shear-wave velocity of the site (V_{s30}). The model was validated in terms of statistics of simulated elastic response spectra against both recorded motions and empirical models. Dabaghi and Der Kiureghian (2014, 2017, 2018) proposed a parameterized stochastic model of near-fault ground motion, i.e., ground motion at sites located within 30 km of the fault rupture. The model can be used to generate horizontal orthogonal pairs of synthetic near-fault ground motion time series for specified earthquake source and site characteristics. The near-fault ground motion model is formulated in terms of a relatively small number of physically meaningful parameters and is able to represent characteristics of recorded ground motions including temporal and spectral non-stationarity, inherent variability, and near-fault effects. This method accounts for the near-fault rupture directivity effect and produces pulse-like and non-pulse-like motions in accordance with their observed proportions among recorded

motions. The near-fault ground motion simulation procedure requires as input information about the source, the site, and the source-to-site geometry, namely, F , M_w , R_{RUP} , and V_{s30} , in addition to the depth to the top of the rupture plane Z_{TOR} , and directivity parameters $s_{or}d$ and $\theta_{or}\phi$.

The objective of this thesis is to address some of the limitations of the models and simulation procedures presented. First, this study shows that the far-field simulation procedure developed by Rezaerian and Der Kiureghian (2008, 2010a, 2012) produces synthetic ground motions that exhibit correlations between spectral acceleration values at different periods that are higher than those of recorded motions, and higher than those predicted by empirical correlation models. Proper representation of correlations between spectral amplitudes at different periods is crucial when computing structural responses of multi-degree-of-freedom (MDOF) systems. Therefore, the first aim of this study is to study the effect of these higher correlations on structural response of MDOF systems and to examine if variations of this model would result in more realistic correlations between spectral periods. Moreover, in seismic design or assessment studies, structural engineers may have information about the magnitude and fault source of the earthquakes that contribute most to the hazard at their site of interest. They may or may not have information about the source-to-site distance, but they are not likely to have information about values of the directivity parameters (or even depth to top of rupture), which are needed as input to the near-fault model developed by Dabaghi and Der Kiureghian (2014, 2017, 2018). These input parameters require information about the rupture geometry (dimensions and location) as well as the hypocenter location. To overcome this limitation, the second aim of this study is to develop procedures to simulate the parameters Z_{TOR} , R_{RUP} , $s_{or}d$, and $\theta_{or}\phi$ when they are unknown.

B. Organization of the Thesis

This thesis is organized into four chapters. After this introductory chapter, Chapter 2 presents a validation of two different site-based models for simulation of far-field ground motion in terms of how the correlations between spectral periods that they result in compare with recorded ground motions and empirical correlation models. The first method is the far-field model proposed by Rezaeian and Der Kiureghian (2010a) and the second method is that of the variant of the model proposed by Broccardo and Dabaghi (2017). The effect of correlations between spectral accelerations at different periods on the structural response of multi-degree of freedom systems is also examined. This is done by conducting response history analyses (RHA) on a structural model exhibiting higher mode effects and subjected to three different sets of ground motions: one recorded and two corresponding synthetic sets, one generated using the Rezaeian and Der Kiureghian (2010a) model, and the other generated using the Broccardo and Dabaghi (2017) model.

Chapter 3 presents methods to simulate near-fault ground motions for randomized source and site characteristics by extending the simulation procedure of Dabaghi and Der Kiureghian (2014, 2017, 2018). First, an extension is proposed where only the contributing fault, earthquake magnitude, and site location and properties are known. Using Monte Carlo simulation, the possible rupture directivity conditions are accounted for by randomizing the rupture geometry and the hypocenter location according to their probability distributions. To achieve this, new predictive models that account for variability and correlations are developed for the rupture geometry parameters, by fitting data from earthquakes with available finite-fault models. Then, a second extension that only takes as input the type-of-faulting, magnitude, source-to-site distance, and site properties is proposed. Here, the rupture geometry and both the hypocenter and site

locations are randomized, allowing comparison of synthetic motions with the NGA-West2 models (Gregor et al., 2014).

Chapter 4 summarizes the study with its major objectives and findings, and suggests a number of improvements and further studies that can be undertaken.

CHAPTER II

TOPIC 1: VALIDATION OF DIFFERENT SITE-BASED MODELS FOR SIMULATION OF FAR-FIELD GROUND MOTION

A. Introduction, Objectives and Chapter Organization

Dynamic analysis of any structural system necessitates knowledge of an input ground motion time series to evaluate the seismic demands on that system. The validity of the input ground motion thus ensures the validity of the predicted structural response (Rezaeian & Der Kiureghian, 2012). Therefore, producing realistic synthetic ground motions that well represent real ones is essential for their use in engineering applications.

To validate that ground motion simulation models produce realistic synthetic ground motion time series, their characteristics are compared with those of recorded ground motions (Burks & Baker, 2014). Different validation approaches have been proposed in the literature, where simulations are compared to corresponding records from historical earthquakes or to empirical ground motion prediction equations (GMPEs). A common validation method consists of comparing ground motion intensity measures such as spectral acceleration values from simulated motions to those of historical earthquake recordings (e.g., Aagaard et al., 2008). Other methods include the validation of structural response measures such as peak story drift ratio and residual drift ratio of systems subjected to comparable simulated and recorded ground motions (e.g., Jayaram & Shome, 2012). Also, previous validation efforts tend to compare statistics of synthetic elastic response spectra with their corresponding statistics predicted using the Next Generation Attenuation (NGA) GMPEs (e.g., Frankel, 2009). Given that these GMPEs are based on empirical observations, this method indirectly validates simulation models against recorded ground motions.

A similar approach was adopted for the far-field stochastic model proposed by Rezaeian and Der Kiureghian (2010a, 2012), where the model was validated in terms of the median and standard deviation of the elastic response spectra against both recorded motions and the NGA GMPEs (Abrahamson et al., 2008). However, when higher mode effects are significant in a structure, the joint distribution of spectral acceleration values at multiple periods is also important (Burks & Baker, 2014). Therefore, the correlations between spectral acceleration values at different periods should be properly represented in synthetic motions used to compute structural responses. Correlations produced by the Rezaeian and Der Kiureghian far-field stochastic model have not been validated, and this study shows that it produces synthetic ground motions that exhibit correlations between spectral periods that are higher than those of recorded motions and empirical correlation models.

Recently, many empirical models that estimate the correlation of spectral acceleration values at different periods have been proposed based on actual recorded ground motions. These models differ in complexity, the size of the ground motion database used, and the range of periods covered. A study by Inoue and Cornell (1990) developed a simple linear correlation coefficient model expressed as a function of the difference of the natural logarithm of pseudo-spectral acceleration ($\log S_a$) values at two periods. However, this model cannot be used for short period structures (with fundamental period less than 0.1 sec). Ishida (1993) suggested a similar model but with a constant correlation coefficient at the short period range. More recently, Baker and Jayaram (2008) measured the correlations between spectral acceleration values at different periods of records in the NGA database and developed a more elaborate empirical correlation predictive equation for periods from 0.01 seconds to 10 seconds. The latter model is used

in this study because it was fitted to records from the NGA database, it covers a wide range of periods, and is extensively used in literature.

In efforts to examine the effect of inter-period correlations, a study by Bayless and Abrahamson (2018) on point-source stochastic models concluded that using simulated ground motions that inadequately represent these correlations affects structural response variability and seismic risk; simulated motions that overestimate correlations result in reduced estimates of variability of structural response, which leads to non-conservative estimates of seismic risk. This highlights the importance of validating these correlations in ground motion simulations.

Recently, an extension and improvement on the far-field model of Rezaeian and Der Kiureghian (2010a, 2012) was proposed by Broccardo and Dabaghi (2017). The latter model also employs a modulated filtered white-noise process, but is formulated in the frequency domain and aims to accommodate a broader range of modulating function shapes that allow multiple peaks. It also preserves the integrability of the simulated acceleration time series and insures zero residual velocity and displacement. An analysis conducted in this study of a variant (currently under development) of the model proposed by Broccardo and Dabaghi (2017) shows that it results in correlations that are more consistent with recorded motions.

This chapter aims to evaluate two methods of generating synthetic far-field ground motions in terms of how their correlations between spectral periods compare with those of recorded ground motions and empirical correlation models. The first method is the far-field model proposed by Rezaeian and Der Kiureghian (2010a), thereafter referred to as RD2010 and the second method, thereafter referred to as BD2017, is that of the variant of the model proposed by Broccardo and Dabaghi (2017).

Moreover, another objective of this chapter is to examine the effect of correlations between spectral accelerations at different periods on the structural response of multi-degree of freedom (MDOF) systems. Response history analyses (RHA) are conducted on a structural model exhibiting higher mode effects and subjected to a set of recorded ground motions, a set of corresponding synthetic ground motions from the RD2010 model, and a set of corresponding synthetic ground motions from the BD2017 model. Higher correlations are expected to produce lower variability of structural response which in turn results in non-conservative estimates of seismic risk. Properly accounting for these correlations is expected to improve the estimate of structural variability.

This chapter begins with an overview of the ground motion catalogs used and a comparison of their characteristics. Next, the developed structural model is presented followed by a comparison of the structural responses of the model subjected to the different ground motion catalogs. Finally, conclusions regarding the effect of higher correlations and recommendations for future work are included.

B. Ground Motion Catalogs

The first method of assessing the validity of synthetic ground motions is by comparing their characteristics with those of recorded ground motions (e.g., Burks & Baker, 2014). The statistics of the response spectra of the three catalogs of recorded and simulated ground motions are thus compared in this study.

The recorded ground motions considered are a subset of the NGA-West2 database (Ancheta et al., 2014) that was used in development of RD2010 (Rezaeian and Der Kiureghian, 2010a) and subsequently in the development of BD2017. It consists of 102 pairs of horizontal ground motion components. These records correspond to both strike-

slip and reverse faulting mechanisms with moment magnitude M_w ranging between 6.1 and 7.62, and closest distance to the rupture plane R_{RUP} between 11 and 100 km.

For each of the ground motion records, a ground acceleration time-series is generated using RD2010 with the model parameters directly fitted by (Rezaeian and Der Kiureghian, 2010a) to each of the considered records. Similarly, the parameters of the BD2017 model (Broccardo & Dabaghi, 2017) are fitted to the same recorded ground motions, and time-series are generated using BD2017 with the fitted model parameters. This procedure results in three ground motion catalogs, one recorded and two simulated. Then for each ground motion in each catalog, the elastic 5% damped pseudo-acceleration response spectrum $S_a(T)$ is calculated for periods T between 0.1 s and 10 s.

The compared statistics include the median level and standard deviation of the pseudo-acceleration elastic response spectra, as well as the correlations between pseudo-spectral accelerations at different periods.

1. Elastic response spectra

Figure 1 compares the median and median plus and minus one logarithmic standard deviation levels of the elastic response spectra of the three considered catalogs. Statistics of the synthetic motions generally agree with those of recorded ones, where no major differences are observed and the trends are mostly consistent. For short periods ($T < 0.4s$), BD2017 underestimates spectral accelerations while RD2010 tends to slightly overestimate them. For mid-range periods, both simulated motion catalogs tend to marginally underestimate spectral accelerations, while for larger periods ($T > 2s$) the medians of the three considered catalogs are similar.

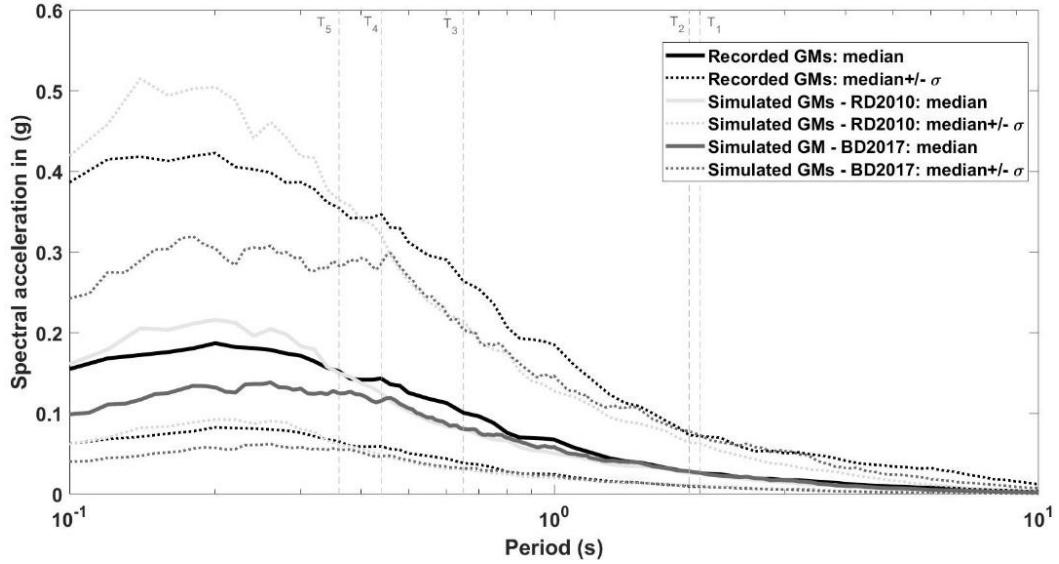


Figure 1. Statistics of recorded and simulated 5% damped elastic response spectra.

Note that the ground motions simulated using the BD2017 model and fitted model parameters were scaled down such that the median response spectrum of the BD2017 catalog matches that of RD2010 in the period range 0.5-2 s, which contains the first three modal periods of the structure considered in this chapter. This was done by multiplying all the response spectra of the BD2017 catalog by a constant factor of 0.72 to ensure that the ground motion catalogs are consistent within that range and subsequently that the differences in structural response are mainly due to the effect of correlations. The scaled ground motions are used throughout this study.

2. Correlations between spectral accelerations

Following Baker and Jayaram (2008), the correlations between spectral accelerations at different periods are calculated for the given three catalogs. The following procedure is adopted to estimate the correlation between spectral accelerations at periods T_1^* and T_2^* . For each catalog, and for each ground motion, the error term $\epsilon(T) = \ln S_a(T) - \mu_{\ln S_a}(T)$ is calculated at all periods, where $\mu_{\ln S_a}(T)$ is the mean of the natural

logarithm of the pseudo-acceleration response spectra of that catalog at period T . Then, Equation 1 is used to estimate the correlations between the error terms at any two spectral periods T_1^* and T_2^* :

$$\rho_{\epsilon(T_1^*), \epsilon(T_2^*)} = \frac{\sum_{i=1}^n (\epsilon_i(T_1^*) - \overline{\epsilon(T_1^*)})(\epsilon_i(T_2^*) - \overline{\epsilon(T_2^*)})}{\sqrt{\sum_{i=1}^n (\epsilon_i(T_1^*) - \overline{\epsilon(T_1^*)})^2 \sum_{i=1}^n (\epsilon_i(T_2^*) - \overline{\epsilon(T_2^*)})^2}}, \quad (1)$$

where n is the total number of records in the considered catalog, $\epsilon_i(T_1^*)$ and $\epsilon_i(T_2^*)$ are the i th realizations of $\epsilon(T_1^*)$ and $\epsilon(T_2^*)$ respectively, and $\overline{\epsilon(T_1^*)}$ and $\overline{\epsilon(T_2^*)}$ are the respective means. The procedure is repeated for any period pair of interest and for all three catalogs.

Figure 2 compares the correlations calculated from recorded ground motions with those calculated from a) ground motions simulated using RD2010, b) ground motions simulated using BD2017 and c) the empirical predictive equation by Baker and Jayaram [see Baker and Jayaram (2008) for details of the model formulation which are not included in this thesis for brevity].

Several observations can be made from these plots. First, the ground motions simulated using RD2010 show much higher correlations between spectral accelerations at different periods than the recorded ground motions for most of the considered periods. This difference is most pronounced at higher periods or when the two considered periods are not closely-spaced. Second, the ground motions simulated using BD2017 generally show lower correlations than their RD2010 simulated counterparts and better agree with the recorded ground motions (but are still higher). Finally, the empirical model tends to underestimate the correlations of the recorded ground motions for all the considered periods. This difference between the recorded motions and the empirical model could be

because the empirical model is fitted to a database that includes a larger number of recorded motions and from a wider range of magnitudes and distances.

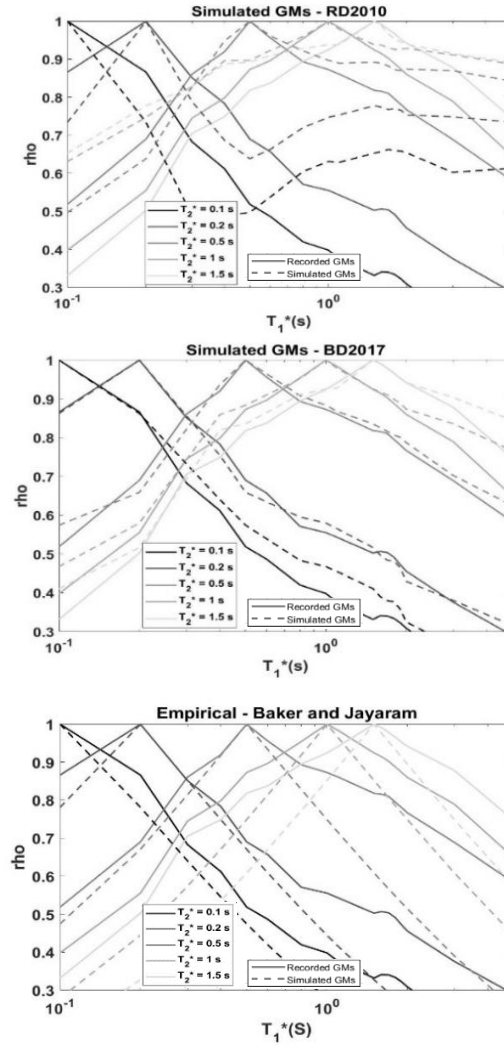


Figure 2. Correlations between spectral accelerations at different periods for T_1^* between 0.1 and 5s and $T_2^* = [0.1, 0.2, 0.5, 1, 1.5]$ s.

The following sections study and discuss the possible effect of the observed differences in correlations on the structural response of a given system.

C. Structural Response

The joint distribution of spectral acceleration values at multiple periods is important when higher mode effects are significant in a structure (Burks & Baker, 2014).

To examine the effect of properly accounting for correlations on structural response, a simple structural model exhibiting higher mode effects is developed and subjected to the three sets of recorded and simulated ground motions presented earlier.

1. Structural model

The structure considered is a two-dimensional four-story frame with an appendage, represented in Figure 3. The masses lumped at the level of each floor are $m = 100$ kips and the mass of the appendage is $m_5 = 0.01 m$. The floor lateral stiffnesses are $k = 22.6$ kips/in and the lateral stiffness of the appendage is $k_5 = 0.0012 k$. The frame is modeled as having rigid floors and thus a total of 5 dynamic degrees of freedom ($N = 5$). This particular model is selected since it is presumed to exhibit higher mode effects [see section 13.2.7 of Chopra (2017) for more details on the model].

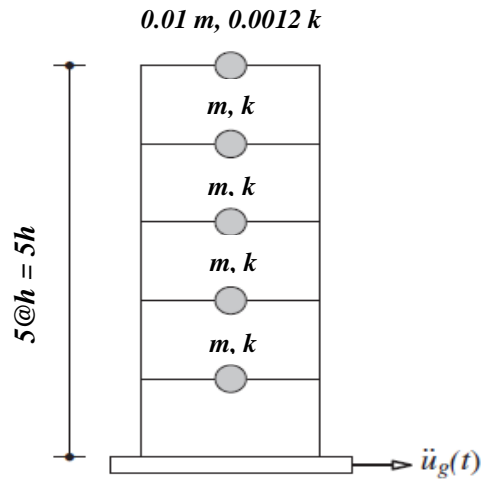


Figure 3. Selected structural model.

This structure is analyzed using RHA whereby the earthquake response of a multistory structure to a given ground motion is the combination of responses due to all the modes (Chopra, 2017) as follows:

$$r(t) = \sum_{n=1}^N r_n(t) = \sum_{n=1}^N r_n^{st} A_n(t) \quad (2)$$

where r_n^{st} is the n th-mode modal static response determined by static analysis of the structure and $A_n(t)$ is the pseudo-acceleration response of the n th-mode single-degree-of-freedom (SDOF) system calculated based on the considered ground motion. Note that the n th-mode spectral ordinate $S_a(T_n) = \max_t |A_n(t)|$, where T_n is the n th-mode period.

In this study, two responses are evaluated: base shear V_b and top-story shear V_5 (at the 5th story for the given structure). Statistics of these responses obtained from each of the three catalogs are compared in the next sections. Table 1 summarizes the five modal periods of the considered structure and the modal static responses.

Table 1. Modal periods and static responses of the structure.

Mode n	1	2	3	4	5
T_n (s)	2.0	1.9	0.65	0.44	0.36
$\frac{V_{b_n}^{st}}{m}$	1.95	1.63	0.33	0.08	0.02
$\frac{V_{5_n}^{st}}{m_5}$	9.94	-8.98	0.05	-0.01	0.0001

2. Initial data bias and correlations

To be able to study the effect of correlations alone, initial bias in the data must be eliminated (i.e. statistics of recorded and simulated ground motions must generally agree). The median and median plus and minus one logarithmic standard deviation levels of the elastic response spectra of the three considered catalogs were generally compared and discussed in Figure 1. Moreover, median spectral acceleration values from the three sets with the difference between the simulated and recorded sets at the five modal periods of the considered structure are listed in Table 2, and the standard deviations of the natural logarithms of the spectral accelerations at the five modal periods are listed in Table 3. It can be observed from Table 2 that for the modal periods of the considered structure, the highest absolute difference between medians of recorded and simulated ground motions

is 0.019 g at $T_3 = 0.65$ s in the case of RD2010 and 0.027 g at $T_5 = 0.36$ s in the case of BD2017. The differences are negligible at the first two modes, which contribute most to the total response. Moreover, it can be observed from Table 3 that the standard deviations in the BD2017 catalog are consistent with those of the recorded catalog, especially at the first two modes, while the standard deviations in the RD2010 catalog are slightly below those of the recorded catalog at the first two modes. The lower standard deviations might contribute to an underestimation of the structural response variability when RD2010 is used. Therefore, while the differences between the median elastic response spectra of the three catalogs are negligible, the differences in standard deviations make it harder to study the effect that higher correlations between spectral accelerations, alone, have on structural response.

Table 2. Median spectral accelerations at the modal periods. The differences with respect to the recorded set are listed between parentheses.

$S_a(T)$ (g)	T_n (s)				
	2.0	1.9	0.65	0.44	0.36
Rec	0.026	0.026	0.101	0.143	0.152
RD2010	0.026 (0.00)	0.026 (0.00)	0.082 (-0.019)	0.125 (-0.018)	0.150 (-0.002)
BD2017	0.026 (0.00)	0.028 (0.002)	0.081 (-0.020)	0.116 (-0.027)	0.125 (-0.027)

Table 3. Standard deviation of natural logarithm of spectral accelerations at the modal periods of the considered structure.

σ	T_n (s)				
	2.0	1.9	0.65	0.44	0.36
Rec	1.026	1.020	0.962	0.884	0.846
RD2010	0.892	0.902	0.961	0.944	0.889
BD2017	1.023	1.016	0.931	0.904	0.818

The correlations between spectral accelerations are now calculated for a vector T_2^* of the modal periods of the adopted structure, which range between 0.36 s and 2 s. Plots of these correlations for recorded and simulated ground motions are shown in Figure 4, and their values are documented in Table 4.

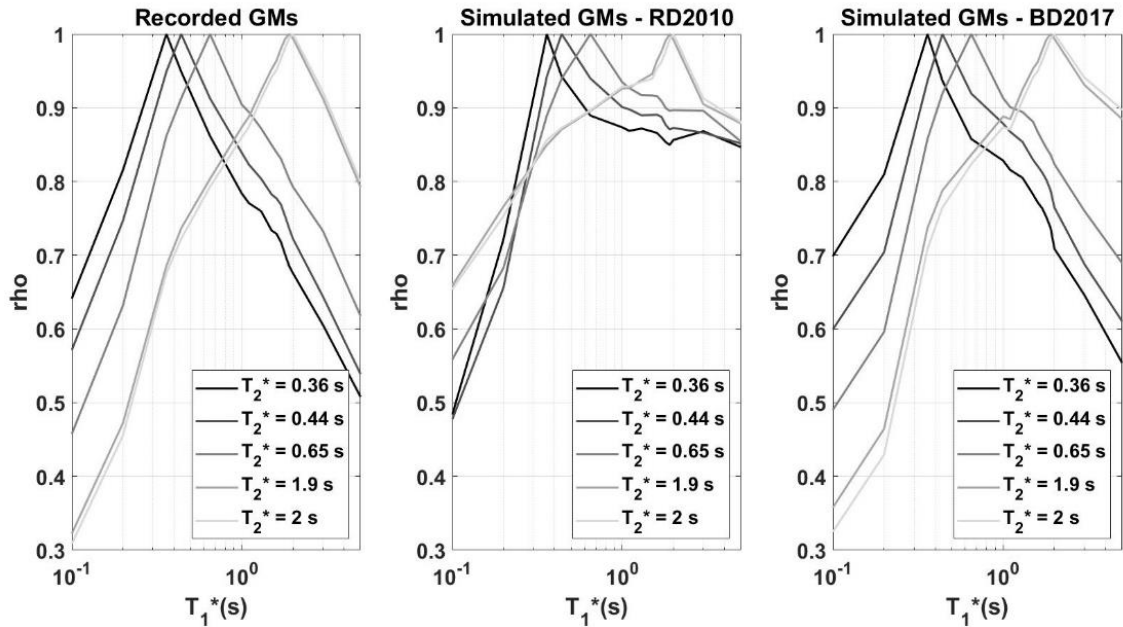


Figure 4. Correlations between spectral accelerations at the modal periods of the considered structure.

Table 4. Correlations between spectral accelerations at the modal periods of the considered structure.

Recorded					
<i>RD2010</i>	T_1	T_2	T_3	T_4	T_5
<i>BD2017</i>					
T_1	1.00	0.99	0.79	0.72	0.68
		0.99	0.90	0.87	0.86
		0.99	0.82	0.76	0.71
T_2		1.00	0.80	0.74	0.69
			0.90	0.87	0.85
			0.84	0.79	0.74
T_3			1.00	0.91	0.86
				0.94	0.89
				0.92	0.86
T_4				1.00	0.95
					0.94
T_5					1.00

It can be observed from Figure 4 that while the correlations between error terms range from 0.3 to 1 for recorded motions for periods T_1^* between 0.1 and 5 s, the lowest correlation is about 0.5 for the RD2010 simulated motions. For periods above 0.3 s, RD2010 ground motions show correlations greater than 0.8 for all periods. On the other hand, the correlations of the BD2017 ground motions are in general agreement with those of recorded motions, whereby the two catalogs have similar values and follow the same trends. In particular, Table 4 shows that the spectral correlations of the BD2017 ground motions at the modal periods of the structure are comparable to or slightly larger than the spectral correlations of the recorded motions at all pairs of periods. As for the spectral correlations of the RD2010 ground motions, they are even larger than those of the BD2017 ground motions at all the modal period pairs.

D. Results and Discussion

The need for consideration of correlations between spectral accelerations at different periods is tested by comparing the structural response of the given structural model subjected to the recorded and synthetic ground motions. RHA are performed on the structural model subjected to the ground motions in each of the three catalogs.

For each recorded and simulated ground motion, the responses $V_{b,max} = \max_t |V_b(t)|$ and $V_{5,max} = \max_t |V_5(t)|$ are calculated. Some statistics of $V_{b,max}$ and $V_{5,max}$ are listed in Table 5 and Table 6, respectively, for each of the three ground motion catalogs. Figure 5 shows scatter plots of $V_{b,max}$ responses from simulated versus recorded ground motions for each of the RD2010 and BD2017 simulated catalogs. Figure 6 shows similar plots for $V_{5,max}$.

Table 5. Statistics of the $V_{b,max}$ response.

$V_{b,max}$ (kips)	Recorded GMs	Simulated GMs – RD2010	Simulated GMs – BD2017
Min	0.46	0.72	0.44
Max	199	96	102
Median	4.77	4.36	4.91
σ	16.42	10.85	12.62

Table 6. Statistics of the $V_{5,max}$ response.

$V_{5,max}$ (kips)	Recorded GMs	Simulated GMs – RD2010	Simulated GMs – BD2017
min	0.01	0.02	0.02
max	3.61	1.41	1.82
median	0.08	0.09	0.08
σ	0.29	0.18	0.22

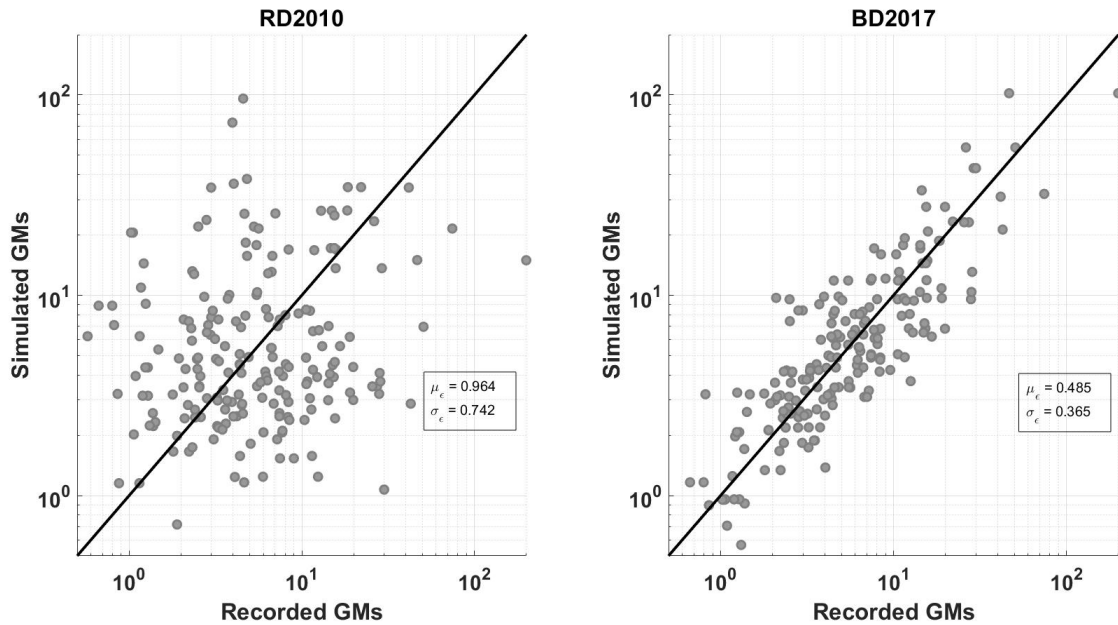


Figure 5. Scatter plots of $V_{b,max}$ response (in kips) with mean and standard deviation of the error term $\epsilon = |\ln(V_{b,max}^{simulated}) - \ln(V_{b,max}^{recorded})|$.

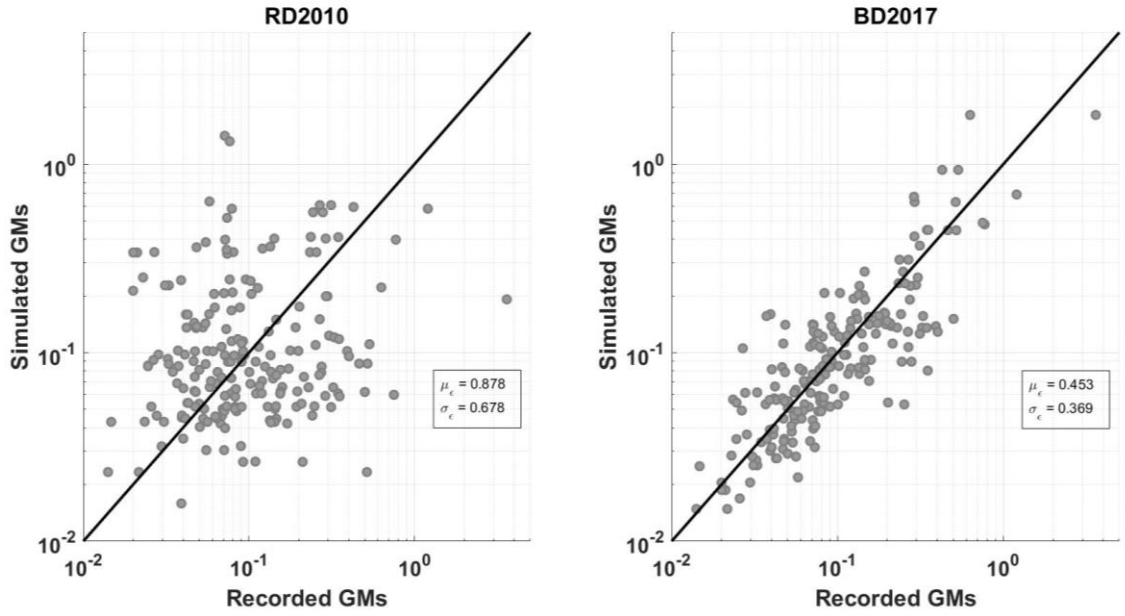


Figure 6. Scatter plots of $V_{5,max}$ response (in kips) with mean and standard deviation of the error term $\epsilon = |\ln(V_{b,max}^{simulated}) - \ln(V_{b,max}^{recorded})|$.

Structural response using BD2017, which better captures both the standard deviation of elastic response spectra and the correlations between spectral accelerations of recorded motions, shows median values slightly above those of recorded motions but closer than RD2010. Moreover, for both of the considered responses, BD2017 provides estimates of the variability of structural response that are closer to those of recorded motions, whereas it can be clearly observed that the RD2010 model largely underestimates this variability. This is consistent with the findings of Bayless and Abrahamson (2018) who concluded that overestimating correlations between spectral accelerations in simulated motions results in reduced estimates of variability of structural response leading to non-conservative estimates of seismic risk.

Additionally, scatter plots of Figure 5 and Figure 6 show that structural responses to the BD2017 ground motions are in better agreement with responses to the recorded motions. BD2017 results in lower mean and standard deviation of the error term $\epsilon = |\ln(V_{simulated}) - \ln(V_{recorded})|$ than RD2010 for both $V_{b,max}$ and $V_{5,max}$. Therefore,

properly accounting for correlations between spectral accelerations in synthetic motions is able to better capture the characteristics of the structural response obtained using recorded motions.

E. Research Significance and Conclusions

The most common validation metrics of synthetic ground motions are the median and logarithmic standard deviations of the spectral acceleration values in the range of periods of interest. This study aims to demonstrate the importance of also checking and validating the correlations between spectral accelerations at different periods produced by ground motion simulation procedures, especially if the generated ground motions are to be used for response history analysis of structures with higher mode contributions. This is particularly relevant to design engineers who want to use synthetic motions in structural response history analyses for probabilistic seismic risk and performance assessment (Baker, 2007; Baker & Cornell, 2006).

After conducting seismic response history analysis on a structural model subjected to three different catalogs of recorded and simulated ground motions, a study of the effect of properly accounting for spectral correlations is conducted by comparing the structural responses to these different catalogs. Results show that properly accounting for correlations between spectral accelerations at different periods is in fact essential in ground motion simulation. For the particular structural model and response quantities considered in this study, higher correlations between spectral accelerations (combined with lower standard deviations of elastic response spectra) result in significant underestimation of the variability of structural response. On the other hand, adequately accounting for correlations results in a larger variability of structural response that is

closer to, but still lower than, that obtained using recorded motions. It also results in estimates of the median of structural response that are closer to those from recorded ground motions. However, the difference in response variability could also be contributed to by the difference in standard deviation of the elastic response spectra, but the current study is unable to separate the two effects. Therefore, further work is recommended: (1) eliminating differences in the standard deviation of the elastic response spectra such that the effect of higher correlations can be separately analyzed; and (2) analyzing a structure exhibiting higher mode effects but having modal periods that are not closely spaced. The latter study is important because having larger differences in correlations (e.g. between the first two modal periods which are closely-spaced in this example) can produce even more pronounced results. In summary, further work should be conducted to provide more conclusive results on the effect of higher correlations on seismic risk.

CHAPTER III

TOPIC 2: EXTENSION OF NEAR-FAULT GROUND MOTION SIMULATION PROCEDURE

A. Introduction, Objectives and Chapter Organization

Near-fault ground motions tend to be more complex and more variable than far-field ground motions and may possess distinct characteristics such as the rupture directivity, hanging-wall effects and the fling step. The rupture directivity effect depends on the direction, length and velocity of rupture propagation relative to a considered site (Somerville, Smith, Graves, & Abrahamson, 1997). When the rupture front propagates towards the site at a velocity almost equal to the shear-wave velocity of the ground, all the seismic energy radiated from the fault rupture tends to arrive at the site in a single, large-amplitude, short-duration pulse – the so-called forward directivity pulse – in the fault-normal direction. If the rupture propagates away from the site, the site is in the backward directivity region and typically records a small amplitude, long-duration ground motion in the fault-normal direction.

Seismic risk and performance assessment of structures located near active faults should account for the distinct near-fault characteristics. Given the scarcity of recorded near-fault ground motions from larger magnitude events and exhibiting near-fault effects, synthetic ground motions can be used in seismic assessment studies in addition to or in place of recorded motions. However, these synthetic ground motions must be able to capture the important characteristics of near-fault ground motions and properly represent the natural variability of recorded motions for given earthquake source and site characteristics.

Several ground motion time series simulation techniques have been proposed. For example, deterministic physics-based (or source-based) techniques explicitly model the rupture process at the seismic source, propagate the resulting seismic waves, and determine the site response (e.g., Hartzell, Guatteri, Mai, Liu, & Fisk, 2005). Through the use of a 3D velocity model, these methods can capture the local wave-propagation effects and naturally represent the amplification of the ground motion in sites susceptible to forward directivity and basin effects. However, the generated synthetic motions typically lack high frequency components beyond approximately 1 Hz. To address this shortcoming, hybrid techniques are used by adding high-frequency stochastic components to the physics-based synthetic (see, e.g., Graves & Pitarka, 2016). Furthermore, this approach requires a precise definition of the fault and rupture geometry and is computationally demanding.

Dabaghi and Der Kiureghian (2014, 2017, 2018) proposed a site-based stochastic model and simulation procedure to generate orthogonal horizontal components of synthetic near-fault ground motions for specified earthquake source and site characteristics. This method accounts for the rupture directivity effect and produces pulse-like and non-pulse-like motions in accordance with their observed proportions among recorded motions. The model requires specification of the source (type-of-faulting F , magnitude M_w , depth to the top of the rupture plane Z_{TOR}), the shear-wave velocity of the top 30 m of soil at the site (V_{s30}), and the source-to-site geometry (closest distance R_{RUP} , directivity parameters $s_{or}d$ and $\theta_{or}\phi$). As illustrated in Figure 7, depending on the nature of the fault, the directivity parameter $s_{or}d$ describes the length s or width d of the portion of the rupture that propagates between the hypocenter and the site in the direction of the slip, and directivity parameter $\theta_{or}\phi$ describes the angle θ in a horizontal plane between

the fault rupture plane and the direction between the epicenter and the site, or the angle ϕ in a vertical plane between the fault rupture plane and the direction between the hypocenter and the site. Parameters s and θ are used for strike-slip faulting, while d and ϕ are used for dip-slip faulting (Somerville et al., 1997). The directivity parameters affect the probability that a ground motion is pulse-like and, if so, the amplitude and period of the pulse.

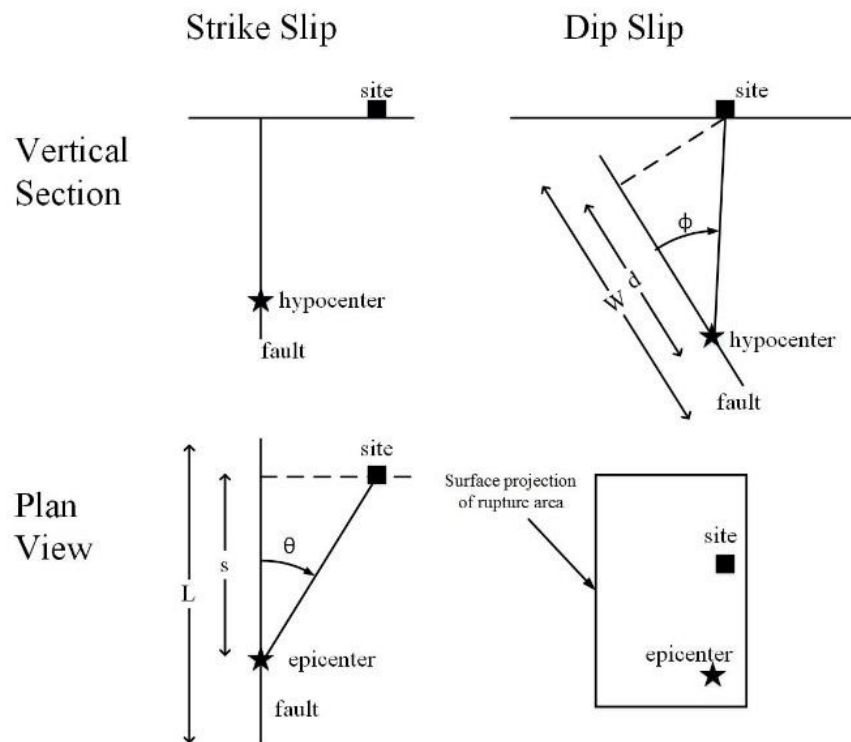


Figure 7. Directivity parameters (after Somerville et al.,1997).

Ground-motion prediction equations (GMPEs) originally developed as part of the Next Generation Attenuation (NGA)-West2 project (Bozorgnia et al., 2014) do not explicitly include the directivity effect, except those proposed by Chiou and Youngs (2014). More recently, five directivity models were developed based on the NGA-West2 ground motion database and numerical simulations of large earthquakes (Spudich & Chiou, 2013). Comparisons of these models showed that their predictions include high

variability and strongly depend on the individual assumptions, especially for non-strike-slip faults. These models are not considered sufficiently developed to be incorporated into the GMPEs and, therefore, further studies have been recommended (Spudich et al., 2013; 2014).

As previously mentioned, the near-fault simulation procedure of Dabaghi and Der Kiureghian (2014, 2017, 2018) requires as input the parameter set $(F, M_w, Z_{TOR}, R_{RUP}, V_{S30}, s_{or}d, \theta_{or}\phi)$. To perform seismic design or assessment studies at a site with known location and V_{S30} , structural engineers can obtain information about the magnitude M_w , the distance R_{RUP} , and the source faults of earthquakes that contribute most to the hazard from deaggregation of probabilistic seismic hazard analysis (PSHA), e.g., as provided by the USGS unified hazard tool (U. S. Geological Survey (USGS), 2019). However, structural engineers are not likely to have information about the parameters $s_{or}d, \theta_{or}\phi$, or even Z_{TOR} . These input parameters require information about the rupture geometry (dimensions and location) as well as the location of the hypocenter. The objective of this study is to develop procedures to simulate the parameters $Z_{TOR}, R_{RUP}, s_{or}d$, and $\theta_{or}\phi$, when they are unknown, in order to generate pairs of horizontal components of synthetic near-fault ground motions using the model and simulation procedure of Dabaghi and Der Kiureghian (2014, 2017, 2018). Two slightly different procedures to simulate these input parameters are proposed.

The first procedure (P1) is used to randomly generate $(Z_{TOR}, R_{RUP}, s_{or}d, \theta_{or}\phi)$ for a specified site, given (F, M_w) of the earthquake, the geometry of the contributing fault (location, strike, dip, maximum dimensions), and the location of the site. This is achieved in a Monte Carlo simulation framework by randomizing the fault rupture geometry, its location within the fault plane, and the hypocenter location within the

rupture plane, based on their respective probability distribution models. First, the rupture geometry is simulated using distributions of the rupture length L_R , rupture width W_R , and Z_{TOR} . These distributions are developed herein using regression analysis on a subset of earthquakes in the NGA-West2 database. Next, the location of the rupture plane is randomized within the fault plane. The hypocenter location along the strike and down-dip is then simulated based on the model developed by Mai, Spudich, and Boatwright (2005). Finally, the coordinates of the site and of the simulated rupture plane and hypocenter are used to calculate R_{RUP} and the directivity parameters s_{ord} and $\theta_{or}\phi$. This tool is particularly useful for structural engineers, who wish to simulate sets of acceleration time series for a particular site of interest and use them in seismic design or assessment studies.

The second procedure (P2) is used to generate $(s_{ord}, \theta_{or}\phi)$ given $(F, M_w, R_{RUP}, Z_{TOR})$ and the dip angle of the fault, in order to compare the near-fault synthetic ground motions with NGA-West2 models. This too is achieved in a Monte Carlo simulation framework, this time by randomizing the fault rupture geometry, the hypocenter location within the rupture plane, and also the site location. The rupture geometry and hypocenter location are simulated in a manner similar to the first procedure, while the site location is sampled from a uniform distribution along the locus of points located at a distance R_{RUP} from the simulated fault rupture. The reader is referred to Appendix A for an illustrated description of the developed procedures.

The chapter first provides a brief review of the stochastic near-fault ground motion model and simulation method developed by Dabaghi and Der Kiureghian (2014, 2017, 2018). We then develop predictive models for the rupture geometry parameters L_R , W_R and Z_{TOR} in terms of the earthquake magnitude and type-of-faulting, and compare these to similar models in the existing literature. The hypocenter location model developed by

Mai et al. (2005) and adopted in this study is then briefly presented. Next, procedure P1 is described and illustrated by simulating ground motions for a specified site given only (F, M_w) and the geometry of the contributing fault. Then, the simulation procedure P2, which generates $(s_{or}d, \theta_{or}\phi)$ given $(F, M_w, R_{RUP}, Z_{TOR})$ and the dip angle of the fault, is described. Finally, near-fault ground motions simulated using P2 are compared with the NGA-West2 GMPEs.

B. Stochastic Near-Fault Ground Motion Model and Simulation Method

Dabaghi and Der Kiureghian (2014, 2017) developed a site-based parameterized stochastic model of near-fault ground motion in two orthogonal horizontal directions. The model is defined in terms of a set of physically meaningful parameters that represent the important amplitude, duration and frequency content characteristics of recorded near-fault ground motions. It accounts for the rupture directivity effect and considers both pulse-like and non-pulse-like motions. Dabaghi and Der Kiureghian (2014, 2018) also presented a procedure to use this model to generate suites of horizontal pairs of synthetic near-fault ground motions for specified earthquake scenarios. The model was fitted to PEER's NGA-West2 database of near-fault recordings to obtain empirical 'observations' of the model parameters, and empirical predictive equations were constructed for the model parameters in terms of earthquake source and site characteristics $(F, M_w, Z_{TOR}, R_{RUP}, V_{s30}, s_{or}d, \theta_{or}\phi)$. The variability of the model parameters and the statistical correlation between them were estimated. The procedure for generating a suite of ground motions for a specified set of earthquake source and site parameters $(F, M_w, Z_{TOR}, R_{RUP}, V_{s30}, s_{or}d, \theta_{or}\phi)$ using the stochastic model and the predictive equations of the model parameters is described in Dabaghi and Der Kiureghian (2018). In this procedure, the empirical model

of the probability of occurrence of the directivity pulse proposed by Shahi and Baker (2014) is used to generate pulse-like and non-pulse-like ground motions in appropriate proportions. The resulting motions were shown to have realistic time series and to reproduce the important features of recorded near-fault ground motions, including the directivity effect and the natural variability.

C. Rupture Geometry

In this thesis, the goal is to generate the input parameters (Z_{TOR} , R_{RUP} , s_{ord} , $\theta_{or}\phi$) according to realistic distributions that are consistent with the physics of the earthquake rupture process. The rupture itself is a complex phenomenon that is usually idealized as a circular or rectangular plane area. The rupture starts at the hypocenter and propagates in one or both directions at a velocity V_r . The distribution of slip over the rupture plane is heterogeneous; patches that undergo large slip and stress drop are distributed over the rupture plane and are surrounded by patches that do not slip. Modeling details of the rupture process, e.g., rupture dimensions, rupture propagation, stress drop and slip distributions, rise time, etc., is a major component of physics-based ground motion modeling. Various approaches have been proposed by seismologists to idealize and model the rupture process (e.g., Graves & Pitarka, 2016; Hartzell et al., 2005), but major uncertainties remain in understanding the process, constraining the various model parameters, and understanding the relations between them.

On the other hand, the site-based model only requires knowledge of the geometry and coordinates of the fault rupture and the location of the hypocenter to calculate (Z_{TOR} , R_{RUP} , s_{ord} , $\theta_{or}\phi$) for a given site. In this study, the rupture is assumed to be rectangular, defined by its length L_R and width W_R . Various models have been proposed to describe

how simple parameters that describe the rupture geometry (such as length, width, aspect ratio, and area) scale with magnitude or vice versa (e.g., Ellsworth, 2003; Hanks & Bakun, 2002; Leonard, 2010; Shaw, 2009; Wells & Coppersmith, 1994). These models employ various functional forms and are developed by regression analysis using diverse historical datasets of earthquakes from different tectonic regimes. They result in large differences in the predicted rupture dimensions for a given M_w . Furthermore, these models predict the rupture length and width independently, without accounting for possible correlation between them. Moreover, they do not account for possible differences in rupture geometry between buried and surface ruptures.

Fewer studies are available for predicting Z_{TOR} . Gupta (2006) used a deterministic value $Z_{TOR} = 3$ km, independent of M_w ; Campbell et al. (2009) used a median estimate of Z_{TOR} that depends on M_w , while Kaklamanos, Baise, and Boore (2011) estimated Z_{TOR} based on hypocentral depth, down-dip rupture width W_R and dip angle δ , assuming a deterministic hypocenter location at 60% down W_R . Chiou and Youngs (2014) proposed a model that relates the mean of Z_{TOR} to M_w and type-of-faulting. They use this mean estimate in the NGA West2 GMPE that they developed. However, their model does not account for the variability of Z_{TOR} .

In this study, new predictive models are developed for Z_{TOR} , L_R , and W_R , while accounting for their variability and for correlations between them. These models are developed using the R open-source software for statistical computing (R Core Team, 2017). F and M_w are considered as the predictor variables, but consideration is also given to the dip angle of the fault and the seismogenic depth (thickness of the crust), if they are available. Possible differences in rupture dimensions between buried ruptures ($Z_{TOR} > 0$)

and surface ruptures ($Z_{TOR} = 0$) are also considered. The study is limited to crustal earthquakes in active tectonic regions.

1. Database of Earthquakes

A subset of earthquakes documented in the PEER NGA West2 database (PEER, 2013) is used to fit the rupture geometry models. The data is for $5.2 \leq M_w \leq 7.9$ and provides the rupture geometry and dimensions for each earthquake, as determined by inversion of seismic waveforms. The dataset used includes earthquakes from strike-slip (SS), reverse (REV) and normal (N) faulting mechanisms. Figure 8 is a scatter plot showing the distribution of earthquakes in the considered database with respect to moment magnitude and type-of-faulting, where $F = 0, 1$ and 2 correspond to SS, REV, and N faults respectively. Note that data from normal and normal-oblique faults are combined throughout the analysis, similarly for data from reverse and reverse-oblique faults.

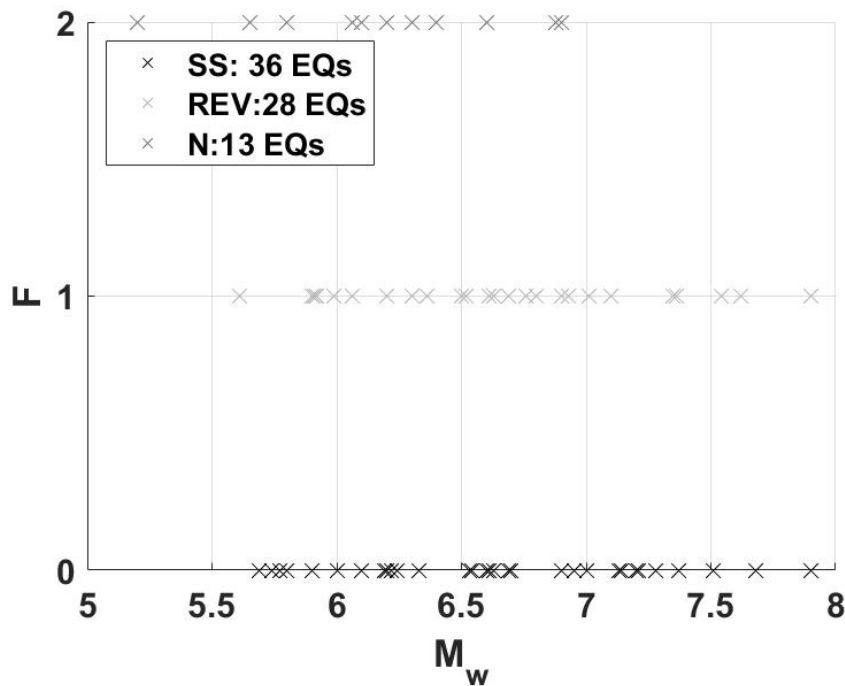


Figure 8. Distribution of earthquakes in the considered database with respect to moment magnitude and type of faulting.

2. Depth to Top of Rupture, Z_{TOR}

Explanatory data analysis indicates that Z_{TOR} is zero-inflated, i.e., the zero value is frequently observed, as can also be seen in Figure 9. Thus, the value of Z_{TOR} is used in this study to classify ruptures as surface or buried: $Z_{TOR} = 0$ corresponds to a surface rupture, i.e., the rupture extends to the Earth's surface, while $Z_{TOR} > 0$ corresponds to a buried rupture, i.e., the rupture does not reach the surface. We note that other references define surface ruptures differently. For example, Kagawa, Irikura, and Somerville (2004) define a rupture having clear surface dislocation and significant slip as a surface rupture, and as a buried rupture otherwise.

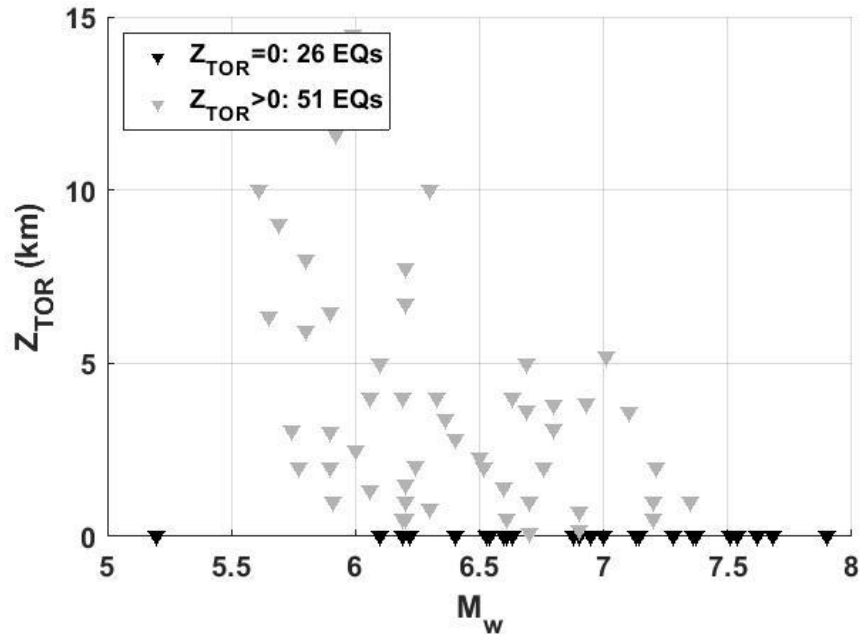


Figure 9. Earthquake magnitude versus depth to top of rupture in the considered database.

Since a simple linear regression model cannot account for the zero-inflation in Z_{TOR} , a two-part model that represents the zero and non-zero values as two separate processes is employed. The first part of the model uses logistic regression to predict the probability that $Z_{TOR} > 0$, while the second is a linear regression model that predicts the

mean and the variability of the non-zero data. While developing the predictive models for Z_{TOR} , it was found that the Z_{TOR} data from normal faulting is not statistically different from data from strike-slip faulting, nor that from reverse faulting. This could be due to the limited number of normal earthquakes in the considered database. Following Chiou and Youngs (2014), in this study the data from normal faulting is combined with the data from strike-slip faulting to fit the Z_{TOR} models.

The fitted logistic regression model, having a pseudo R^2 value of 0.26, is given by:

$$Prob(Z_{TOR} > 0) = \begin{cases} \frac{1}{1 + e^{(-15.293 + 2.293M_w)}}, & \text{for SS and N} \\ \frac{1}{1 + e^{(-17.220 + 2.293M_w)}}, & \text{for REV,} \end{cases} \quad (3)$$

and is plotted in Figure 10 alongside the data used for fitting.

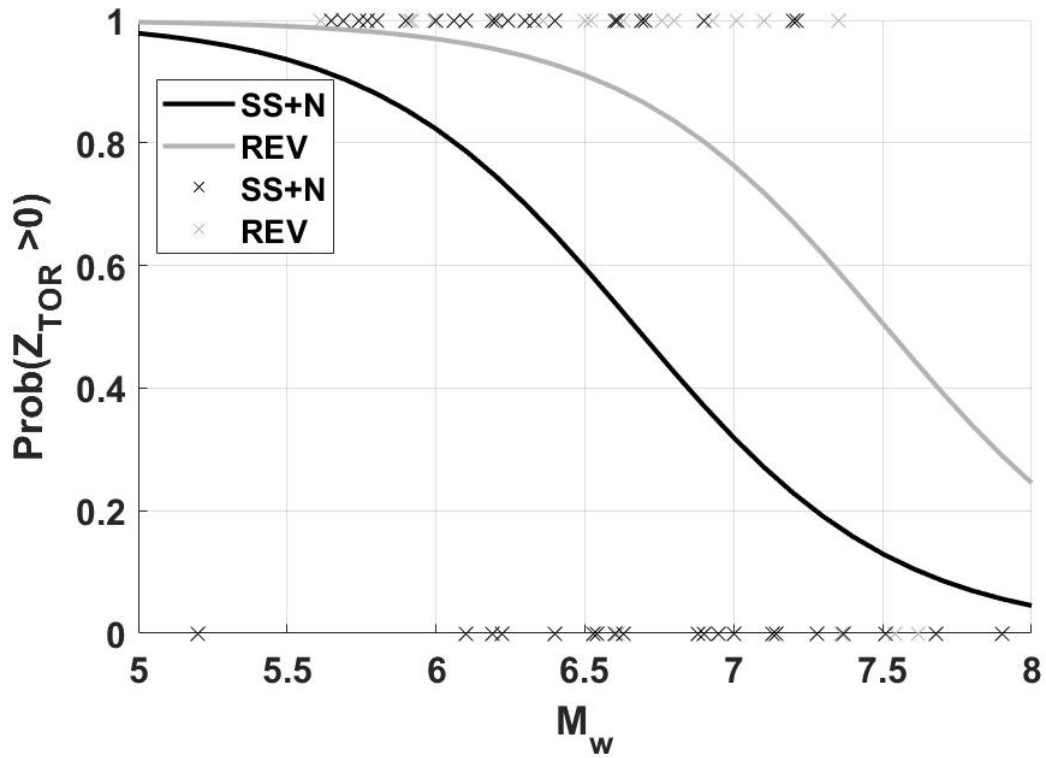


Figure 10. Logistic regression models for $Prob(Z_{TOR} > 0)$ against used data.

To use regression analysis to develop predictive equations for Z_{TOR} when $Z_{TOR} > 0$, and similarly to develop predictive equations for L_R and W_R in the next section, the data is first transformed to ensure normality of the regression residuals. The functional form of the predictive equation of a transformed model parameter Y is initially constructed as:

$$Y = (\beta_0 + \beta_1 F) + (\beta_2 + \beta_3 F)M_w + \epsilon, \quad (4)$$

where ϵ denotes the regression residual, assumed to be a normally distributed random variable with a mean of zero and standard deviation σ , and β_0, \dots, β_3 are the model parameters. Step-wise linear regression is utilized to investigate the importance of the predictors, and the models are refitted accordingly. The models are evaluated based on the resulting adjusted R^2 value, residual plots, plots of fitted versus observed values, and normality of the residuals using the Shapiro-Wilk normality test (Wilk & Shapiro, 1965). Residual plots and plots of fitted versus observed values indicating the R^2 values for all the developed models are provided in Appendix B. A significance level of 5% is used for all statistical tests, unless stated otherwise.

A logarithmic transformation is applied to the $Z_{TOR} > 0$ data to increase the normality of the regression residuals. The following model, having an adjusted R^2 value of 0.34, is obtained:

$$E[\ln Z_{TOR} | Z_{TOR} > 0] = \begin{cases} 9.361 - 1.400M_w & \text{for SS and N} \\ 6.362 - 0.789M_w & \text{for REV} \end{cases}, \quad \sigma_{\ln Z_{TOR}} = 0.86, \quad (5)$$

where Z_{TOR} is in km.

Moreover, to prevent the model from giving unreasonable predictions, upper limits are imposed. The following limits, which are based on the observed maximum values in the used database, are suggested:

$$Z_{TOR} \leq \begin{cases} \exp(E[\ln Z_{TOR}|Z_{TOR} > 0, \text{SS and N}] + 1.75\sigma_{\ln Z_{TOR}}), & \text{for SS and N} \\ 10 \text{ km} \end{cases} \quad (6)$$

$$Z_{TOR} \leq \begin{cases} \exp(E[\ln Z_{TOR}|Z_{TOR} > 0, \text{REV}] + 1.75\sigma_{\ln Z_{TOR}}), & \text{for REV.} \\ 15 \text{ km} \end{cases}$$

Figure 11 shows the predictive model for $Z_{TOR} > 0$ given by Equation 5 and the upper limits given by Equation 6, plotted against the data used for fitting. It can be seen from Figure 10 and Figure 11 that the probability of having a buried rupture decreases with increasing magnitude and is larger for reverse faults than for strike-slip or normal faults. Similarly, Z_{TOR} tends to decrease with magnitude, and reverse faults tend to have larger Z_{TOR} values than strike-slip and normal faults. These observations are consistent with previous Z_{TOR} models, such as the one proposed by Chiou and Youngs (2014). These models should only be used in their ranges of applicability ($5.2 \leq M_w \leq 7.9$) and extrapolation should be exercised with caution, since the model does not account for a plateau in Z_{TOR} observed by Chiou and Youngs (2014) for $M_w < 5$.

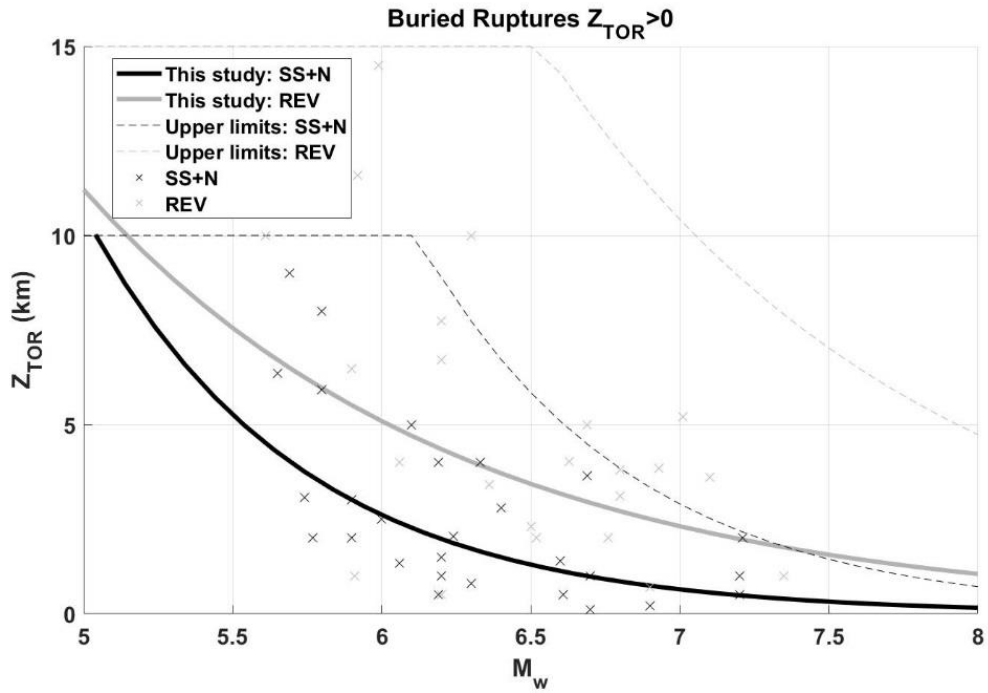


Figure 11. Predictive models for $Z_{TOR} > 0$, with upper limits, against used data.

3. Rupture Dimensions L_R and W_R

As mentioned before, calculating $(R_{RUP}, s_{or}d, \theta_{or}\phi)$ for a given site requires knowledge of the geometry and coordinates of the fault rupture and the location of the hypocenter. The fault rupture geometry is idealized as rectangular, but the rupture aspect ratio varies from earthquake to earthquake. In this section, predictive models are developed for L_R and W_R , while accounting for their variability and for the correlation between them. F and M_w are the predictor variables considered. Possible differences in rupture dimensions between buried ruptures ($Z_{TOR} > 0$) and surface ruptures ($Z_{TOR} = 0$) are also considered. As mentioned earlier, data from normal earthquakes is limited, and suggests similarities with data from both strike-slip and reverse earthquakes. In this study, data from normal faulting is combined with data from reverse faulting to develop the predictive models for the rupture dimensions. This is similar to what has been done in earlier studies (e.g., Schwartz, 2018; Watts & Burov, 2003).

A procedure similar to that used for developing the linear regression model of $Z_{TOR} > 0$ is used. For the rupture length, no statistical difference is observed between surface and buried ruptures, so a predictive model that does not make this distinction is developed. The following model, having an adjusted R^2 value of 0.81, is obtained:

$$E[\ln L_R] = \begin{cases} -5.653 + 1.376M_w & \text{for SS,} \\ -5.881 + 1.376M_w & \text{for REV and N,} \end{cases} \quad \sigma_{\ln L_R} = 0.40, \quad (7)$$

where L_R is in km. Figure 12 shows the fitted predictive model for L_R together with the employed data. The model indicates that L_R increases with M_w , and that SS ruptures tend to be longer than REV and N ruptures. These are consistent with previous findings (Schwartz, 2018). Figure 12 also shows the widely used model for subsurface rupture length developed by Wells and Coppersmith (1994), referred to as WC94. The

comparison shows that, in general, the developed models are similar to the WC94 models and are a good fit to the available data for L_R .

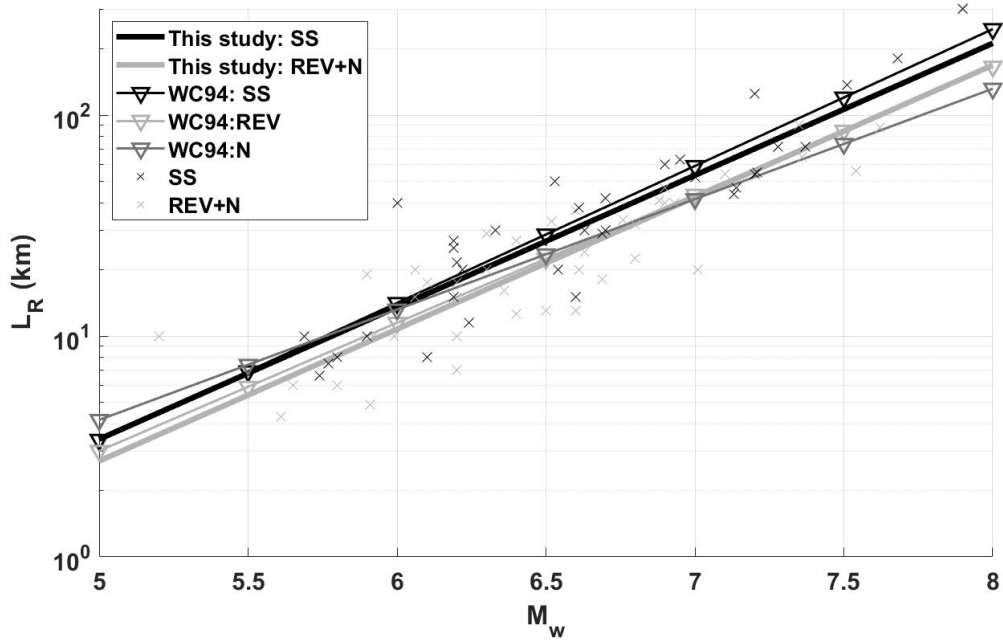


Figure 12. Comparison of developed predictive models for L_R with WC94 and employed data.

For the rupture width, a significant statistical difference is observed between the surface and buried rupture cases. Therefore, two models which distinguish between the two cases are developed. The following models, having adjusted R^2 values of 0.47 and 0.70 respectively, are obtained:

$$E[\ln W_R | Z_{TOR} = 0] = \begin{cases} -0.504 + 0.458M_w & \text{for SS,} \\ -0.105 + 0.458M_w & \text{for REV and N,} \end{cases} \quad \sigma_{\ln W_R} = 0.33, \quad (8)$$

$$E[\ln W_R | Z_{TOR} > 0] = \begin{cases} -3.352 + 0.898M_w & \text{for SS,} \\ -3.149 + 0.898M_w & \text{for REV and N,} \end{cases} \quad \sigma_{\ln W_R} = 0.28 \quad (9)$$

where W_R is in km. Figure 13 shows the fitted predictive models for W_R , together with the data used to fit them. The models indicate that W_R increases with M_w , and that REV and N ruptures tend to be wider than SS ruptures. These trends are consistent with previous findings (Watts & Burov, 2003). The models also indicate that, when the rupture reaches the surface, the rate of change of W_R with M_w decreases, while the rate of change

of L_R with M_w is not affected (see Equations 7-9). This is consistent with the observation of Dalguer, Miyake, Day, and Irikura (2008) that surface ruptures tend to have a larger aspect-ratio than buried ruptures. Figure 13 also shows the WC94 rupture width models, which distinguish between the three faulting mechanisms but not between surface and buried ruptures. The comparison shows that, for the available W_R data, the developed models result in lower mean and standard deviation of the model error than WC94. Note that for the L_R and W_R models, the effect of magnitude is found to be independent from the faulting mechanism (i.e., $\beta_3 = 0$ in Equation 4), and only the intercept is affected by the faulting mechanism (i.e., $\beta_1 \neq 0$).

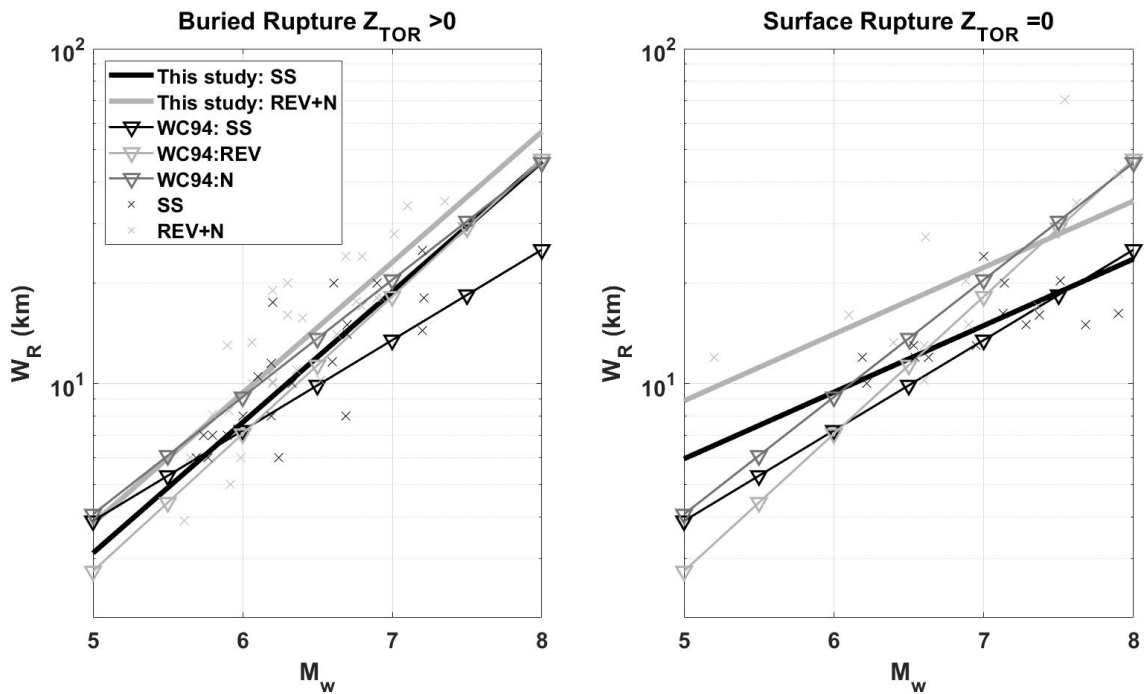


Figure 13. Comparison of developed predictive models for W_R with WC94 and employed data.

Upper bounds on L_R and W_R are imposed based seismological considerations to prevent unrealistic values. If the user specifies the length L_F of the fault, or the coordinates of the end points of the top edge of the fault from which L_F can be calculated, an upper bound $L_{R,max} = L_F$ is imposed on the rupture length. Otherwise $L_{R,max} = 500$ km is imposed, which is the largest observed fault length (Schwartz, 2018). The user can also specify the depth Z_{TOF} of the top edge of the fault and the width W_F of the fault, if this information is available. If not, default values $Z_{TOF} = 0$ and $W_F = \frac{H-Z_{TOF}}{\sin \delta}$ are assumed, where H is the seismogenic depth in km (assumed to be 25 km if no information is available) and δ is the dip of the fault in degrees. If the dip angle is not available, mean values based on faulting mechanism can be used: 85° for SS faulting, 40° for REV faulting, and 53° for N faulting. These mean values are obtained based on fault dip data in the considered database of shallow crustal earthquakes. Then, given the simulated value of Z_{TOR} , the upper bound on the rupture width is calculated as

$$W_{R,max} = W_F - \frac{(Z_{TOR}-Z_{TOF})}{\sin \delta}. \quad (10)$$

Using the developed mean predictive models for $\ln L_R$ and $\ln W_R$, the corresponding mean predictive model for $\ln A_R$ can be calculated as a function of M_w :

$$E[\ln A_R] = \begin{cases} -6.157 + 1.834M_w & \text{for SS surface ruptures,} \\ -5.986 + 1.834M_w & \text{for REV and N surface ruptures,} \\ -9.004 + 2.275M_w & \text{for SS buried ruptures,} \\ -9.031 + 2.275M_w & \text{for REV and N buried ruptures,} \end{cases} \quad (11)$$

where A_R is the rupture area in km^2 . These rupture area-magnitude scaling models are plotted in Figure 14. The relationships for surface and buried ruptures intersect at $M_w = 6.47$ for strike-slip faults and at $M_w = 6.92$ for other faulting mechanisms. This intersection can be thought of as a break in the rupture area-magnitude scaling between smaller magnitude events, more likely to be buried ruptures, and larger magnitude events,

more likely to be surface ruptures. A similar break at $M_w = 6.71$ was observed by Hanks and Bakun (2002) for strike-slip faults, but in the magnitude-rupture area scaling. Furthermore, it can be observed from Figure 14 that for smaller amplitude events (below 6.47 for SS and below 6.92 for REV and N), the area of buried ruptures is smaller than that of surface ruptures. This is consistent with the findings of Kagawa et al. (2004), which indicated that, for the same moment magnitude, the area of buried ruptures is almost 1.5 times smaller than that of surface ruptures.

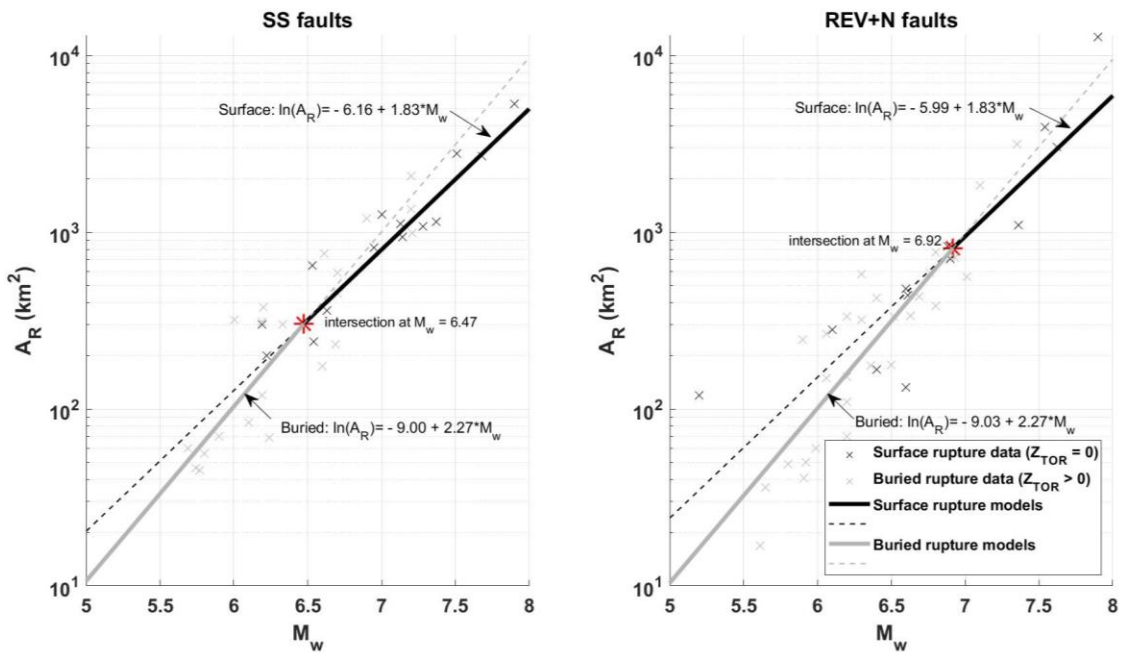


Figure 14. Comparison of resulting $\ln A_R - M_w$ scaling relationships with the corresponding data from buried and surface ruptures. The solid lines represent the relationships for buried and surface ruptures below and above their intersections, respectively. The dashed lines represent the relationships for buried and surface ruptures above and below their intersections, respectively.

Next, correlations between the log-transformed rupture geometry parameters (Z_{TOR}, L_R, W_R) are examined. They are estimated as the correlations between the residuals of the developed models. These correlations are documented in Table 7 along with their 95% confidence intervals (in brackets). A statistically significant correlation (at the 8% significance level) is observed only between $\ln L_R$ and $\ln W_R$ when $Z_{TOR} > 0$. The data

indicates that there is a mild positive correlation (0.248) between rupture length and width only for buried ruptures, while for surface ruptures, length and width seem uncorrelated. Further investigation shows that the correlation between $\ln L_R$ and $\ln W_R$ tends to decrease with magnitude, which explains why buried ruptures (usually associated with smaller magnitude events) show some positive correlation, while surface ruptures (usually associated with larger magnitude events) show close to zero correlation. Moreover, for buried ruptures, Z_{TOR} seems uncorrelated from both L_R and W_R . The correlation structures accounted for when simulating rupture geometry parameters using the developed models are given in Table 8.

Table 7. Estimated correlation matrix of regression residuals of the developed models and their 95% confidence intervals: a) for $Z_{TOR} = 0$; and b) for $Z_{TOR} > 0$. Only the correlation between $\ln L_R$ and $\ln W_R$ when $Z_{TOR} > 0$ is found to be statistically significant (at the 8% significance level).

a) $Z_{TOR} = 0$	$\ln L_R$	$\ln W_R$
$\ln L_R$	1	-0.018 [-0.40, 0.37]
$\ln W_R$	-0.018 [-0.40, 0.37]	1

b) $Z_{TOR} > 0$	$\ln Z_{TOR}$	$\ln L_R$	$\ln W_R$
$\ln Z_{TOR}$	1	-0.029 [-0.30, 0.25]	-0.122 [-0.38, 0.16]
$\ln L_R$	-0.029 [-0.30, 0.25]	1	0.248 [-0.03, 0.49]
$\ln W_R$	-0.122 [-0.38, 0.16]	0.248 [-0.03, 0.49]	1

Table 8. Correlation matrices of regression residuals used in the simulations: a) for $Z_{TOR} = 0$; and b) for $Z_{TOR} > 0$.

a) $Z_{TOR} = 0$	$\ln L_R$	$\ln W_R$
$\ln L_R$	1	0
$\ln W_R$	0	1

b) $Z_{TOR} > 0$	$\ln Z_{TOR}$	$\ln L_R$	$\ln W_R$
$\ln Z_{TOR}$	1	0	0
$\ln L_R$	0	1	0.248
$\ln W_R$	0	0.248	1

4. Location of Rupture Plane within Fault Plane

Given the coordinates of the top points of the fault and its maximum width and dip angle, the rectangular fault plane is defined. Then, for any set of the simulated parameters (L_R, W_R, Z_{TOR}), the location of the L_R by W_R rupture at depth Z_{TOR} within the fault plane is randomized assuming a uniform distribution.

D. Hypocenter Location within Rupture Plane

The location of the hypocenter within the fault rupture plane has an important effect on the ground motion characteristics at a site since it strongly influences the directivity configuration (Somerville et al., 1997). In fact, the location of the hypocenter is a required input for physics-based simulations (e.g., Graves & Pitarka, 2016; Hartzell et al., 2005; Pitarka, Graves, Irikura, Miyake, & Rodgers, 2017) and it is also needed to calculate various directivity parameters proposed by directivity modelers, e.g., $s_{or}d$ and $\theta_{or}\phi$ in this study. Therefore, to properly account for the variability of generated ground motions, the simulation procedure should account for the variability in the hypocenter location. It is noted that in the kinematic ground motion simulations conducted by Graves and Pitarka (2016) and Pitarka et al. (2017), only variations in the slip distribution were considered, while the variabilities in the hypocenter location and fault rupture area were neglected.

Most previous studies assume the location of the hypocenter is uniformly distributed along the fault strike; this is the model also employed in Dabaghi and Der Kiureghian (2014). The down-dip location is assumed to be either deterministic or to also follow a uniform distribution. For example, early studies in the CyberShake project placed hypocenters every 20 km along the strike (a discrete uniform distribution) and at a down-

dip distance of 0.75 of the rupture width (Graves et al., 2011), while more recent studies placed them every 4.5 km along the strike and down-dip (SCEC, 2018). However, Mai et al. (2005) found that data from more than 50 earthquakes does not support the assumption that the location of the hypocenter is uniformly distributed over the rupture plane. They found that the location of the hypocenter is more likely to be near the center of the rupture plane than near the ends. They modeled the location of the hypocenter along the strike as a random variable following a truncated normal distribution with mean $0.5L_R$ and standard deviation $0.23L_R$, while the down-dip location normalized by the rupture width W_R was modeled using a Weibull distribution for both strike-slip and crustal dip-slip earthquakes. The shape and scale parameters of the fitted Weibull distributions for the two types of earthquakes are listed in Table 9. In this study, the along-strike and down-dip locations of the hypocenter within the rupture plane are assumed to be independent random variables and follow the distributions proposed by Mai et al. (2005). These distributions were also used by (Chiou and Youngs, 2008).

Table 9. Shape and scale parameters of Weibull distributions for normalized down-dip hypocenter location fitted by Mai et al. (2005).

Faulting Mechanism	Distribution Function	Scale Parameter	Shape Parameter
SS	Weibull	0.626	3.921
REV+N	Weibull	0.692	3.394

E. Simulation Procedure for Specified Site and Random Hypocenter Location – P1

We first consider the case where F , M_w , the fault geometry (coordinates of the top points, fault dimensions L_F and W_F , depth of the top edge of the fault Z_{TOF} , and dip δ) and the site information (location and V_{s30}) are known, which is procedure P1. As mentioned earlier, if some of the fault geometry parameters are unavailable, the default

values $Z_{TOF} = 0$, $W_F = \frac{H-Z_{TOF}}{\sin \delta}$, and $\delta = 85^\circ$ for SS faulting, 40° for REV faulting, and 53° for N faulting are used. The following procedure is employed to simulate Z_{TOR} , R_{RUP} and the rupture directivity parameters (s_{ord} , $\theta_{or}\phi$):

1. Given M_w and F , the probability p of obtaining $Z_{TOR} > 0$ is calculated from Equation 3. A random number generator is then employed to simulate a value of either 0 (i.e., $Z_{TOR} = 0$) or 1 (i.e., $Z_{TOR} > 0$), with the latter having a probability of occurrence p .
2. If $Z_{TOR} = 0$, i.e., a surface rupture case, $\ln L_R$ and $\ln W_R$ are simulated as normally distributed uncorrelated random variables with means and standard deviations computed from Equations 7 and 8. If $Z_{TOR} > 0$, i.e., a buried rupture case, $\ln Z_{TOR}$, $\ln L_R$ and $\ln W_R$ are simulated as normally distributed correlated random variables with means and standard deviations estimated from Equations 5, 7 and 9, respectively, and correlations based on Table 8(b). If any of the resulting Z_{TOR} , L_R or W_R values are larger than the imposed upper bounds calculated from Equations 6 and 10, step 2 is repeated until all upper bounds are satisfied.
3. Given the geometry of the fault and the simulated rupture parameters (Z_{TOR} , L_R and W_R), the location of the rupture plane is uniformly sampled from within the fault plane. The corresponding coordinates of the edges of the rupture plane are calculated.
4. Given F , L_R and W_R , the location of the hypocenter along the strike and down-dip are independently simulated based on the Mai et al. (2005) distribution models described above. The corresponding hypocenter coordinates are calculated.

5. The simulated coordinates of the rupture plane and hypocenter and the coordinates of the site location are then used to calculate R_{RUP} , $s_{or}d$ and $\theta_{or}\phi$.

Each simulation results in a different set of values of Z_{TOR} , L_R , W_R , and the rupture and hypocenter locations, thus in different values of R_{RUP} , $s_{or}d$ and $\theta_{or}\phi$. This process is repeated to generate any desired number of rupture directivity scenarios for a specific set of input values (F , M_w , fault geometry, site location and V_{s30}). The resulting (F , M_w , Z_{TOR} , R_{RUP} , V_{s30} , $s_{or}d$, $\theta_{or}\phi$) scenarios are then provided as input to the near-fault simulation procedure of Dabaghi and Der Kiureghian (2018) to generate the desired number of synthetic near-fault ground motions.

1. Example Application

The proposed simulation procedure is used to generate pairs of horizontal components of near-fault ground motions for an earthquake event at a site located in downtown Los Angeles (LADT) and selected from the CyberShake platform (SCEC, 2018). The site has latitude 34.05204, longitude -118.25713 and $V_{s30} = 390$ m/s. The 2008 edition of the USGS hazard model is used in the USGS unified hazard tool to determine the earthquakes and faults that contribute most to the hazard at the LADT site. For example, at a spectral period of 2 seconds and for a return period of 2475 years, the deaggregation results show a major contribution from earthquakes having large magnitudes ($M_w > 6.50$) and occurring at short distances (< 10 km) from the site. One of the largest contributors to the hazard is an earthquake with $M_w = 6.55$ on the Upper Elysian Park reverse fault ($F = 1$). This earthquake scenario is used to illustrate our proposed simulation procedure. Information about the geometry of the Upper Elysian Park fault is extracted from the CyberShake platform, which is based on Version 2.0 of

the Uniform California Earthquake Rupture Forecast, UCERF2.0 (Field et al., 2009). The extracted information includes the coordinates of the end points of the top edge of the fault, from which the fault length $L_F = 18.7$ km is calculated as the horizontal distance between the two points, i.e., by idealizing the fault as a rectangular plane. The above reference also provides $W_F = 20.4$ km, $Z_{TOF} = 3.1$ km and $\delta = 50^\circ$.

Given information about the fault type ($F = 1$) and geometry (coordinates of the top points, $L_F = 18.7$ km, $W_F = 20.4$ km, $Z_{TOF} = 3.1$ km and $\delta = 50^\circ$), and the site location and $V_{s30} = 390$ m/s, procedure P1 is used to generate, for $M_w = 6.55$, 100 different realizations of Z_{TOR} , L_R , W_R , rupture location within the fault plane, and hypocenter location, which are in turn used to calculate R_{RUP} , $s_{or}d$ and $\theta_{or}\phi$. Table 10 summarizes the resulting ranges of some of these parameters for this particular example. Moreover, Figure 15 illustrates selected realizations of randomized Z_{TOR} and rupture dimensions, while Figure 16 illustrates selected realizations of randomized hypocenter locations within a fixed rupture plane.

Table 10. Ranges of simulated rupture geometry parameters and calculated distance and directivity parameters.

Simulated parameter	L_R (km)	W_R (km)	Z_{TOR} (km)	R_{RUP} (km)	d (km)	ϕ ($^\circ$)
Min	7.9	5.2	3.1	6.4	1.7	0.4
Max	18.4	20.3	9.3	10.8	17.0	16.8

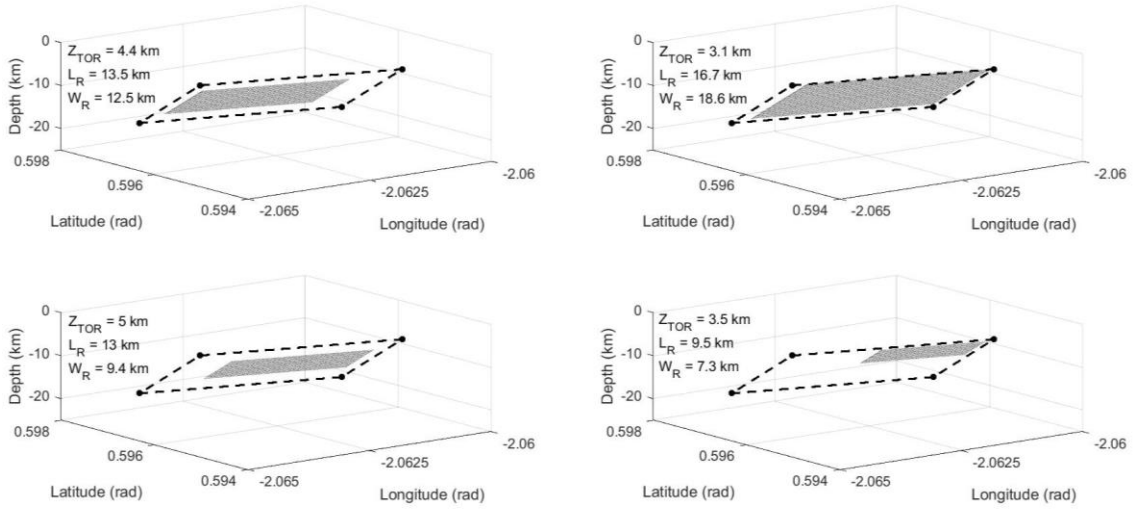


Figure 15. Randomization of Z_{TOR} and the rupture dimensions and location (gray rectangular surface) for an $M_w = 6.55$ earthquake on the Upper Elysian Park fault (dashed black rectangle).

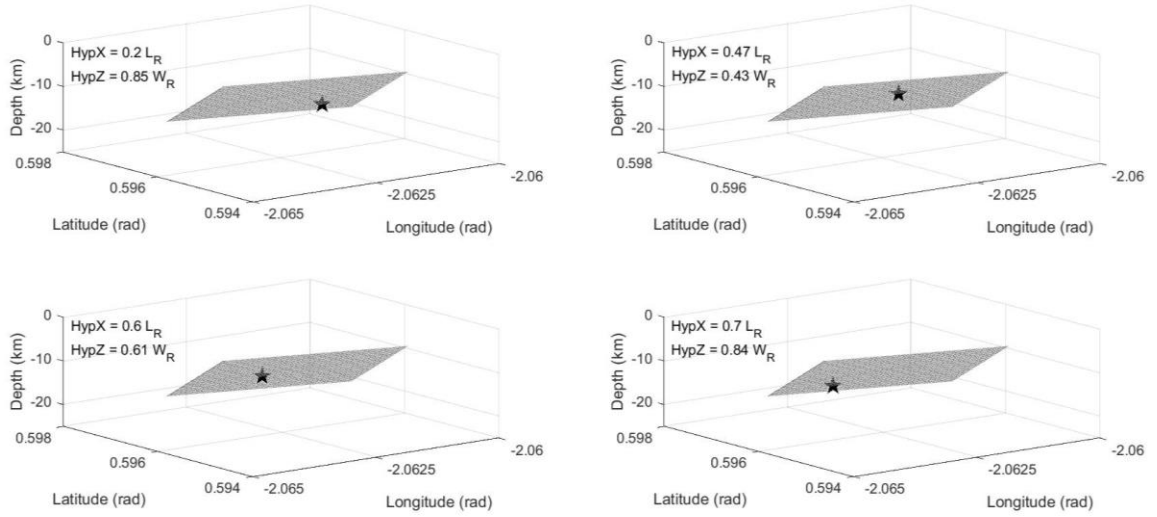


Figure 16. Randomization of the hypocenter location (black star) along strike ($HypX$) and down-dip ($HypZ$) within a fault rupture plane (gray rectangular surface) with fixed rupture geometry of $Z_{TOR} = 3.1$ km, $L_R = 16.7$ km and $W_R = 18.6$ km.

For the 100 different sets of simulated rupture realizations, the corresponding parameters (Z_{TOR} , R_{RUP} , $s_{ord} = d$, and $\theta_{or}\phi = \phi$) are used as input to the simulation procedure of Dabaghi and Der Kiureghian (2018), together with ($F = 1$, $M_w = 6.55$, and $V_{s30} = 390$ m/s), to obtain 100 pairs of horizontal components of near-fault motion. The

5% damped RotD50 pseudo-acceleration response spectra (Boore, 2010) of the simulated motions and their median and median plus and minus one logarithmic standard deviations are illustrated in Figure 17. These simulations, which cover a range of directivity configurations (d between 1.7 and 17.0 km), consist of 38 pulse-like and 62 non-pulse-like motions. The pulse periods T_p range between 0.44 s and 2.44 s. Over this range, the pulse-like motions tend to have larger amplitudes than non-pulse-like motions; see Figure 17. Moreover, Figure 17 highlights one pulse-like simulation with $T_p = 2.12$ s and resulting from a rather forward directivity scenario ($d = 11.2$ km), and one non-pulse-like simulation resulting from a rather backward directivity scenario ($d = 3.8$ km). Note that the spectral amplitudes of the pulse-like motion are amplified near the period of the pulse.

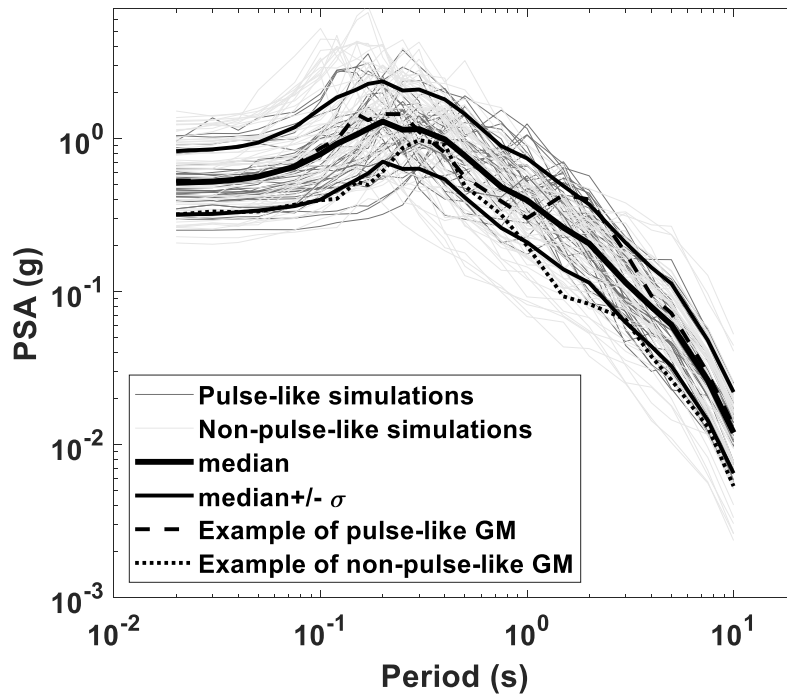


Figure 17. 5% damped RotD50 pseudo-acceleration response spectra of 100 simulated motions (38 pulse-like and 62 non-pulse-like) at the LADT site ($V_{S30} = 390$ m/s) due to an earthquake with $M_w = 6.55$ occurring on the Upper Elysian Park fault, median and median plus and minus one logarithmic standard deviations of the simulations, and examples of one pulse-like motion (from a scenario with $d = 11.2$ km and with $T_p = 2.12$ s) and one non-pulse-like motion (from a scenario with $d = 3.8$ km).

F. Simulation Procedure for Random Site and Random Hypocenter Location – P2

Now consider the case where only F , M_w , R_{RUP} , and Z_{TOR} are known, i.e., procedure P2. The following procedure is developed to simulate possible rupture directivity conditions ($s_{or}d$, $\theta_{or}\phi$):

1. Given M_w , F and Z_{TOR} , $\ln L_R$ and $\ln W_R$ are simulated as normally distributed uncorrelated random variables with means and standard deviations estimated from Equations 7 and 8, respectively, if $Z_{TOR} = 0$, or as correlated random variables with means and standard deviations estimated from Equations 7 and 9, respectively, and correlation coefficient 0.248, if $Z_{TOR} > 0$ (see Table 8(b)). A procedure similar to step 2 in P1 is employed to sample L_R and W_R values within the imposed upper bounds.
2. Given F , Z_{TOR} , L_R and W_R , the hypocenter coordinates are simulated similar to step 3 in P1.
3. Given R_{RUP} , Z_{TOR} , L_R , W_R and δ (if δ is unknown, the mean value based on F is used), a “racetrack” is uniformly generated at a distance R_{RUP} from the simulated fault rupture using the method developed by Brian Chiou (personal communication, 2018). A random number generator is then employed to uniformly sample a single site on the racetrack.
4. The simulated rupture geometry as well as hypocenter and site locations are used to calculate $s_{or}d$ and $\theta_{or}\phi$.

Each simulation results in different L_R , W_R , hypocenter and site location and, thus, in different values of $s_{or}d$ and $\theta_{or}\phi$. This process is repeated to generate any desired number of rupture directivity conditions ($s_{or}d$ and $\theta_{or}\phi$) for a specific (F , M_w , R_{RUP} ,

Z_{TOR} and δ) scenario. This allows comparison of the synthetic motions with the NGA-West2 ground motion prediction equations.

1. Example Application

The proposed P2 simulation procedure is used to generate 600 pairs of horizontal components of near-fault ground motions for different hypothetical earthquake scenarios with varying F , M_w , R_{RUP} , Z_{TOR} and V_{S30} values and random directivity conditions. For each simulation, the rupture length L_R , rupture width W_R , hypocenter location, and site location are generated following the procedure P2 described in the previous section. The resulting directivity parameters are used as input to the simulation procedure of Dabaghi and Der Kiureghian (2018) to obtain 600 pairs of orthogonal horizontal components of the ground motion.

In order to validate the obtained synthetic ground motions, the statistics of their elastic response spectra are compared to those of the NGA-West2 GMPEs (Bozorgnia et al., 2014), and by that indirectly to recorded ground motions. We use a weighted average of the five NGA-West2 GMPEs developed by: (1) Abrahamson, Silva and Kamai (2014), denoted ASK14; (2) Boore, Stewart, Seyhan and Atkinson (2014), BSSA14, (3) Campbell and Bozorgnia (2014), CB14; (4) Chiou and Youngs (2014), CY14; and (5) Idriss (2014), I14. Following the recommendation in Rezaeian et al. (2014), all models are assigned a weight of 2/9 except I14, which is assigned a weight of 1/9. The weighted average of the five NGA-West2 GMPEs is denoted the “NGA-West2 model”.

The above GMPEs have limitations in the near-fault region. First, they do not require directivity parameters as input (except CY14) and, therefore, cannot differentiate between forward and backward directivity sites. They are assumed to represent random

directivity conditions. Moreover, they were calibrated to larger ranges of magnitude and distance than the Dabaghi and Der Kiureghian (2014) model, which is limited to records from large magnitude earthquakes ($M_w > 5.5$) at short distances ($R_{RUP} < 31$ km). Therefore, the GMPEs may be less well calibrated to near-fault scenarios.

The synthetic ground motions are compared with the GMPEs for several hypothetical earthquake scenarios occurring on vertical SS ($F = 0$) or dipping REV faults ($F = 1$), having magnitudes $M_w = 6.5, 7$ or 7.5 , and $Z_{TOR} = 0$ or 3 km. Considered sites have $V_{s30} = 360, 525$ or 760 m/s and are located at $R_{RUP} = 5, 10$ or 20 km from the fault rupture. Simulations were conducted for a total of 28 scenarios.

The NGA-West2 GMPEs require additional input parameters not required by the Dabaghi and Der Kiureghian model. For instance, some GMPEs need as input other distance parameters in addition to or instead of R_{RUP} . These distance parameters include the Joyner-Boore distance R_{jb} (i.e., the closest distance to surface projection of coseismic rupture), the horizontal distance R_x from the top of the rupture measured perpendicular to the fault strike, and the horizontal distance R_{y0} off the end of the rupture measured parallel to the strike. These distance parameters can be calculated for each realization of the rupture geometry and hypocenter and site locations simulated using the procedure P2 for a specified ($F, M_w, R_{RUP}, Z_{TOR}, V_{s30}$) scenario. Mean values of these distance parameters are then used for comparison of each scenario with the GMPEs.

Moreover, the NGA-West2 GMPEs (except I14) differentiate between sites located on the hanging wall (HW), i.e., on the down-dip side of the top of rupture, and sites located on the footwall (FW). The hanging wall effect refers to the increase in ground motion amplitudes at short periods observed at sites located at short distances on the HW side of a rupture, as compared to sites located at the same closest rupture distance but on

the FW side (Donahue & Abrahamson, 2014). This hanging wall effect is accounted for in the the NGA-West2 GMPEs using an input hanging-wall factor, herein referred to as HW ($= 1$ for HW sites; $= 0$ for FW sites). The simulation procedure of Dabaghi and Der Kiureghian does not require HW as input and therefore does not explicitly distinguish between HW and FW sites. Thus, simulated motions are compared with the GMPEs for random HW-FW configurations. Default values are assigned for the other input parameters that remain unspecified in the various GMPEs.

For each of the considered scenarios, statistics of the 5% damped pseudo-acceleration response spectra of the 600 synthetic motions are compared with those described by the NGA-West2 model. The compared statistics are the median and median plus and minus one logarithmic standard deviation levels for the RotD50 horizontal component.

Figure 18 shows the comparison for two of the considered near-fault scenarios, for random HW-FW configurations. In addition to the median and median plus/minus one standard deviation of the synthetic ground motion spectra, we show the median spectra for the subsets of pulse-like and non-pulse-like synthetic motions. The generated synthetic ground motions show good agreement with the GMPEs. At most periods and for both the strike-slip ($F = 0$) and reverse ($F = 1$) faulting mechanisms, the median spectrum of all the simulated motions falls within the range spanned by the median spectra of the five GMPEs. Moreover, the median level from the simulated motions falls within the median plus and minus one standard deviation levels predicted by the NGA-West2 model. For strike-slip faults, the simulations tend to predict larger spectral ordinates at periods between 0.1 and 0.3 seconds and at longer periods (greater than 1 second) and to underestimate spectral ordinates at other periods; see Figure 18 (left). However, the

differences are not large. These observations are mostly consistent among all strike-slip scenarios (refer to Appendix C). For the particular reverse faulting scenario shown in Figure 18 (right), the simulations tend to predict larger spectral ordinates only at longer periods (greater than 1 second) and to underestimate spectral ordinates at all other periods; see. While these differences are larger than the ones observed for the corresponding strike-slip scenario, they are still not significant. Note that other reverse scenarios exhibit slightly different trends, whereby some have more significant differences between the simulated motions and the GMPEs (see, e.g., Figure C.7), while others show better agreement between the two (see, e.g., Figure C.9).

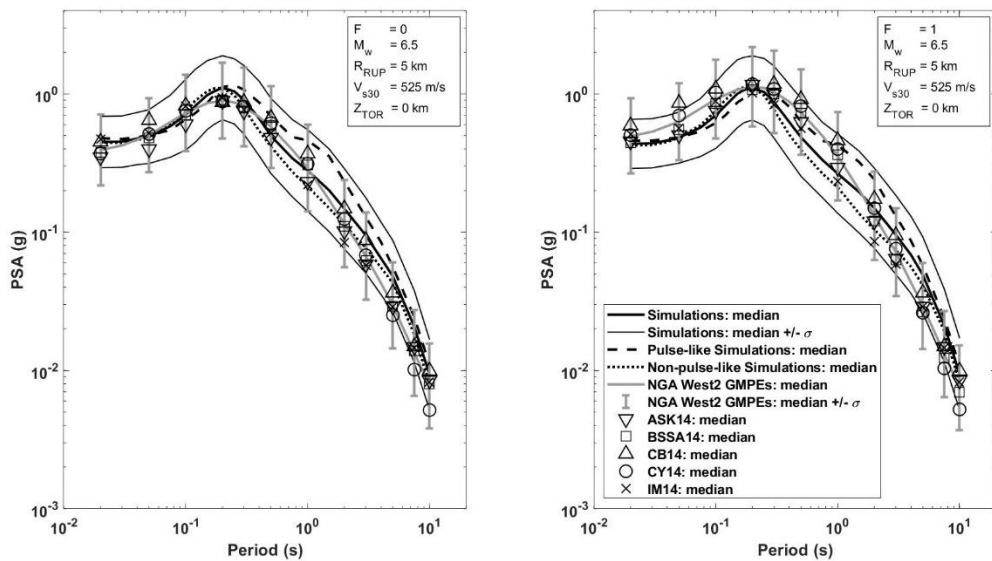


Figure 18. Median and median plus and minus one logarithmic standard deviation of 5% damped pseudo-acceleration response spectra of RotD50 component for 600 synthetic motions, median spectra for pulse-like and non-pulse-like synthetic motions, median and median plus and minus one logarithmic standard deviation spectra predicted by a combination of the five NGA-West2 GMPEs, and median spectra predicted by each of the five NGA-West2 GMPEs for two different earthquake scenarios.

It can be observed from Figure 18 that, for both cases, the median spectrum of the subset of simulated pulse-like motions has considerably larger amplitudes than the median spectrum for all simulated motions as well as the median spectrum of the NGA-West2 model for periods greater than 1 s. This is due to the forward directivity effect, which is

present in the latter spectra in a weighted average sense. On the other hand, the median spectrum of the subset of simulated non-pulse motions has smaller amplitudes than the median spectrum of all simulated motions and smaller values than the median spectrum of the NGA-West2 model at periods 0.5-3 s. This is due to the absence of long-period pulses in these simulated motions. Similar trends are observed for the other scenarios, which are illustrated in Appendix C.

As mentioned earlier, and contrary to the NGA-West2 GMPEs, the simulation procedure of Dabaghi and Der Kiureghian does not explicitly distinguish between HW and FW sites. In fact *HW* is not an input parameter, but information about the simulated rupture geometries and site locations can be used to separate the simulated scenarios and their corresponding synthetic motions into those at HW versus FW sites. Therefore, as next step, we check whether the generated synthetic ground motions are able to capture some differences between HW and FW sites in comparison with the GMPEs.

Figure 19 shows the same statistics as Figure 18 (right), and for the same reverse faulting scenario, but now distinguishing between HW (left panel) and FW (middle panel) sites in both simulated motions and GMPEs. The two scenarios are compared in Figure 19 (right) where it can be observed that, while the amplitudes of the NGA-West2 model are higher at HW sites than at their FW counterparts for all periods less than 3 seconds, the differences between HW and FW simulations are negligible at all periods. Thus, while the simulated motions show good agreement with the GMPEs for random HW-FW configurations (as seen in Figure 18), these simulations do not capture the hanging wall effect as the GMPEs do.

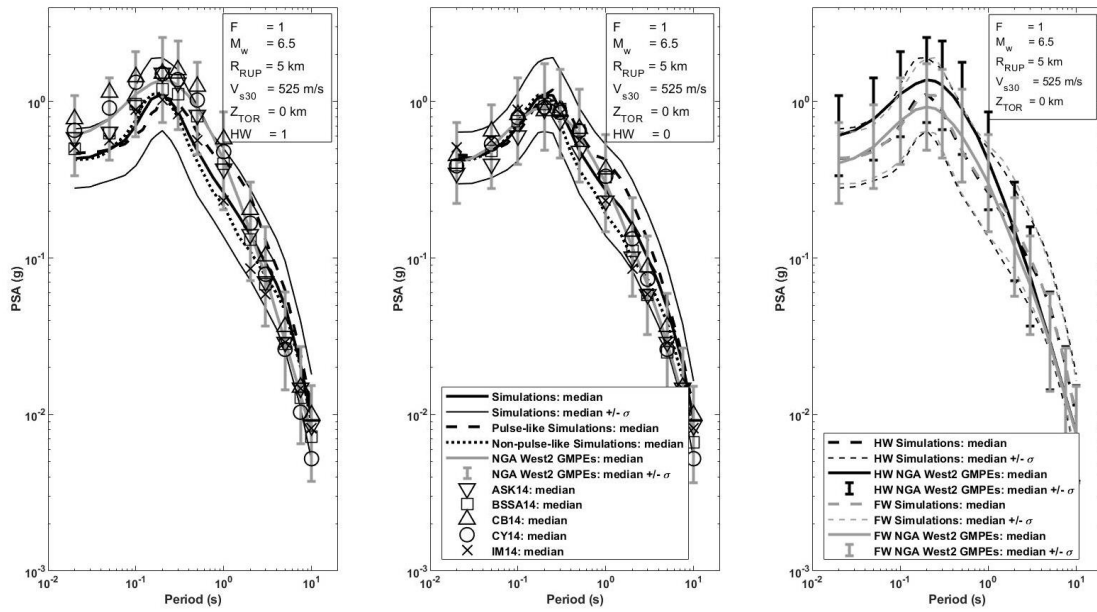


Figure 19. Median and median plus and minus one logarithmic standard deviation of 5% damped pseudo-acceleration response spectra of RotD50 component for 300 synthetic motions, median spectra for pulse-like and non-pulse-like synthetic motions, median and median plus and minus one logarithmic standard deviation spectra predicted by a combination of the five NGA-West2 GMPEs, and median spectra predicted by each of the five NGA-West2 GMPEs for a similar earthquake scenario at HW sites (left) and FW sites (middle). The two scenarios are compared in the right panel.

Figure 19 (left) shows that for HW sites and at shorter periods (below 2 s), the median spectrum of the simulated motions falls below the range spanned by the median spectra of the four NGA-West2 GMPEs that account for the hanging wall effect (i.e., all except I14). Moreover, the median level from the simulated motions falls slightly above but near the median minus one standard deviation level predicted by the NGA-West2 model at most periods below 2 s. On the other hand, Figure 19 (middle) shows that for FW sites and at shorter periods (below 2 s), the median spectrum of the simulated motions falls within the range spanned by the median spectra of all five NGA-West2 GMPEs. Moreover, the median level from the simulated motions falls near the median level predicted by the NGA-West2 model at most periods below 2 s. Therefore, for this

scenario, the simulated motions tend to be more consistent with the GMPEs for the FW scenarios. Similar trends are observed for the other reverse faulting scenarios.

Figures 20, 21, and 22 show the effect on the median spectra of the simulated ground motions and the NGA-West2 model of varying M_w , R_{RUP} and V_{s30} , respectively, while keeping the other scenario parameters constant. It can be observed in Figure 20 that the effect of varying M_w is not captured similarly by the synthetic ground motions and the NGA-West2 model. For the NGA-West2 model, as M_w increases, spectral amplitudes increase at all periods, whereas for the synthetic motions spectral amplitudes increase with M_w at longer periods, while magnitude saturation is observed at lower periods. On the other hand, Figure 21 shows that the spectral amplitudes increase at all periods as R_{RUP} decreases, for both the NGA-West2 model and the synthetic motions. Moreover, for all the scenarios considered in Figure 21, the period-dependent differences between the NGA-West2 model and the synthetic motions are similar to the differences observed in Figure 18. Finally, it can be observed from Figure 22 that the effect of varying V_{s30} is not captured similarly by the NGA-West2 model and the synthetic ground motions. For the NGA-West2 model, as V_{s30} decreases spectral amplitudes increase at all periods, but more at the longer periods. For the synthetic motions, the effect of V_{s30} is negligible at shorter periods and spectral amplitudes increase as V_{s30} decreases only at periods longer than about 0.5 s. The trends that the synthetic motions show with V_{s30} at lower periods are comparable to the ones observed by CB14. Since both the simulated motions and the NGA-West2 model are based on fitting assumed models to data of recorded motions, it is not possible to ascertain as to which of the two produce more accurate trends. Nevertheless, it is noted that the differences between the two models and their trends are relatively small.

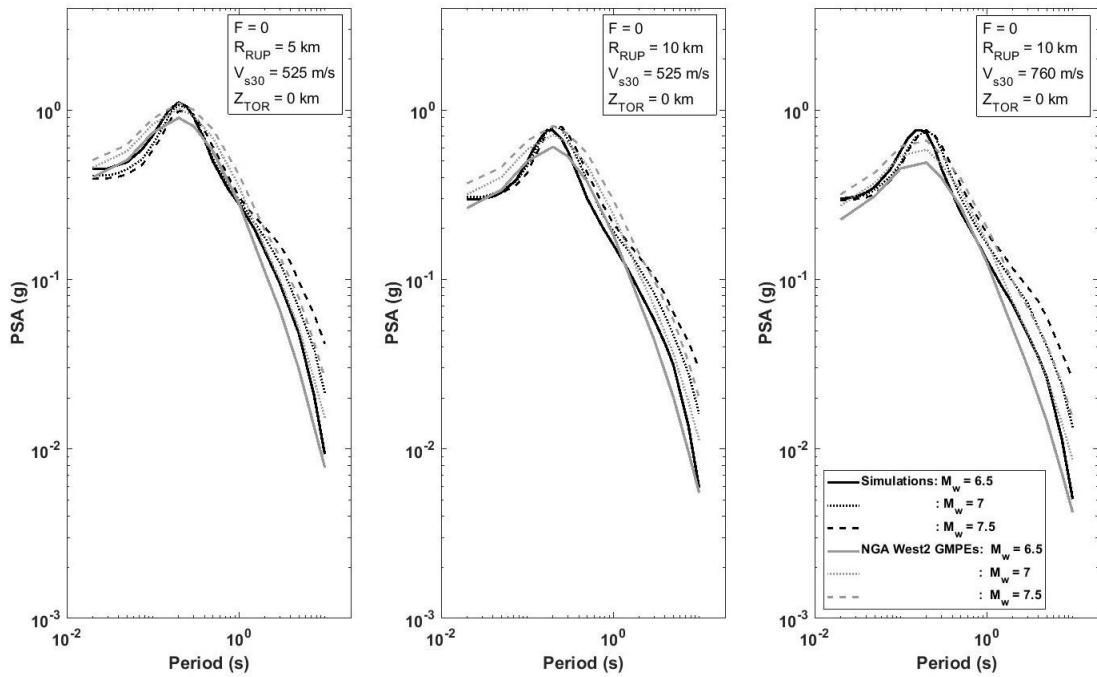


Figure 20. Median of 5% damped pseudo-acceleration response spectra of the RotD50 component for 600 synthetic motions versus median spectra predicted by the NGA-West2 model for scenarios having same F , R_{RUP} , V_{s30} and Z_{TOR} values but different M_w values.

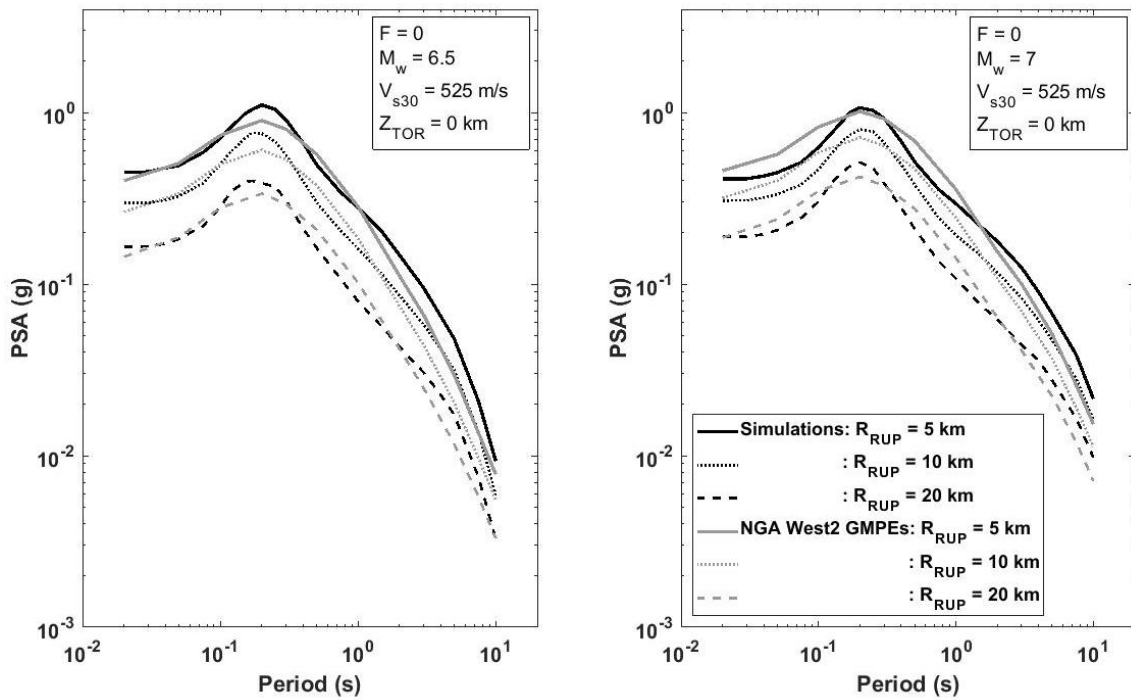


Figure 21. Median of 5% damped pseudo-acceleration response spectra of the RotD50 component for 600 synthetic motions versus median spectra predicted by the NGA-West2 model for scenarios having same F , M_w , V_{s30} and Z_{TOR} values but different R_{RUP} values.

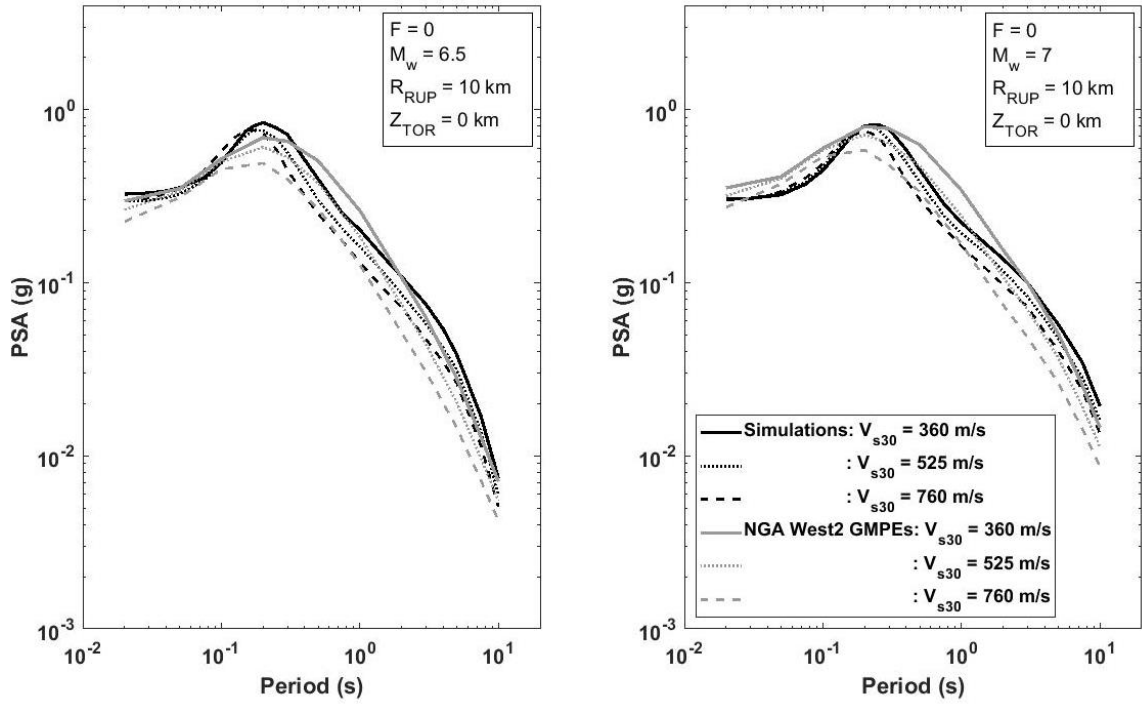


Figure 22. Median of 5% damped pseudo-acceleration response spectra of the RotD50 component for 600 synthetic motions versus median spectra predicted by the NGA-West2 model for scenarios having same F , M_w , R_{RUP} and Z_{TOR} values but different V_{S30} values.

G. Conclusions

Novel procedures to simulate suites of synthetic near-fault ground motions for randomized source and site characteristics are proposed. The site-based stochastic model and simulation procedure proposed by Dabaghi and Der Kiureghian (2014, 2017, 2018) requires information about the source, site, and source-to-site geometry, namely $(F, M_w, Z_{TOR}, R_{RUP}, V_{S30}, s_{or}d, \theta_{or}\phi)$. The resulting simulations account for the near-fault rupture directivity effect and capture the natural variability of real ground motions. They also make the crucial distinction between pulse-like and non-pulse-like ground motions. However, the directivity parameters $s_{or}d$ and $\theta_{or}\phi$ entail often unavailable knowledge of the rupture geometry and hypocenter location.

Using data from a subset of earthquakes in the NGA West2 database, new predictive models are developed for the rupture geometry parameters (Z_{TOR} , L_R , and W_R) as a function of F and M_w . These models are found to be consistent with existing models. For simplicity, the fault rupture is idealized as a rectangular plane. Important features of the developed models include: (1) account for the variability and correlations between the rupture geometry parameters; (2) a two-part model consisting of a logistic regression model and a linear regression model to account for the zero-inflation in Z_{TOR} values; and (3) models for L_R and W_R that distinguish between buried ruptures ($Z_{TOR} > 0$) and surface ruptures ($Z_{TOR} = 0$). Several observations can be made about the scaling of rupture geometry with magnitude. For example, the models indicate that the scaling of the rupture width with magnitude is different for buried and surface ruptures, while the scaling of the rupture length with magnitude is not affected by Z_{TOR} . As more data becomes available, the models can be improved.

The first extension (P1) to the Dabaghi and Der Kiureghian simulation procedure considers the case where only the contributing fault, earthquake magnitude, and site location and properties are known. Using Monte Carlo simulation, random rupture geometries and hypocenter locations are generated according to their probability distributions, and are used to calculate the corresponding randomized rupture directivity conditions. The location of the rupture within the fault plane is assumed to follow a uniform distribution, while the hypocenter location is assumed to follow the distributions proposed by Mai et al. (2005). The procedure is illustrated by simulating near-fault ground motions at a site located in downtown Los Angeles.

The second extension (P2) to the Dabaghi and Der Kiureghian simulation procedure takes as input the type-of-faulting, the earthquake magnitude, the source-to-

site distance, and the site properties. In this case, the rupture geometry as well as both the hypocenter and the site location are randomized. This procedure allows comparison with existing GMPE models. The procedure is illustrated for several earthquake scenarios defined by the set of parameters $(F, M_w, Z_{TOR}, R_{RUP}, V_{s30})$ and the statistics of the synthetic motions are compared with the NGA-West2 models. Results show general agreement between the two, but also some differences. For instance, synthetic ground motions are generally consistent with the GMPEs for random HW-FW configurations, but they are not able to capture the hanging wall effect as the GMPEs do. Both approaches fit assumed models to statistical data, therefore it is not possible to state which model is correct when significant differences appear.

The proposed rupture geometry predictive models and simulation procedures P1 and P2 are necessary for structural engineers who want to generate synthetic motions using a site-based stochastic model in order to perform seismic design or assessment studies at a near-fault site with known location and V_{s30} . They only need information about the magnitude (M_w) and source faults of the earthquakes that contribute most to the hazard at their site of interest. This information can be obtained from deaggregation of probabilistic seismic hazard analysis results. Note that, using the predictive models of the rupture geometry developed herein, the procedure to simulate $(Z_{TOR}, R_{RUP}, s_{ord}, \text{ and } \theta_{or}\phi)$ can easily be extended to simulate any other source-to-site geometry parameters (e.g., other distance measures or directivity parameters) that may be required as input to other site-based stochastic ground motion models or to GMPEs.

CHAPTER IV

SUMMARY, CONCLUSIONS AND FUTURE WORK

A. Summary of the Study

The research presented in this study concerns the stochastic modeling and simulation of ground motion time-series for both far-field and near-fault ground motions. This study addresses a crucial need in performance-based earthquake engineering (PBEE), namely the first step of characterizing the seismic hazard at a location of interest. This first step influences the ensuing steps of computing structural responses for the given hazard, defining and computing relevant measures of damage to structural and non-structural components and equipment, and computing decision variables. Therefore, careful characterization of ground motions is essential. A previous study by Rezaeian and Der Kiureghian (2008, 2010a, 2010b, 2012) proposed a parameterized stochastic model of far-field ground motion that can be used to generate horizontal orthogonal pairs of synthetic ground motion time series for given earthquake source and site characteristics. The model was validated in terms of statistics of simulated elastic response spectra against both recorded motions and empirical models. However, the present study showed that it produces synthetic far-field ground motions exhibiting correlations between spectral periods that are higher than those of the recorded motions and higher than the empirical model of Baker and Jayaram (2008). Additionally, a previous study by Dabaghi and Der Kiureghian (2014, 2017, 2018) resulted in the development of a near-fault ground motion stochastic model and simulation procedure for specified earthquake source and site characteristics. The simulation procedure requires as input information about the source, the site, and the source-to-site geometry, namely, F , M_w , R_{RUP} , and V_{s30} , in addition to

the depth to the top of the rupture plane Z_{TOR} , and the directivity parameters $s_{or}d$ and $\theta_{or}\phi$.

The main objective of this study is to validate and propose improvements to the previous studies by: (1) studying the effect of the higher correlations exhibited by the Rezaeian and Der Kiureghian model on structural response and exploring variations of this model to reduce the correlations between the spectral periods and thus improve structural variability and structural risk estimates; and (2) extending the Dabaghi and Der Kiureghian model to allow users to simulate near-fault ground motions even when the input parameters Z_{TOR} , R_{RUP} , $s_{or}d$, and/or $\theta_{or}\phi$ are unknown.

In order to achieve these objectives, we proceeded as follows: (1) performed response history analysis on an MDOF structural model subjected to various input ground motions and concluded that higher correlations could result in lower estimates of structural risk; and (2) developed rupture geometry predictive models and used them to develop two procedures (P1 and P2) to simulate the input parameters Z_{TOR} , R_{RUP} , $s_{or}d$, and $\theta_{or}\phi$ thereby allowing to simulate suites of synthetic near-fault ground motions for randomized source and site characteristics.

B. Major Contributions and Conclusions

The major contributions and conclusions of this study are summarized as follows:

1. Results of the study that compared the response of a structural model to three different catalogs of recorded and simulated ground motions show that higher correlations between spectral accelerations (combined with lower standard deviations of elastic response spectra) significantly reduce variability of structural response. Therefore, properly accounting for correlations between

spectral accelerations at different periods is in fact essential in ground motion simulation.

2. New predictive models were developed for the rupture geometry parameters (Z_{TOR} , L_R , and W_R) as a function of F and M_w . Important features of the developed models include: (1) account for the variability and correlations between the rupture geometry parameters; (2) a two-part model to account for the zero-inflation in Z_{TOR} values; and (3) models for L_R and W_R that distinguish between buried ruptures ($Z_{TOR} > 0$) and surface ruptures ($Z_{TOR} = 0$).
3. The above models indicate that the scaling of the rupture width with magnitude is different for buried and surface ruptures, while the scaling of the rupture length with magnitude is not affected by Z_{TOR} .
4. The first extension (P1) to the Dabaghi and Der Kiureghian simulation procedure is necessary for structural engineers who want to generate synthetic motions to perform seismic design or assessment studies at a near-fault site with known location and V_{s30} . They only need information about the magnitude (M_w) and source faults of the earthquakes that contribute most to the hazard at their site of interest. This information can be obtained from deaggregation of probabilistic seismic hazard analysis results.
5. The second extension (P2) to the Dabaghi and Der Kiureghian simulation allows comparison with existing GMPE models. The results obtained show general agreement between the two, but also some differences. For instance, synthetic ground motions are generally consistent with the GMPEs for random

HW-FW configurations, but they are not able to capture the hanging wall effect as the GMPEs do.

C. Limitations and Recommendations for Future Studies

Several studies are recommended to improve and expand on the various constituents presented in this study:

1. For the particular example used in the study on spectral correlations and validation of ground motion simulation procedures, in addition to differences in spectral correlations, the three considered ground motion catalogs present differences in the standard deviation of their elastic response spectra at the modal periods of the structure, which could also affect structural variability. Therefore, a limitation of this study is that it is unable to separate the two effects. Additionally, for the example used, the first two modal periods are closely-spaced which results in lower differences in correlations between the first two modes. Therefore, to provide more conclusive results on the sole effect of higher spectral correlations on structural variability, future work should: (1) analyze a structure where differences in the standard deviation of the elastic response spectra at the modal periods are eliminated; and (2) analyze a structure exhibiting higher mode effects but having modal periods that are not closely spaced.
2. This study shows that the model of Broccardo and Dabaghi (2017) results in an improved estimation of the correlations between spectral acceleration values at different periods compared to the model of Rezaeian and Der Kiureghian (2010a). Further studies should be performed to identify the

feature(s) of the stochastic model that result(s) in this improved estimate and possibly incorporate these features in the Rezaeian and Der Kiureghian model.

3. In the proposed simulation procedures P1 and P2, the fault rupture was idealized as a rectangular plane for simplicity. This may result in errors in the prediction of the rupture geometry and of the source-to-site geometry parameters for segmented fault ruptures. For such cases, more complex definitions of the rupture geometry and source-to-site geometry parameters are required.
4. When more earthquakes with finite-fault models become available, updated and more reliable rupture geometry predictive models can be developed.
5. The current version of the simulation procedure was proved in this study to be incapable of differentiating between HW and FW sites. Therefore, future studies should be performed on the Dabaghi and Der Kiureghian model to incorporate the hanging wall effect.

REFERENCES

- Aagaard, B. T., Brocher, T. M., Dolenc, D., Dreger, D., Graves, R. W., Harmsen, S., & Nilsson, S. (2008). Ground-motion modeling of the 1906 San Francisco earthquake, part II: Ground-motion estimates for the 1906 earthquake and scenario events. *Bulletin of the Seismological Society of America*, 98(2), 1012-1046.
- Abrahamson, N.A., Atkinson, G., Boore, D., Bozorgnia, Y., Campbell, K., Chiou, B., & Youngs, R. (2008). Comparisons of the NGA ground-motion relations. *Earthquake Spectra*, 24(1), 45-66.
- Abrahamson, N. A., Silva, W. J., & Kamai, R. (2014). Summary of the ASK14 ground motion relation for active crustal regions. *Earthquake Spectra*, 30(3), 1025-1055.
- Ancheta, T. D., Darragh, R. B., Stewart, J. P., Seyhan, E., Silva, W. J., Chiou, B.S.J., & Boore, D. M. (2014). NGA-West2 database. *Earthquake Spectra*, 30(3), 989-1005.
- Baker, J. W. (2007). *Correlation of ground motion intensity parameters used for predicting structural and geotechnical response*. Paper presented at the Tenth International Conference on Application of Statistics and Probability in Civil Engineering.
- Baker, J. W., & Cornell, C. A. (2006). Correlation of response spectral values for multicomponent ground motions. *Bulletin of the Seismological Society of America*, 96(1), 215-227.
- Baker, J. W., & Jayaram, N. (2008). Correlation of Spectral Acceleration Values from NGA Ground Motion Models. *Earthquake Spectra*, 24(1), 299-317. doi:10.1193/1.2857544
- Bayless, J., & Abrahamson, N. (2018). *Implications of the inter-period correlation of strong ground motions on structural risk*. Paper presented at the Eleventh U.S. National Conference on Earthquake Engineering, Los Angeles, California.
- Boore, D., Stewart, J., Seyhan, E., & Atkinson, G. (2014). Summary of the BSSA14 GMPE. *Earthquake Spectra*, 30.
- Boore, D. M. (1983). Stochastic simulation of high-frequency ground motions based on seismological models of the radiated spectra. *Bulletin of the Seismological Society of America*, 73(6A), 1865-1894.
- Boore, D. M. (2010). Orientation-Independent, Nongeometric-Mean Measures of Seismic Intensity from Two Horizontal Components of Motion. *Bulletin of the Seismological Society of America*, 100(4), 1830-1835. doi:10.1785/0120090400
- Bozorgnia, Y., Abrahamson, N. A., Atik, L. A., Ancheta, T. D., Atkinson, G. M., Baker, J. W., Youngs, R. (2014). NGA-West2 Research Project. *Earthquake Spectra*, 30(3), 973-987. doi:doi:10.1193/072113EQS209M

- Broccardo, M., & Dabaghi, M. (2017). *A spectral-based stochastic ground motion model with a non-parametric time-modulating function*. Paper presented at the 12th International Conference on Structural Safety and Reliability; Vienna.
- Burks, L. S., & Baker, J. W. (2014). Validation of Ground-Motion Simulations through Simple Proxies for the Response of Engineered Systems. *Bulletin of the Seismological Society of America*, 104(4), 1930-1946. doi:10.1785/0120130276
- Campbell, K., Abrahamson, N., Power, M., Chiou, B. S. J., Bozorgnia, Y., Shantz, T., & Roblee, C. (2009). *Next generation attenuation (nga) project: Empirical ground motion prediction equations for active tectonic regions*. Paper presented at the Sixth International Conference on Urban Earthquake Engineering, Tokyo, Japan.
- Campbell, K., & Bozorgnia, Y. (2014). NGA-West2 ground motion model for the average horizontal components of PGA, PGV, and 5% damped linear acceleration response spectra. *Earthquake Spectra*, 30(3), 1087-1115.
- Chiou, B. S.J., & Youngs, R. R. (2008). *NGA Model for Average Horizontal Component of Peak Ground Motion and Response Spectra* (PEER Report No. 2008/09). Retrieved from University of California, Berkeley, CA:
- Chiou, B. S.J., & Youngs, R. R. (2014). Update of the Chiou and Youngs NGA model for the average horizontal component of peak ground motion and response spectra. *Earthquake Spectra*, 30(3), 1117-1153.
- Chopra, A. K. (2017). Dynamics of Structures. Theory and Applications to. *Earthquake Engineering*.
- Dabaghi, M., & Der Kiureghian, A. (2014). *Stochastic modeling and simulation of near-fault ground motions for performance-based earthquake engineering* (PEER Report No. 2014/20). Retrieved from University of California, Berkeley, CA:
- Dabaghi, M., & Der Kiureghian, A. (2017). Stochastic model for simulation of near-fault ground motions. *Earthquake Engineering & Structural Dynamics*, 46(6), 963-984. doi:10.1002/eqe.2839
- Dabaghi, M., & Der Kiureghian, A. (2018). Simulation of orthogonal horizontal components of near-fault ground motion for specified earthquake source and site characteristics. *Earthquake Engineering & Structural Dynamics*, 47, 1369–1393.
- Dalguer, L. A., Miyake, H., Day, S. M., & Irikura, K. (2008). Surface Rupturing and Buried Dynamic-Rupture Models Calibrated with Statistical Observations of Past Earthquakes. *Bulletin of the Seismological Society of America*, 98(3), 1147-1161. doi:10.1785/0120070134
- Donahue, J. L., & Abrahamson, N. A. (2014). Simulation-Based Hanging Wall Effects. *Earthquake Spectra*, 30(3), 1269-1284. doi:10.1193/071113eqs200m

- Douglas, J., & Aochi, H. (2008). A Survey of Techniques for Predicting Earthquake Ground Motions for Engineering Purposes. *Surveys in geophysics*, 29(3), 187-220. doi:<http://dx.doi.org/10.1007/s10712-008-9046-y>
- Dreger, D., Hurtado, G., Chopra, A., & Larsen, S. (2011). Near-field across-fault seismic ground motions. *Bulletin of the Seismological Society of America*, 101(1), 202-221. doi:10.1785/0120090271
- Ellsworth, W. L. (2003). Magnitude and area data for strike slip earthquakes. *US Geol. Surv. Open File Rep*, 03-214.
- Field, E. H., Dawson, T. E., Felzer, K. R., Frankel, A. D., Gupta, V., Jordan, T. H., . . . Weldon, R. (2009). Uniform California earthquake rupture forecast, version 2 (UCERF 2). *Bulletin of the Seismological Society of America*, 99(4), 2053-2107.
- Frankel, A. (2009). A constant stress-drop model for producing broadband synthetic seismograms: Comparison with the Next Generation Attenuation relations. *Bulletin of the Seismological Society of America*, 99(2A), 664-680.
- Graves, R.W., & Pitarka, A. (2016). Kinematic ground-motion simulations on rough faults including effects of 3D stochastic velocity perturbations. *Bulletin of the Seismological Society of America*, 106(5), 2136-2153.
- Graves, R.W., Jordan, T. H., Callaghan, S., Deelman, E., Field, E., Juve, G., & Milner, K. (2011). CyberShake: A physics-based seismic hazard model for southern California. *Pure and Applied Geophysics*, 168(3-4), 367-381.
- Graves, R. W., & Pitarka, A. (2010). Broadband ground-motion simulation using a hybrid approach. *Bulletin of the Seismological Society of America*, 100(5A), 2095-2123. doi:10.1785/0120100057
- Gregor, N., Abrahamson, N.A., Atkinson, G., M. Boore, D., Bozorgnia, Y., Campbell, K., & Youngs, R. (2014). *Comparison of NGA-West2 GMPEs* (Vol. 30).
- Gupta, I. (2006). *Defining source-to-site distances for evaluation of design earthquake ground motion*. Paper presented at the Proceedings of the 13th Symposium on Earthquake Engineering, Roorkee.
- Hanks, T. C., & Bakun, W. H. (2002). A bilinear source-scaling model for M-log A observations of continental earthquakes. *Bulletin of the Seismological Society of America*, 92(5), 1841-1846.
- Hartzell, S., Guatteri, M., Mai, P. M., Liu, P.-C., & Fisk, M. (2005). Calculation of Broadband Time Histories of Ground Motion, Part II: Kinematic and Dynamic Modeling Using Theoretical Green's Functions and Comparison with the 1994 Northridge Earthquake. *Bulletin of the Seismological Society of America*, 95(2), 614-645. doi:10.1785/0120040136

- Idriss, I. (2014). An NGA-West2 empirical model for estimating the horizontal spectral values generated by shallow crustal earthquakes. *Earthquake Spectra*, 30(3), 1155-1177.
- Inoue, T., & Cornell, C. A. (1990). Seismic hazard analysis of multi-degree-of-freedom structures. *Reliability of marine structures*.
- Ishida, H. (1993). Probabilistic evaluation of earthquake response spectrum and its application to response analysis. *Proceedings of ICOSSAR'93*, 3, 2131-2138.
- Jayaram, N., & Shome, N. (2012). *A statistical analysis of the response of tall buildings to recorded and simulated ground motions*. Paper presented at the 15th World Conference on Earthquake Engineering.
- Kagawa, T., Irikura, K., & Somerville, P. G. (2004). Differences in ground motion and fault rupture process between the surface and buried rupture earthquakes. *Earth, Planets and Space*, 56(1), 3-14. doi:10.1186/bf03352486
- Kaklamanos, J., Baise, L. G., & Boore, D. M. (2011). Estimating unknown input parameters when implementing the NGA ground-motion prediction equations in engineering practice. *EARTHQUAKE SPECTRA*, 27(4), 1219-1235.
- Leonard, M. (2010). Earthquake Fault Scaling: Self-Consistent Relating of Rupture Length, Width, Average Displacement, and Moment Release. *Bulletin of the Seismological Society of America*, 100(5A), 1971-1988. doi:10.1785/0120090189
- Luco, N., & Bazzurro, P. (2007). Does amplitude scaling of ground motion records result in biased nonlinear structural drift responses? *Earthquake Engineering & Structural Dynamics*, 36(13), 1813-1835. doi:10.1002/eqe.695
- Mai, P. M., Spudich, P., & Boatwright, J. (2005). Hypocenter Locations in Finite-Source Rupture Models. *Bulletin of the Seismological Society of America*, 95(3), 965-980. doi:10.1785/0120040111
- Olsen, K., Madariaga, R., & Archuleta, R. J. (1997). Three-dimensional dynamic simulation of the 1992 Landers earthquake. *Science*, 278(5339), 834-838.
- Pacific Earthquake Engineering Research Center (PEER). (2013). NGA-West2 Database. <https://peer.berkeley.edu/research/nga-west-2/final-products>
- Pitarka, A., Graves, R., Irikura, K., Miyake, H., & Rodgers, A. (2017). Performance of Irikura Recipe Rupture Model Generator in Earthquake Ground Motion Simulations with Graves and Pitarka Hybrid Approach. *Pure and Applied Geophysics*, 174(9), 3537-3555. doi:10.1007/s00024-017-1504-3
- R Core Team. (2017). R: A Language and Environment for Statistical Computing. Vienna, Austria. Retrieved from <https://www.R-project.org>

- Rezaeian, S., & Der Kiureghian, A. (2010). Simulation of synthetic ground motions for specified earthquake and site characteristics. *Earthquake Engineering & Structural Dynamics*, 39(10), 1155-1180. doi:10.1002/eqe.997
- Rezaeian, S., & Der Kiureghian, A. (2008). A stochastic ground motion model with separable temporal and spectral nonstationarities. *Earthquake Engineering & Structural Dynamics*, 37(13), 1565-1584.
- Rezaeian, S., & Der Kiureghian, A. (2010a). Simulation of synthetic ground motions for specified earthquake and site characteristics. *Earthquake Engineering & Structural Dynamics*, 39(10), 1155-1180. doi:10.1002/eqe.997
- Rezaeian, S., & Der Kiureghian, A. (2010b). *Stochastic Modeling and Simulation of Ground Motions for Performance-Based Earthquake Engineering* (PEER Report No. 2010/02). Retrieved from University of California, Berkeley, CA:
- Rezaeian, S., & Der Kiureghian, A. (2012). Simulation of orthogonal horizontal ground motion components for specified earthquake and site characteristics. *Earthquake Engineering & Structural Dynamics*, 41(2), 335-353. doi:10.1002/eqe.1132
- Rezaeian, S., Petersen, M. D., Moschetti, M. P., Powers, P., Harmsen, S. C., & Frankel, A. D. (2014). Implementation of NGA-West2 ground motion models in the 2014 US National Seismic Hazard Maps. *Earthquake Spectra*, 30(3), 1319-1333.
- Schwartz, D. P. (2018). Review: Past and Future Fault Rupture Lengths in Seismic Source Characterization—The Long and Short of It. *Bulletin of the Seismological Society of America*, 108(5A), 2493-2520. doi:10.1785/0120160110
- Shahi, S. K., & Baker, J. W. (2014). An Efficient Algorithm to Identify Strong-Velocity Pulses in Multicomponent Ground Motions. *Bulletin of the Seismological Society of America*, 104(5), 2456-2466.
- Shaw, B. E. (2009). Constant stress drop from small to great earthquakes in magnitude-area scaling. *Bulletin of the Seismological Society of America*, 99(2A), 871-875.
- Somerville, P. G., Smith, N. F., Graves, R. W., & Abrahamson, N. A. (1997). Modification of Empirical Strong Ground Motion Attenuation Relations to Include the Amplitude and Duration Effects of Rupture Directivity. *Seismological Research Letters*, 68(1), 199-222. doi:10.1785/gssrl.68.1.199
- Southern California Earthquake Center (SCEC). (2018). CyberShake. Retrieved from <https://scec.usc.edu/scecpedia/CyberShake>
- Spudich, P., Bayless, J. R., Baker, J. W., Chiou, B. S.-J., Rowshandel, B., Shahi, S. K., & Somerville, P. G. (2013). *Final report of the NGA-West2 directivity working group* (PEER Report No. 2013/09). Retrieved from University of California, Berkeley, CA:

- Spudich, P., & Chiou, B. S.-J. (2013). *The Spudich and Chiou NGA-West2 directivity model* (PEER Report No. 2013/09). Retrieved from University of California, Berkeley, CA:
- Spudich, P., Rowshandel, B., Shahi, S. K., Baker, J. W., & Chiou, B. S. J. (2014). Comparison of NGA-West2 directivity models. *Earthquake Spectra*, 30(3), 1199-1221. doi:10.1193/080313EQS222M
- U. S. Geological Survey (USGS). (2019). Unified Hazard Tool (Dynamic Conterminous US 2008 Edition). Retrieved from <https://earthquake.usgs.gov/hazards/interactive/index.php>
- Vlachos, C., Papakonstantinou, K. G., & Deodatis, G. (2017). Predictive model for site specific simulation of ground motions based on earthquake scenarios. *Earthquake Engineering & Structural Dynamics*. doi:10.1002/eqe.2948
- Watts, A., & Burov, E. (2003). Lithospheric strength and its relationship to the elastic and seismogenic layer thickness. *Earth and Planetary Science Letters*, 213(1-2), 113-131.
- Wells, D. L., & Coppersmith, K. J. (1994). New empirical relationships among magnitude, rupture length, rupture width, rupture area, and surface displacement. *Bulletin of the Seismological Society of America*, 84(4), 974-1002.
- Wilk, M. B., & Shapiro, S. S. (1965). An analysis of variance test for normality (complete samples)†. *Biometrika*, 52(3-4), 591-611. doi:10.1093/biomet/52.3-4.591

APPENDIX A

ILLUSTRATION OF SIMULATION PROCEDURES

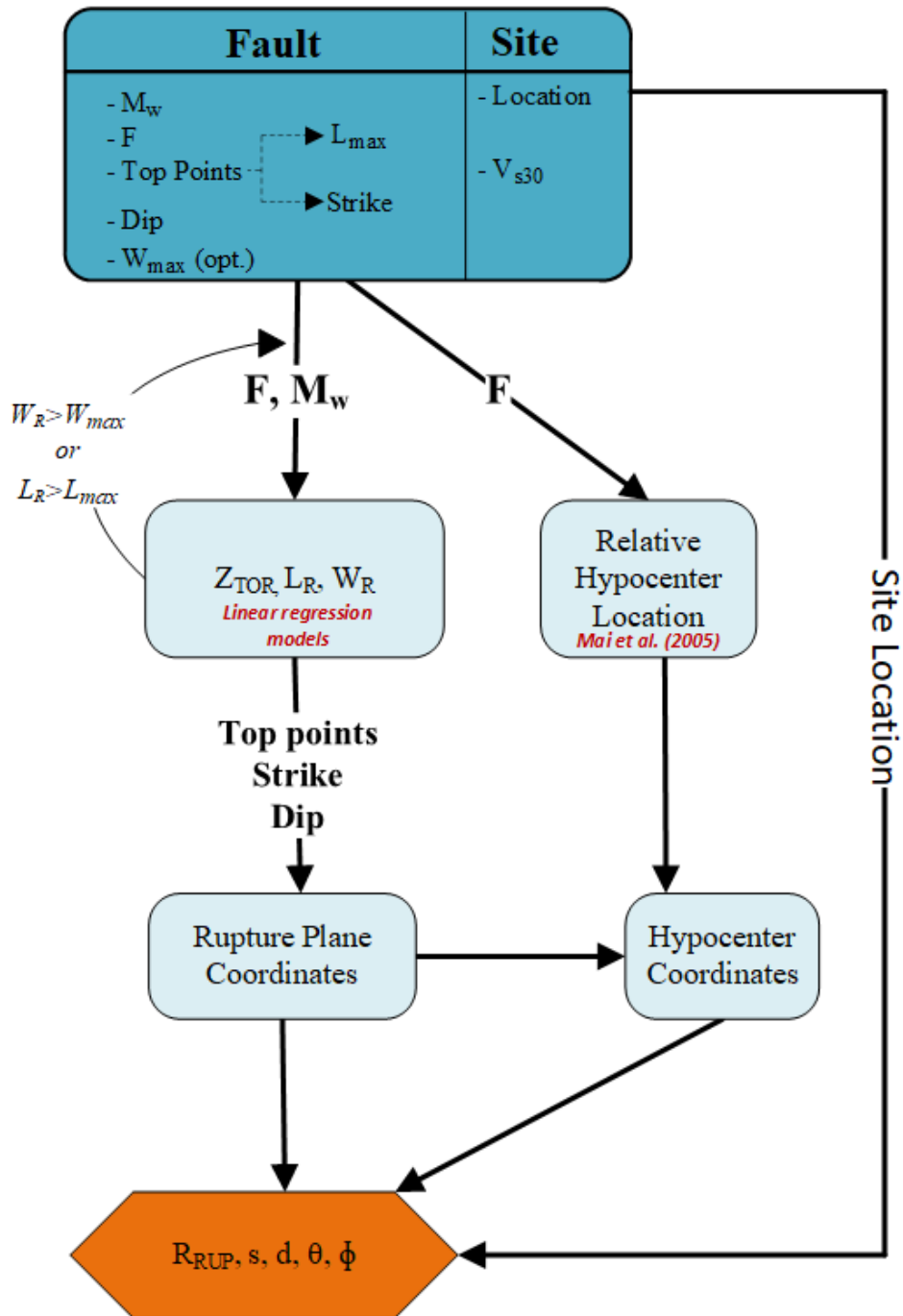


Figure A1. Simulation procedure P1.

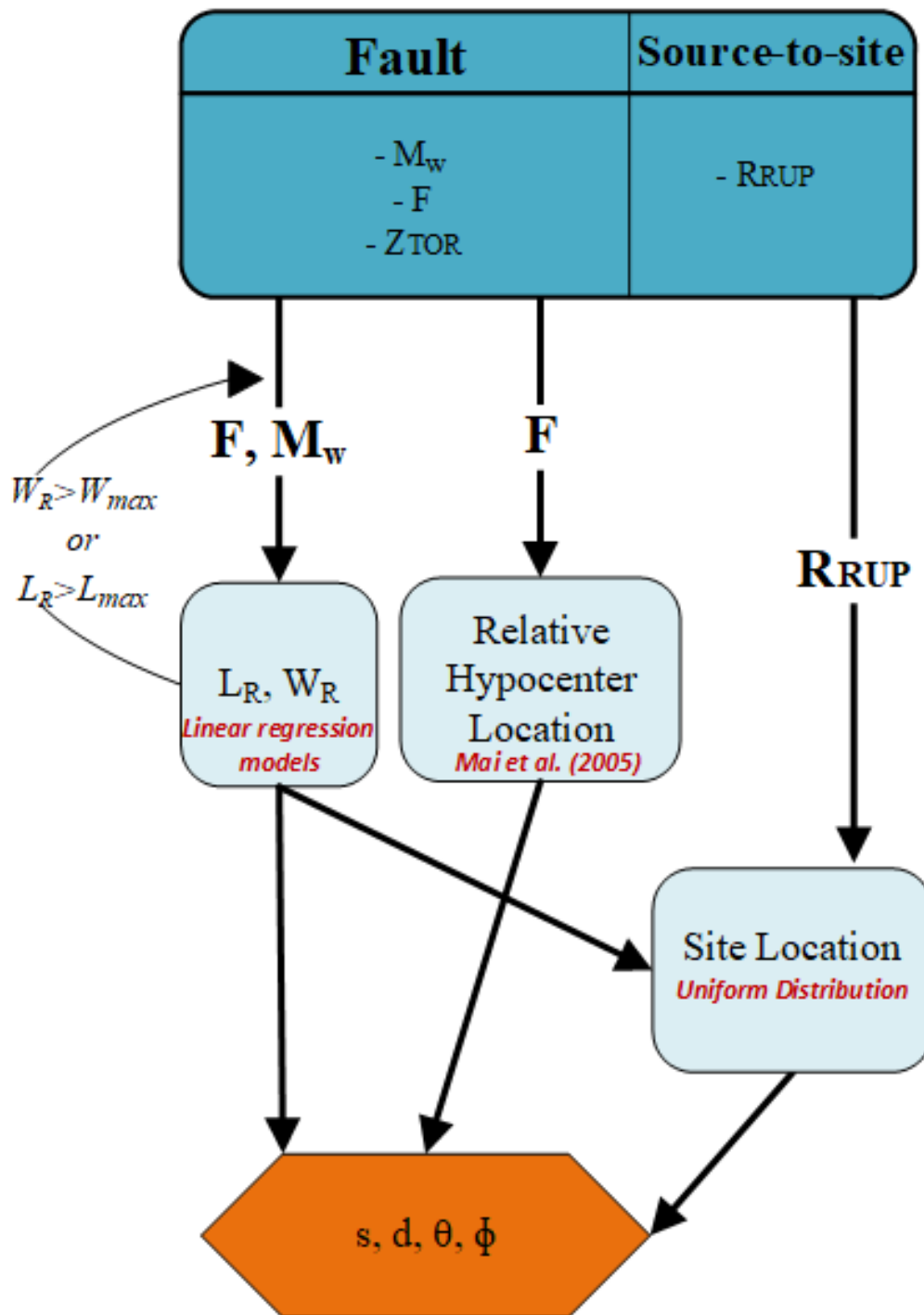


Figure A2. Simulation procedure P2.

APPENDIX B

RUPTURE GEOMETRY MODELS – DIAGNOSTIC PLOTS

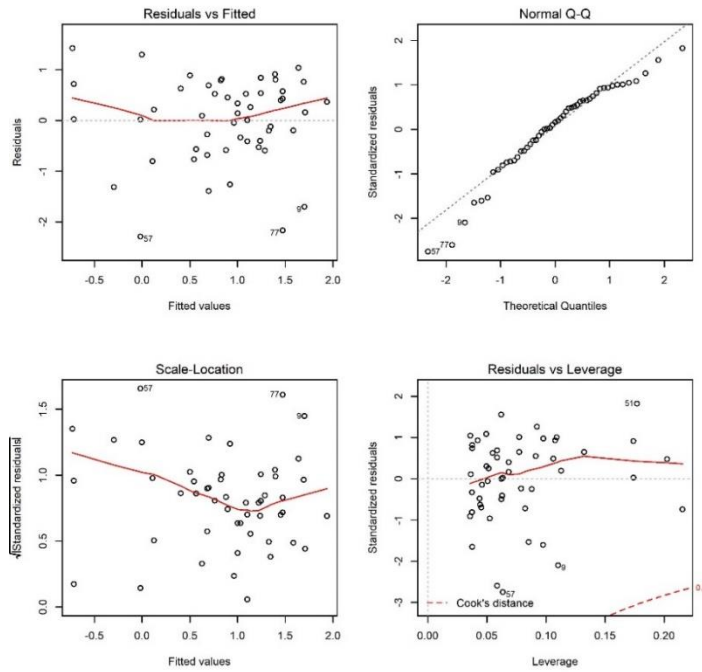


Figure B1. Diagnostic plots of the model for $Z_{TOR} > 0$.

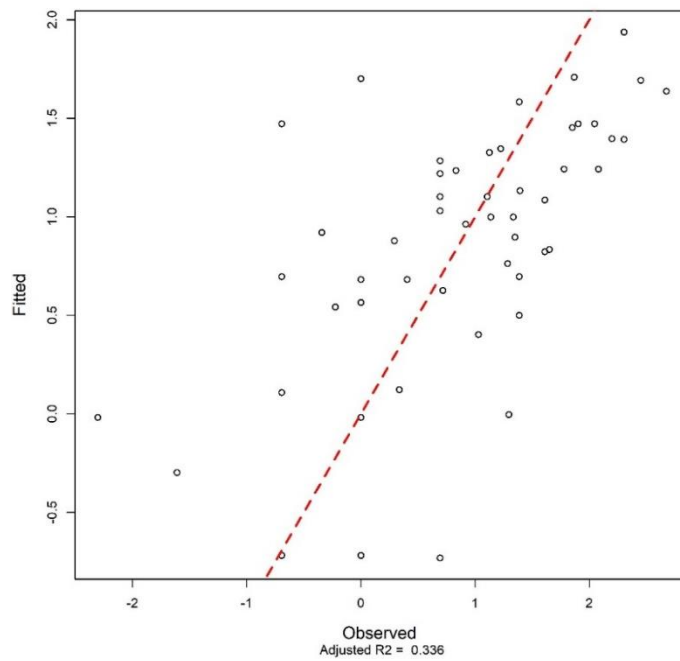


Figure B2. Plot of the fitted versus observed values of Z_{TOR} when $Z_{TOR} > 0$.

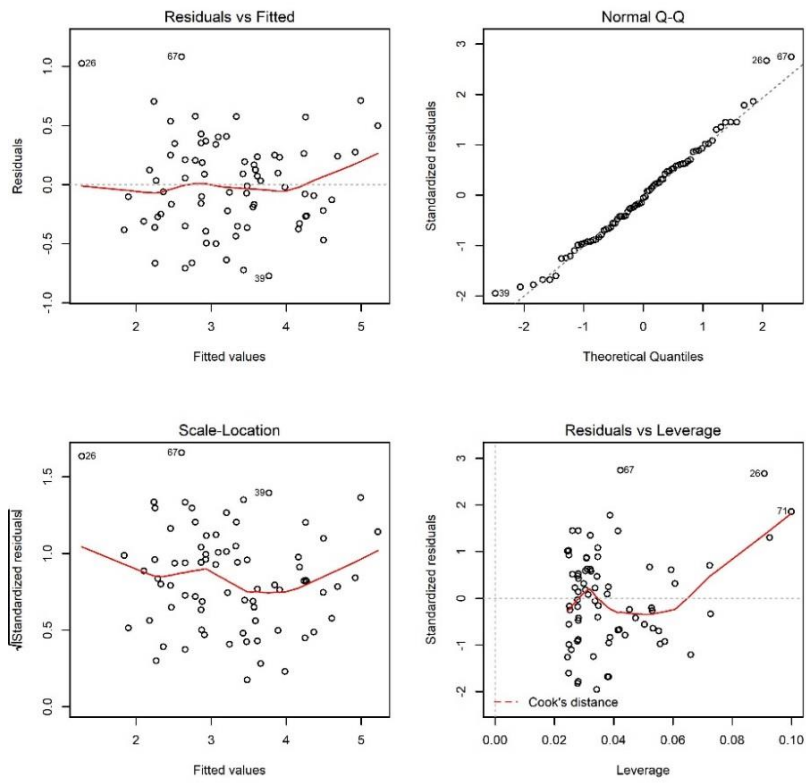


Figure B3. Diagnostic plots of the model for L_R .

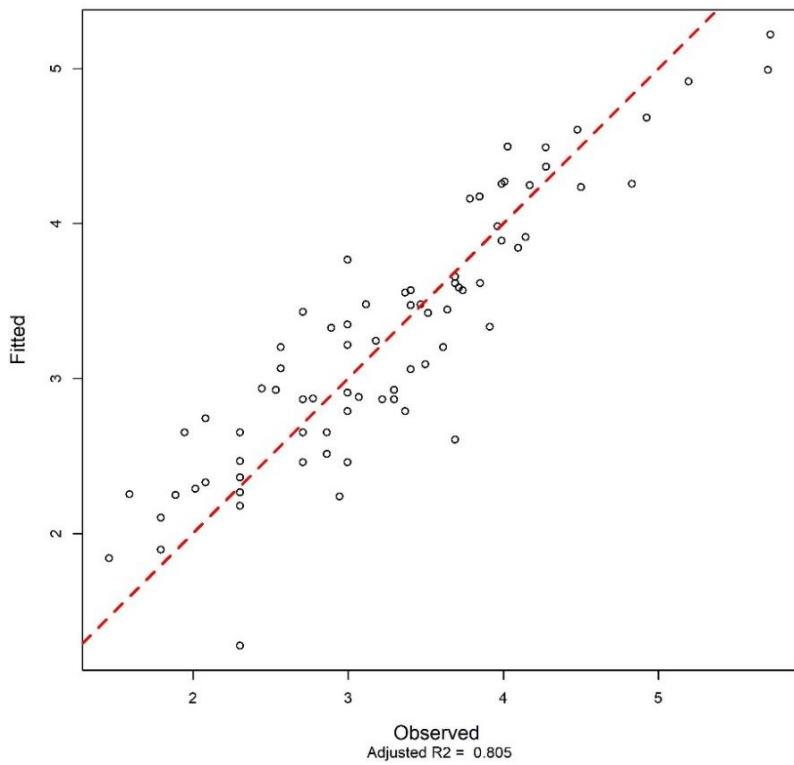


Figure B4. Plot of the fitted versus observed values of L_R .

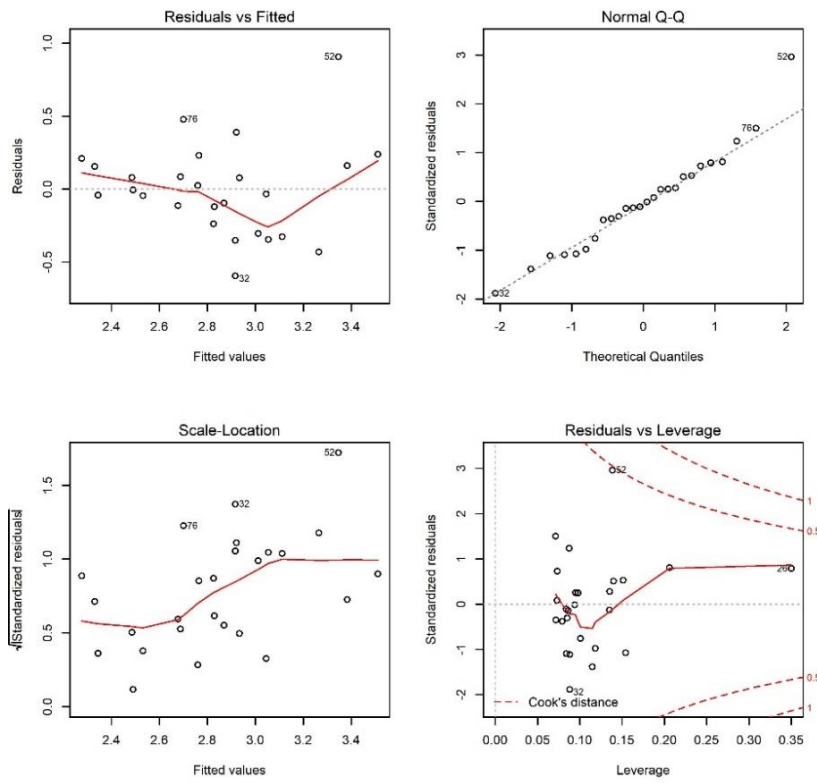


Figure B5. Diagnostic plots of the model for $W_R | Ztor = 0$.

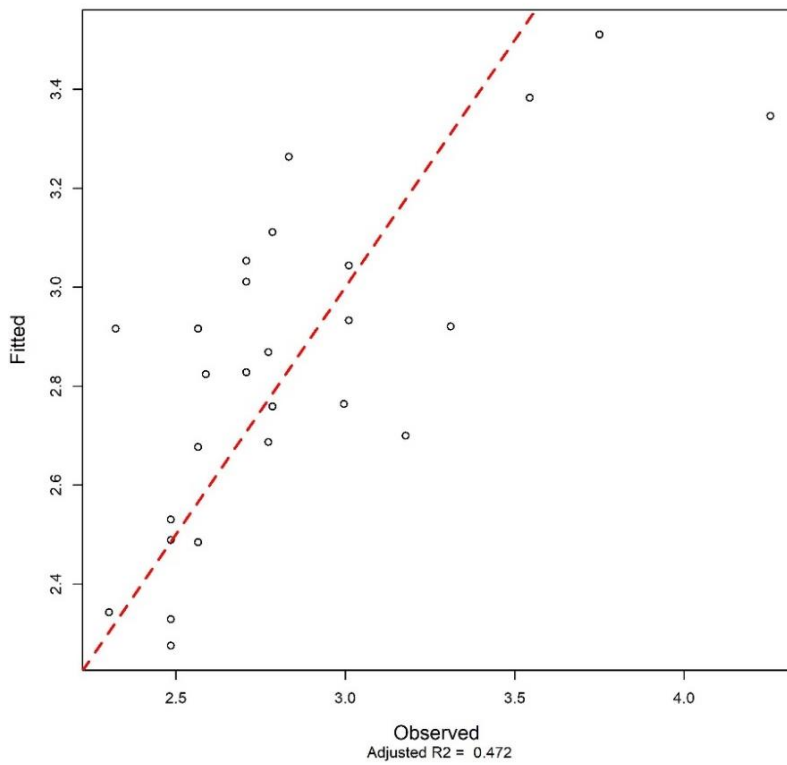


Figure B6 Plot of the fitted versus observed values of $W_R | Ztor = 0$.

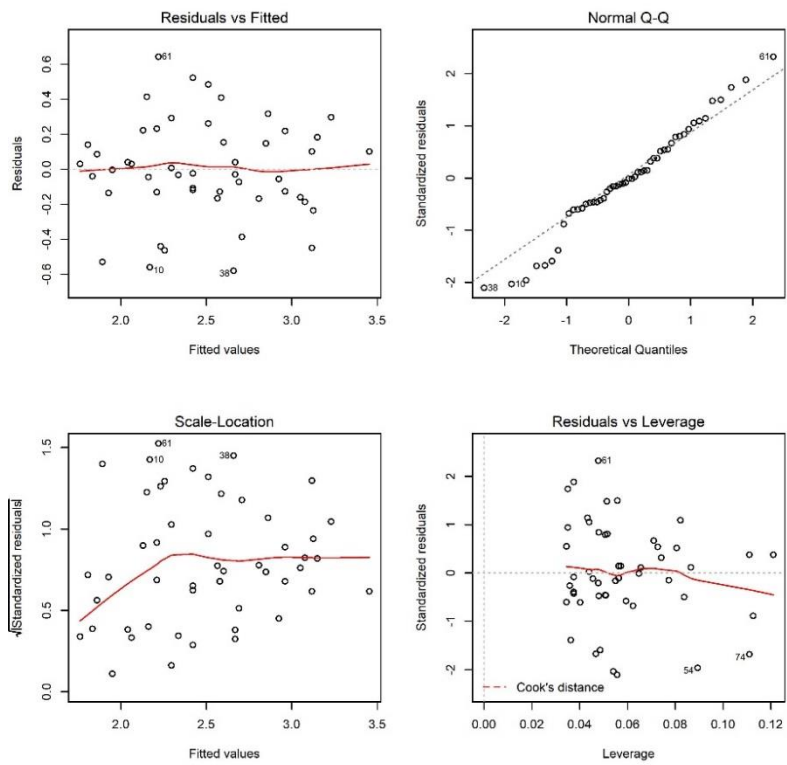


Figure B7. Diagnostic plots of the model for $W_R | Ztor > 0$.

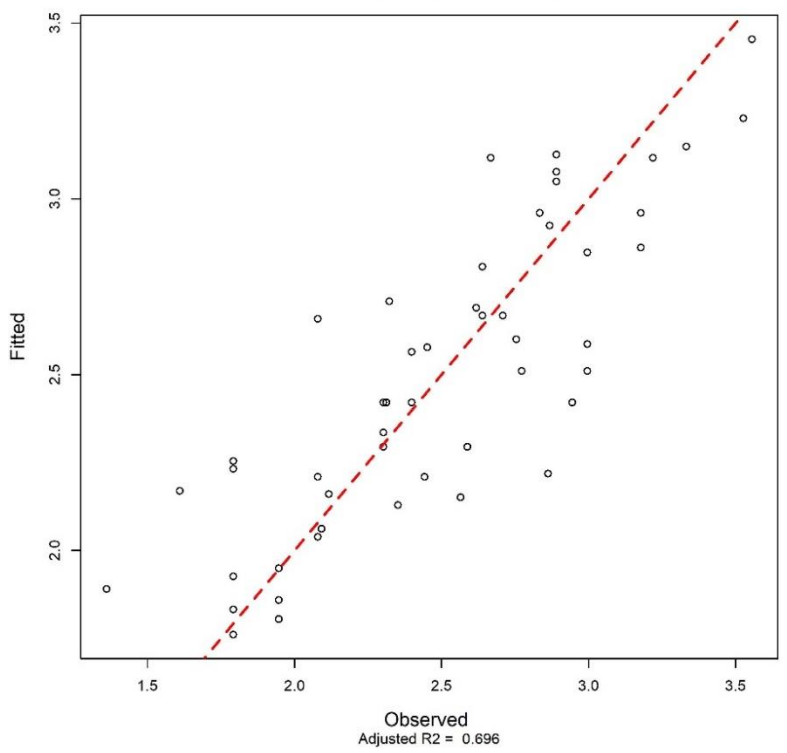


Figure B8. Plot of the fitted versus observed values of $W_R | Ztor > 0$

APPENDIX C

P2 SIMULATIONS VS GMPES

All figures in this appendix show the median and median plus and minus one logarithmic standard deviation of 5% damped pseudo-acceleration response spectra of RotD50 component for 600 synthetic motions, median spectra for pulse-like and non-pulse-like synthetic motions, median and median plus and minus one logarithmic standard deviation spectra predicted by a combination of the five NGA-West2 GMPEs, and median spectra predicted by each of the five NGA-West2 GMPEs for two different earthquake scenarios.

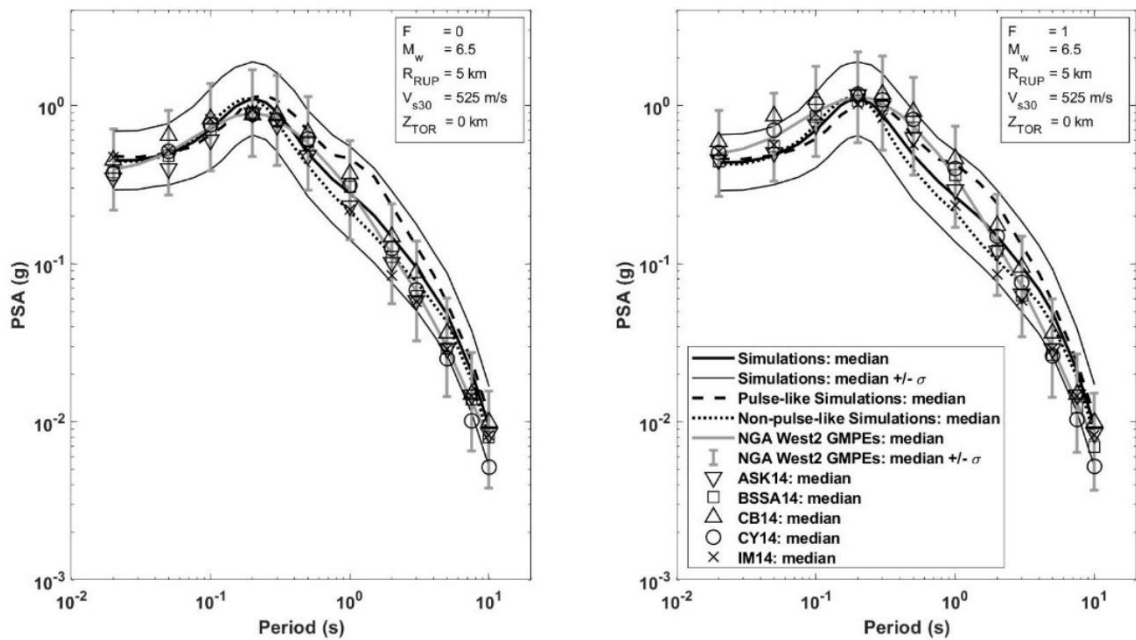


Figure C1. Scenario $M_w = 6.5, R_{RUP} = 5$ km, $V_{S30} = 525 \frac{m}{s}$ and $Z_{TOR} = 0$ km for $F = 0$ (left) and $F = 1$ (right).

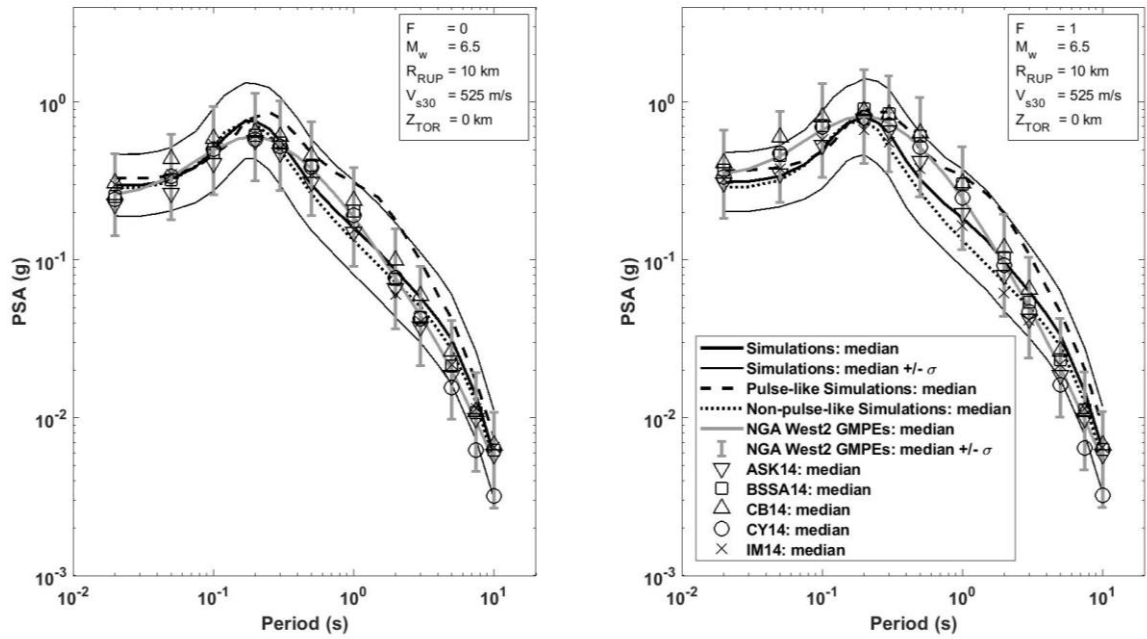


Figure C2. Scenario $M_w = 6.5, R_{RUP} = 10$ km, $V_{S30} = 525 \frac{m}{s}$ and $Z_{TOR} = 0$ km for $F = 0$ (left) and $F = 1$ (right).

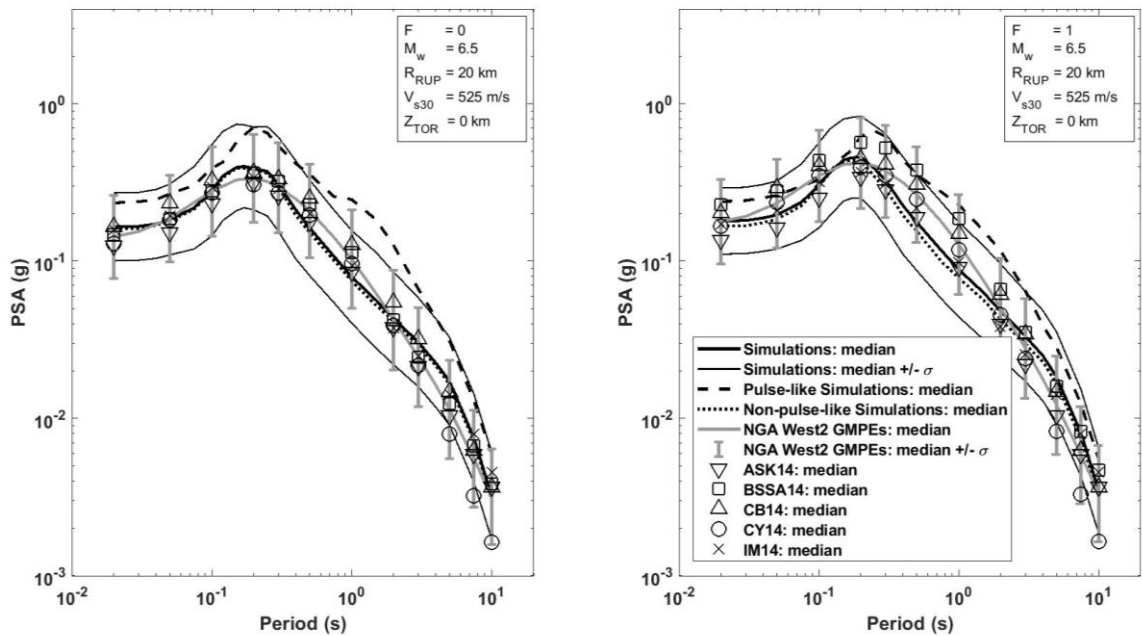


Figure C3. Scenario $M_w = 6.5, R_{RUP} = 20$ km, $V_{S30} = 525 \frac{m}{s}$ and $Z_{TOR} = 0$ km for $F = 0$ (left) and $F = 1$ (right).

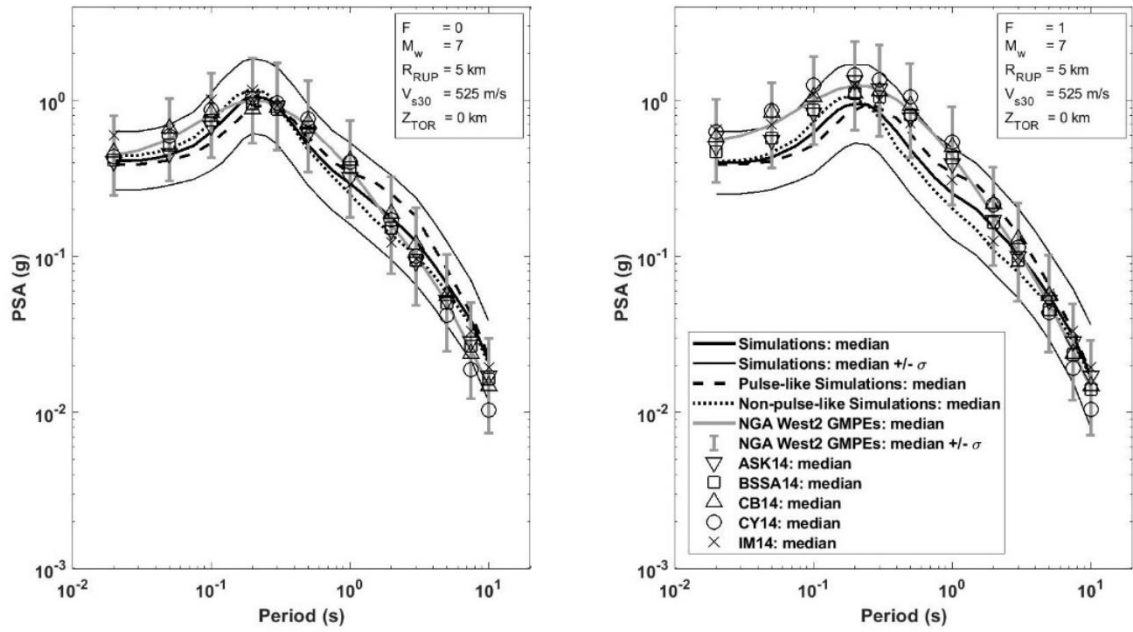


Figure C4. Scenario $M_w = 7, R_{RUP} = 5$ km, $V_{S30} = 525 \frac{m}{s}$ and $Z_{TOR} = 0$ km for $F = 0$ (left) and $F = 1$ (right).

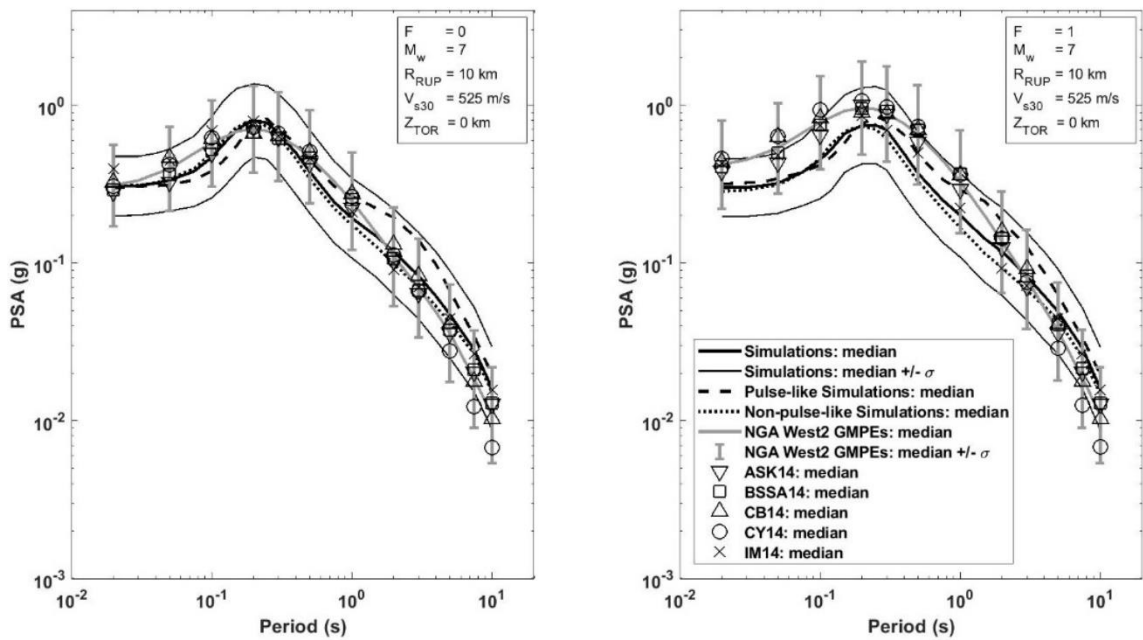


Figure C5. Scenario $M_w = 7, R_{RUP} = 10$ km, $V_{S30} = 525 \frac{m}{s}$ and $Z_{TOR} = 0$ km for $F = 0$ (left) and $F = 1$ (right).

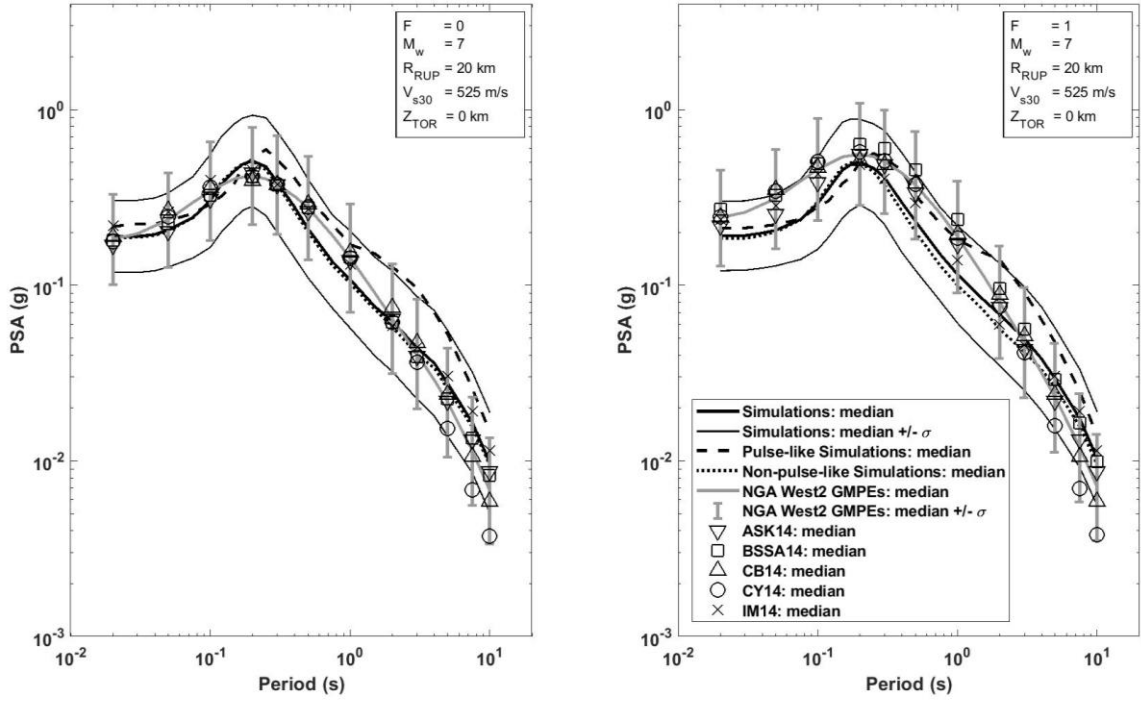


Figure C6. Scenario $M_w = 7, R_{RUP} = 20$ km, $V_{S30} = 525 \frac{m}{s}$ and $Z_{TOR} = 0$ km for $F = 0$ (left) and $F = 1$ (right).

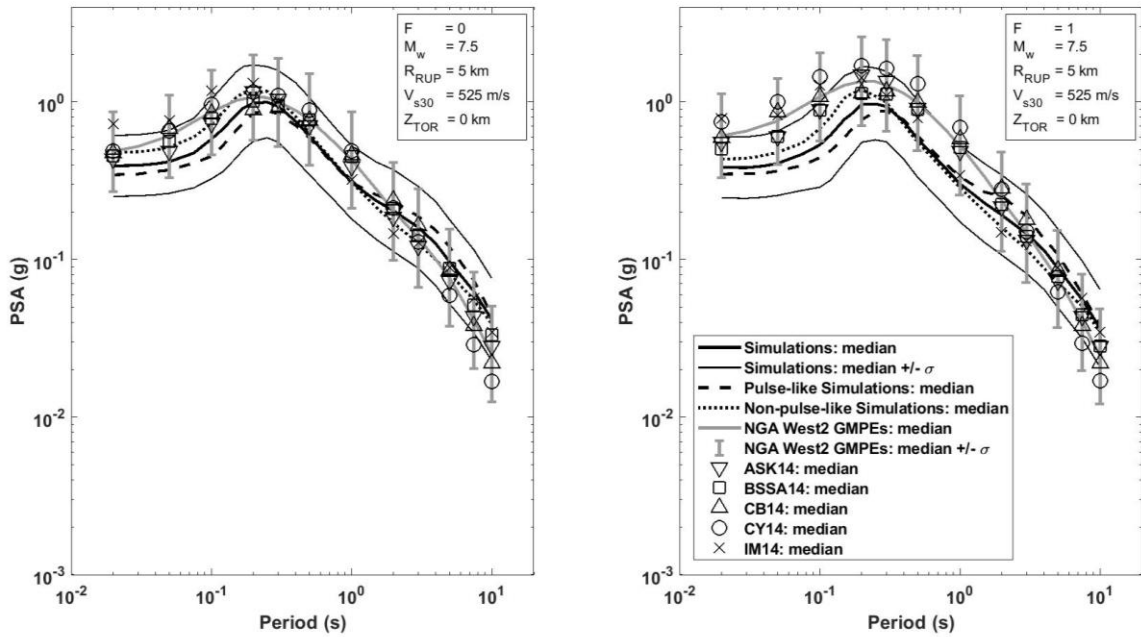


Figure C7. Scenario $M_w = 7.5, R_{RUP} = 5$ km, $V_{S30} = 525 \frac{m}{s}$ and $Z_{TOR} = 0$ km for $F = 0$ (left) and $F = 1$ (right).

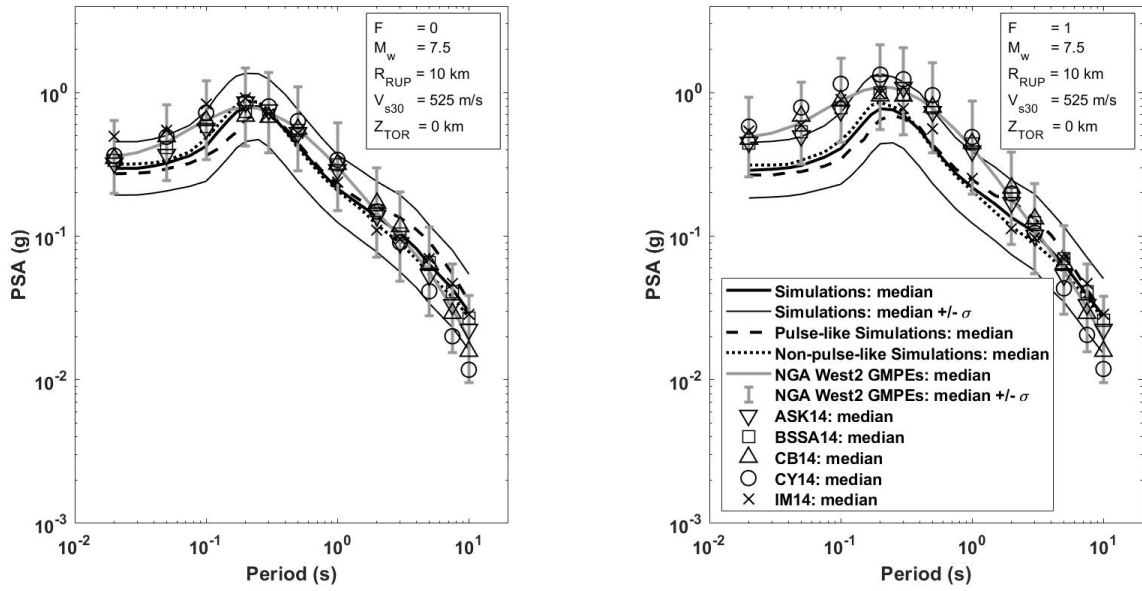


Figure C8. Scenario $M_w = 7.5, R_{RUP} = 10$ km, $V_{S30} = 525 \frac{m}{s}$ and $Z_{TOR} = 0$ km for $F = 0$ (left) and $F = 1$ (right).

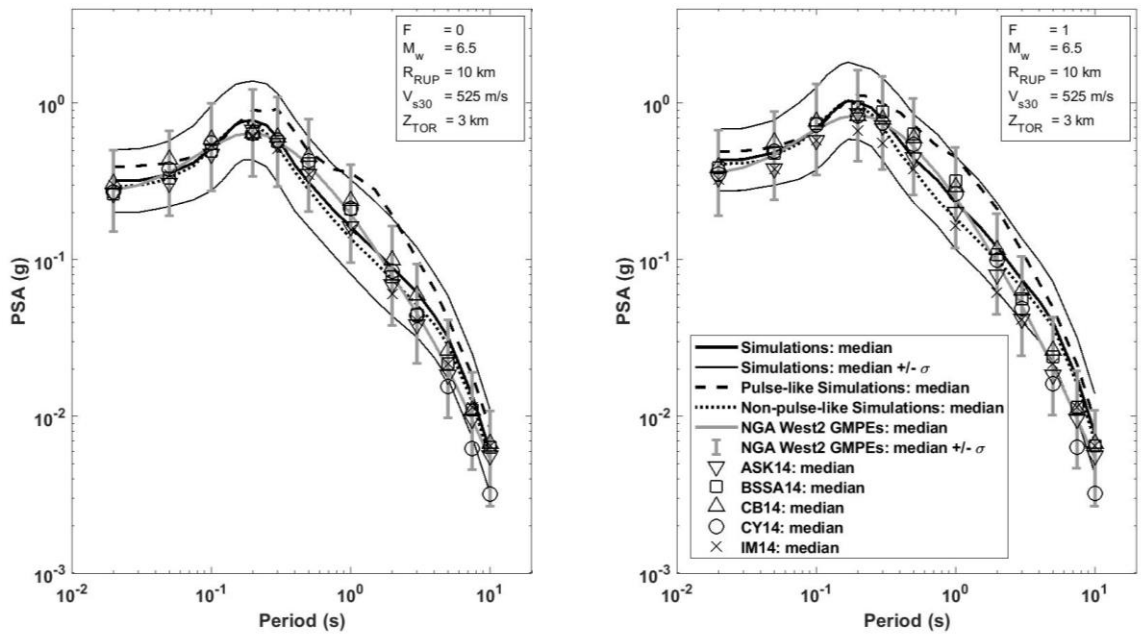


Figure C9. Scenario $M_w = 6.5, R_{RUP} = 10$ km, $V_{S30} = 525 \frac{m}{s}$ and $Z_{TOR} = 3$ km for $F = 0$ (left) and $F = 1$ (right).

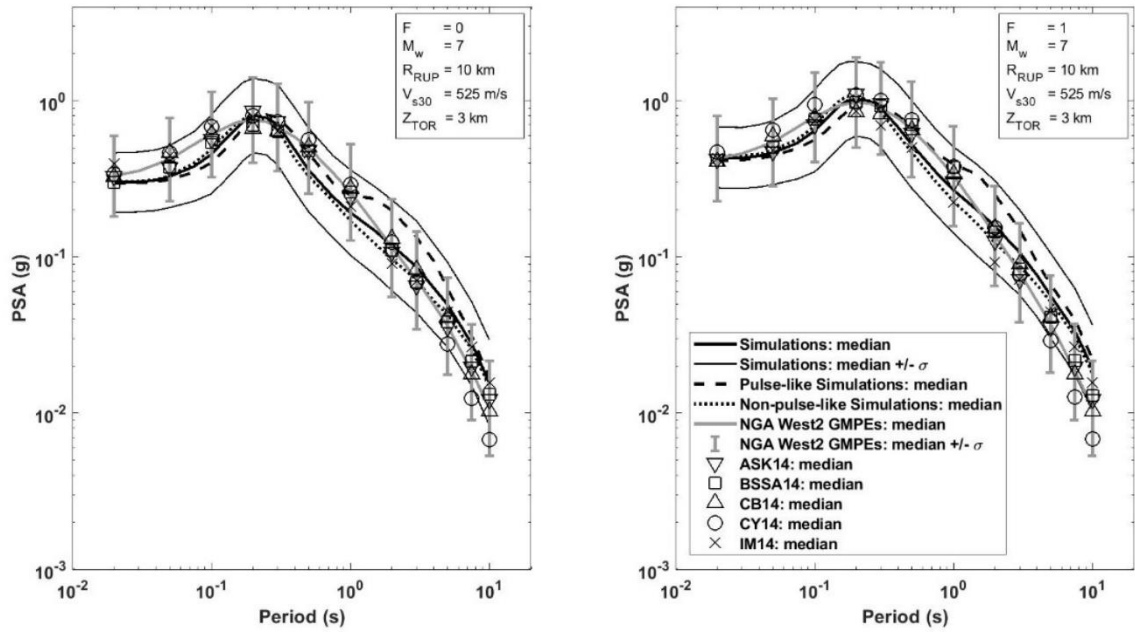


Figure C10. Scenario $M_w = 7, R_{RUP} = 10$ km, $V_{S30} = 525 \frac{m}{s}$ and $Z_{TOR} = 3$ km for $F = 0$ (left) and $F = 1$ (right).

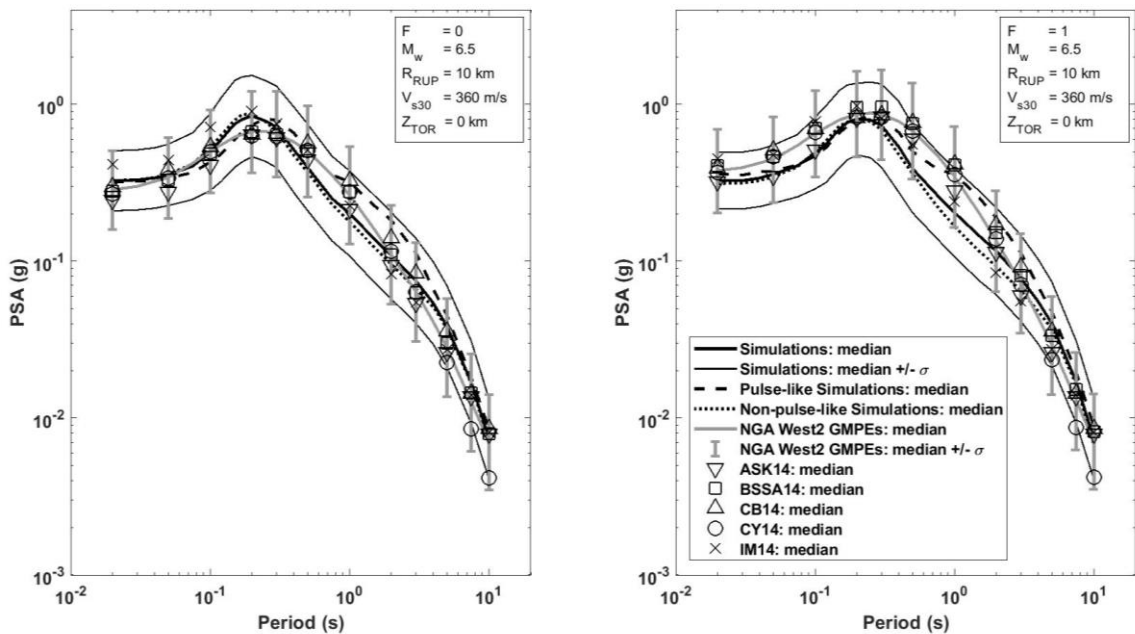


Figure C11. Scenario $M_w = 6.5, R_{RUP} = 10$ km, $V_{S30} = 360 \frac{m}{s}$ and $Z_{TOR} = 0$ km for $F = 0$ (left) and $F = 1$ (right).

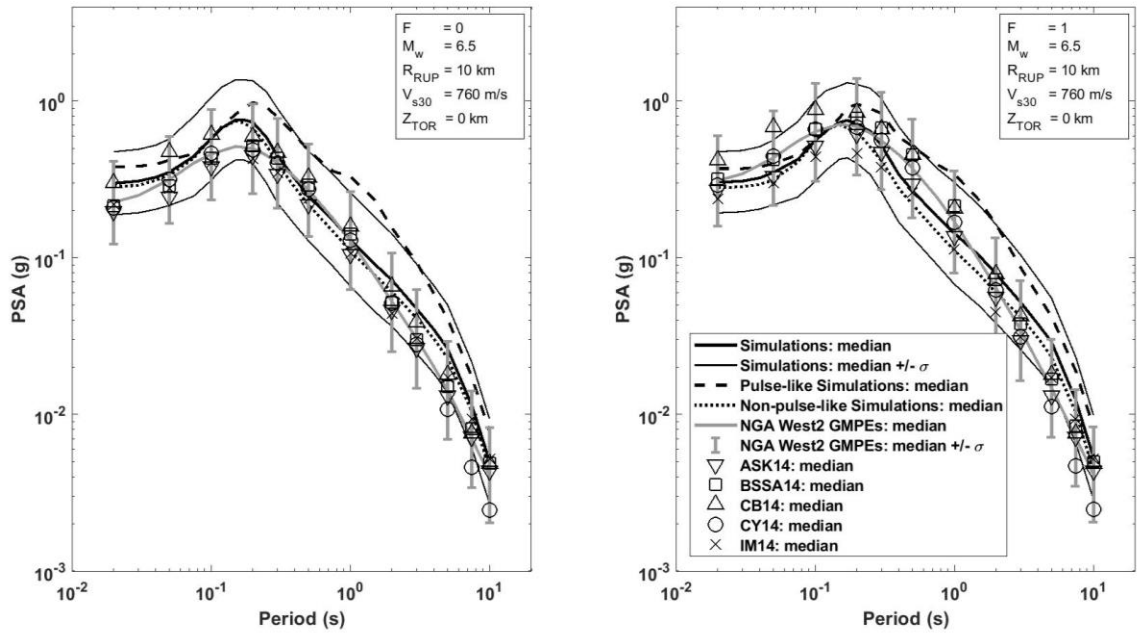


Figure C12. Scenario $M_w = 6.5, R_{RUP} = 10$ km, $V_{S30} = 760 \frac{m}{s}$ and $Z_{TOR} = 0$ km for $F = 0$ (left) and $F = 1$ (right).

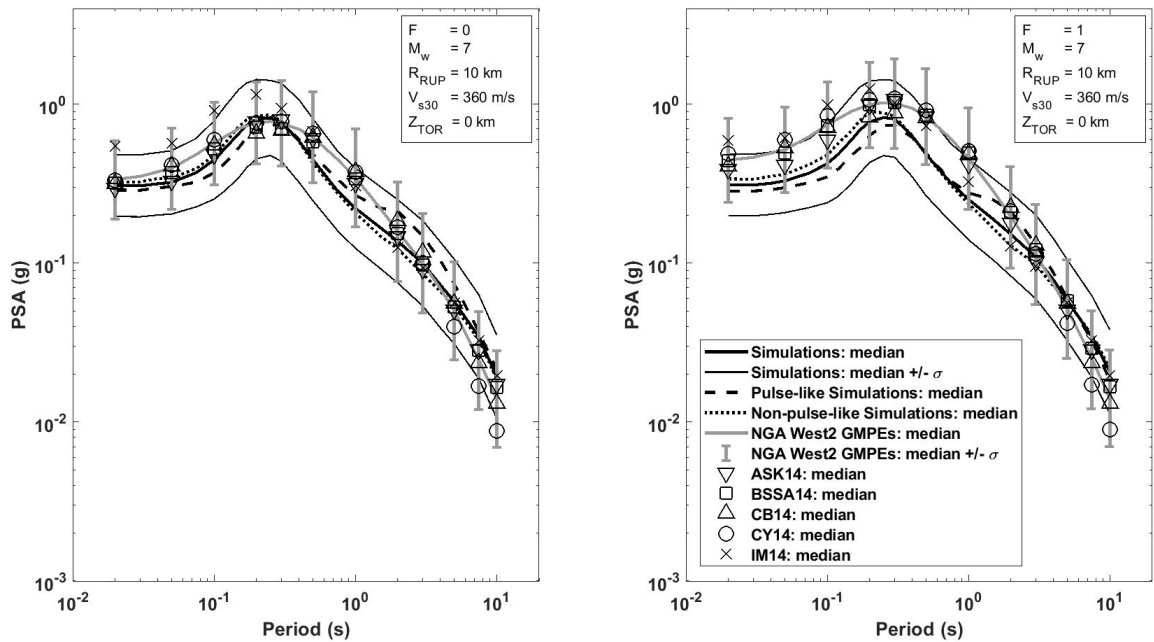


Figure C13. Scenario $M_w = 7, R_{RUP} = 10$ km, $V_{S30} = 360 \frac{m}{s}$ and $Z_{TOR} = 0$ km for $F = 0$ (left) and $F = 1$ (right).

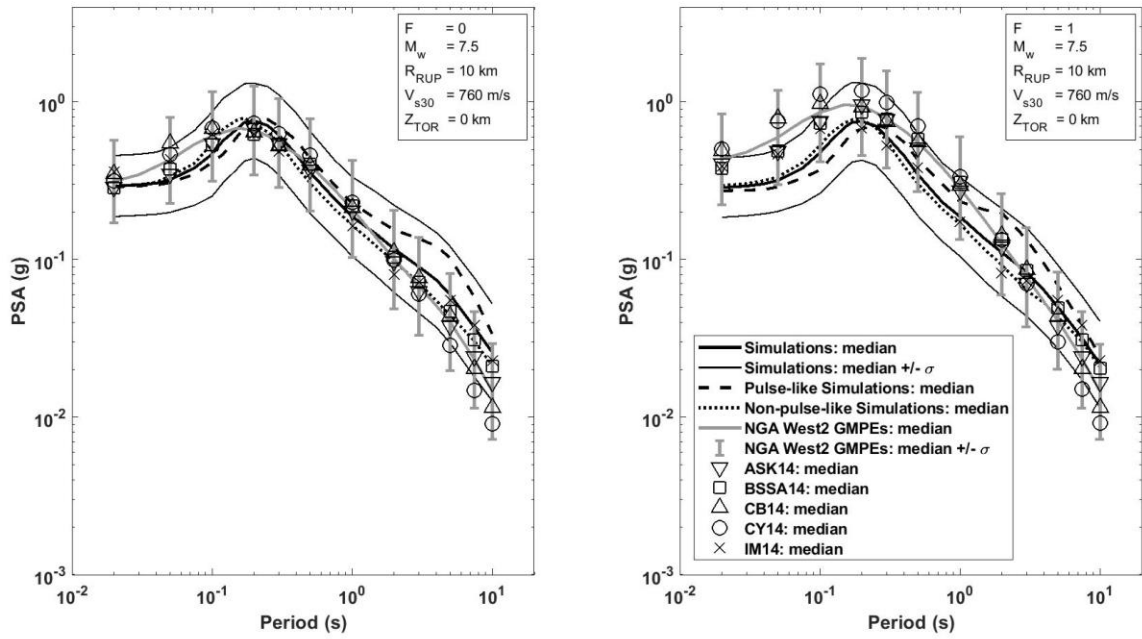


Figure C14. Scenario $M_w = 7.5$, $R_{RUP} = 10$ km, $V_{s30} = 760 \frac{m}{s}$ and $Z_{TOR} = 0$ km for $F = 0$ (left) and $F = 1$ (right).